Inverse Compton scattering in high energy astrophysics.

A thesis submitted for the degree of
Doctor of Philosophy

by

Jason Cullen

Research Centre for Theoretical Astrophysics
& Theoretical Physics Group
School of Physics
University of Sydney
Australia

August 2001

Declaration of originality

To the best of my knowledge, this thesis contains no copy or paraphrase of work published by another person, except where duly acknowledged in the text. This thesis contains no material which has been presented for a degree at the University of Sydney or any other university.

Jason Cullen

Acknowledgements

I wish to thank Zdenka Kuncic and Kinwah Wu for important suggestions regarding the work in Chapter 4.

I also wish to thank Chris Rennie for advice on the IDL routine used in Chapter 5.

Thanks also to Roberto Soria for suggesting I work on bulk rotational motion Comptonization.

My grateful thanks to my principle supervisor for this thesis, Kinwah Wu.

Abstract

This thesis investigates some aspects of the inverse Compton scattering process within various physical contexts in high energy astrophysics. Initially an introduction to the key results of Comptonization theory for the case of scattering in optically thick plasmas is given, using a diffusion approach, since these results are required for the interpretation of Comptonized spectra.

Since Comptonization in astrophysical systems is frequently treated using numerical techniques, an introduction to these is then presented. Such linear Monte Carlo photon transport codes are typically applied to scattering in plasmas without temperature and density gradients. Additionally, treating bulk motion can be difficult even for simple cases.

It is demonstrated that these problems can be made tractable numerically with the use of algorithms associated with non-linear Monte Carlo codes. Such codes can already treat scattering within arbitrary velocity structures in a plasma, and an extension of the algorithm is proposed that enables the easy calculation of photon transport in plasmas with non-constant density as well as non-constant temperature and/or bulk motion. This algorithm and code has been developed to treat scattering in astrophysical situations where bulk motion, temperature gradients and density gradients are simultaneously present in a plasma.

Both a semi-analytic approach and the numerical approach are then used to treat Comptonization problems of current interest. Firstly, the standard two-phase disk–corona model for the high-energy spectra of Active Galactic Nuclei is modified to include an an outflow or wind which may provide an additional source of disk cooling. Earlier slab disk–corona models predict a spectral index which is consistent with observations only if all the accretion power is dissipated in the corona. For the models investigated here, energy spectral indices that are consistent with observations can be obtained with less accretion power being dissipated in the corona, as a result of an outflow/wind. However, it is required that the wind extract large amounts of power from the disk, and it it yet to be seen if this is a plausible scenario.

Secondly, the linear numerical technique is then applied to a study of the time delay or lag of high energy photons due to the inverse Compton process, for cases where the scattering plasma is characterised by more than one temperature. Such a model has been proposed for Cyg X-1, and the spectral and temporal behaviour of such a model is investigated. Predictions are made regarding the form that the time lag curve should take if this particular geometry is a realistic model for the material surrounding Galactic black hole candidates.

The extended non-linear algorithm is then applied to the study of scattering in bulk motion accretion flows in both one and two dimensions. The 1-D case is that of line photon scattering in the accretion column of a magnetised white dwarf star, and the resulting spectra are presented for various inclination angles, accretion rates, and Cyclotron cooling rates in the post-shock region. Spectra as a function of inclination angle are also obtained and beaming of photons by the inhomogeneous column is investigated.

The 2-D case is that of Comptonization in a rotating torus geometry, which is a first attempt at considering scattering in an orbiting accretion disk-like structure. Different photon injection spectra are investigated for different values of the electron momentum within the torus. It is found that for a reasonable optical depth and electron momentum, lines can be significantly broadened by rotational Compton scattering.

Contents

List of Figures

Part I

Background

Chapter 1

Theory of Compton scattering

This thesis investigates the Comptonization process within various physical contexts in high energy astrophysics. This Chapter gives an introduction to some of the main results of Comptonization theory, and to astrophysical systems in which Comptonization is important.

1.1 Introduction

Astrophysical sources of X-ray photons are frequently interpreted in terms of low energy photons entering a region of hot plasma and scattering off energetic electrons. The photons gain energy (on average) from the electrons via the inverse Compton scattering process. Energy exchange due to multiple inverse Compton scattering events is termed Comptonization. Photons may scatter multiple times, and before escaping from the plasma a typical photon may have been scattered up to X-ray or even gamma-ray energies. Thus one is interested in the transport of photons through an electron plasma as they gain energy at a succession of scattering events. Spectra given by this process are said to have been Comptonized.

1.2 Compton scattering

1.2.1 Energy shift

In the limit of a photon's energy ϵ being significantly smaller than the electron rest mass energy 511 keV, the interaction between a photon and an electron can be adequately

described by the Thompson cross-section σ_T. For photons with energy $\epsilon \geq 511$ keV, however, the relativistic cross-section derived from quantum electrodynamics must be used. This cross-section is known as the Klein-Nishina cross-section,

$$\sigma_{KN} = \frac{2\pi e^4}{x m_e^2 c^4}\left[(1-\frac{4}{x}-\frac{8}{x})\ln(1+x)+\frac{1}{2}+\frac{8}{x}-\frac{1}{2(1+x)^2}\right] , \tag{1.1}$$

where $x \equiv 2\left(\frac{h\nu}{m_e c^2}\right)\gamma(1-\mathbf{\Omega}.\mathbf{v}/c)$, and ν is the photon frequency, $\mathbf{\Omega}$ is the photon propagation vector, γ is the Lorentz factor of the electron, $\mathbf{v}$ is the electron velocity vector, h is Plank's constant, m_e is the electron rest mass and c is the speed of light. The Klein-Nishina cross-section becomes smaller than σ_T at energies well above 511 keV, when $\sigma_{KN} \sim (2\pi e^4/xm^2c^4)\left[\ln(x)+\frac{1}{2}\right]$, and reduces to the Thompson case at low energies, $\sigma_{KN} \sim \sigma_T(1-x)$.

At an interaction (or scattering event), energy can be exchanged between the photon and the electron, and if the energy of the electron is greater than that of the photon, the photon is likely to gain energy from the electron and increase its frequency. Consider a single photon of energy ϵ about to scatter off an electron of energy $\gamma m_e c^2$. In the electron frame the photon energy before the scattering is

$$\epsilon_1 = \epsilon\gamma(1-\beta\cos\theta) . \tag{1.2}$$

where θ is the angle between the electron direction of motion and the photon direction of propagation, γ is the electron Lorentz factor and $\beta = v/c$.

After the scattering event, the photon energy changes from ϵ_1 to $\epsilon_1^{'}$, where dashed quantities are those after the scattering event. The transformation out of the electron frame and into the laboratory frame then gives

$$\epsilon^{'} = \epsilon_1^{'}\gamma^{'}(1+\beta^{'}\cos\theta^{'}) , \tag{1.3}$$

If $\epsilon_1^{'} \simeq \epsilon_1$ (elastic scattering) and the energy of the electron has not changed significantly, one has

$$\epsilon^{'} = \epsilon\gamma^2(1-\beta\cos\theta)(1+\beta\cos\theta^{'}) . \tag{1.4}$$

A typical photon might then increase its energy by a factor of γ^2 at a scattering event. A photon can have an energy of up to 100 keV in the rest frame of the electron and still be well described by the Thompson cross-section. Therefore energies of $\gamma 100$ keV can be produced in a single scattering event. Because the energy of the photon has increased, it is said that the photon has been scattered up to higher energies, or 'up-scattered'.

Conservation of energy at the scattering event can be used to put an upper limit on the amount of energy transferred. The total incoming energy is the energy of the

electron $\gamma m_e c^2$ and the energy of the photon ϵ. Therefore, the energy of the outgoing photon must be

$$\epsilon^{'} \leq \epsilon + \gamma m_e c^2 \ , \tag{1.5}$$

and so the shift in energy is,

$$\Delta\epsilon \equiv \epsilon^{'} - \epsilon \leq \gamma m_e c^2 \ . \tag{1.6}$$

At each scattering event, the photon cannot gain more energy from the electron than the electron has to start with.

1.2.2 Low and high optical depth regimes

The form of the spectrum that results from multiple inverse Compton scattering events is of interest in high energy astrophysics. It is possible to define an optical thickness $\tau = \int n_e \sigma_T \, dl$, where n_e is the electron density along a ray of length l, which is a measure of the number of scattering events a photon undergoes in escaping from a source region. In the limit of small τ (the optically thin regime), there exists an estimate for the spectrum, attributed to Zeldovich but never published by him (see Rybicki & Lightman 1979).

The photon frequency after a single scattering event can be written as

$$\nu^{'} = \nu A \ , \tag{1.7}$$

where ν is the photon frequency before scattering, and A is an amplification factor to be determined. If a photon initially has a frequency of ν_0, then after scattering k times the frequency of the photon will be

$$\nu_k = \nu_0 A^k \ \ \text{which implies} \ \ \mathrm{k} = \frac{\log(\nu/\nu_\mathrm{o})}{\log(\mathrm{A})} \ , \tag{1.8}$$

where A has been averaged over many scattering events.

The probability of escape from the plasma cloud after undergoing a single scattering event is $P_1 = 1 - \exp(-\tau) \approx \tau$, so the probability of escape after k (independent) scattering events is $P_k \approx \tau^k$. The spectrum is therefore the initial intensity times the probability of escape,

$$\begin{aligned} I_\nu &\sim I_0 \tau^{\,k} \\ &= I_0 \tau^{\,\log(\nu/\nu_o)/\log(A)} \end{aligned}$$

$$= I_0 \left(\frac{\nu}{\nu_0}\right)^{\log(\tau)/\log(A)}$$

$$= I_0 \left(\frac{\nu}{\nu_0}\right)^{-\alpha}, \tag{1.9}$$

where $\alpha \equiv -\log(\tau)/\log(A)$. The spectrum from an optically thin electron cloud is therefore a power law with energy spectral index α. Note that it has been implicitly assumed that the amplification factor is not a function of photon frequency.

In the limit of infinite τ (the infinitely optically thick case), and for non-relativistic temperatures, the evolution of the photon spectrum is determined by the Kompaneets equation,

$$\frac{\partial\, n(x,t)}{\partial t} = n_e \sigma_T\, c\, \Theta \frac{1}{x^2}\frac{\partial}{\partial x}\left[x^4\left(\frac{\partial\, n(x,t)}{\partial x} + n(x,t) + n(x,t)^2\right)\right], \tag{1.10}$$

where $n(x,t)$ is the photon occupation number, $x \equiv h\nu/kT_e$ is the dimensionless photon frequency, and c the speed of light. $\Theta \equiv kT_e/m_e c^2$ is the dimensionless electron temperature, with T_e the electron temperature. The electron density n_e is assumed constant.

The Kompaneets equation is a Fokker-Planck equation for the photon occupation number, that is found by expanding the Boltzmann equation in terms of a small energy shift at each scattering event. The first term in the curved brackets represents a secular gain of energy by the photons due to the Doppler effect, the second term is due to the electron recoil effect and acts to limit the photon energy gain as the energy of the photons approaches that of the electrons. The $n(x,t)^2$ term describes induced scattering, a quantum effect that is usually negligible in most astrophysical applications.

The Kompaneets equation assumes that all the photons are of low enough energy to be described by the Thompson cross-section, and the electrons are non-relativistic so that the average change in photon energy at a scattering event is small.

Dropping the $n(x,t)$ and $n(x,t)^2$ terms and changing variables gives

$$\frac{\partial\, n(x,y)}{\partial y} = \frac{1}{x^2}\frac{\partial}{\partial x}\left[x^4\left(\frac{\partial\, n(x,y)}{\partial x}\right)\right]. \tag{1.11}$$

where the Kompaneets y parameter is defined by $y \equiv n_e \sigma_T\, c\, \Theta\, t$. (For a stationary case the y parameter is defined as the product $\Theta\tau$, and is a measure of the total amount of energy transferred from the electrons to the photons.)

Making a change of variables to $x = \exp(r)$ in Eq. 1.11 (so that $\frac{\partial}{\partial x} = \exp(-r)\frac{\partial}{\partial r}$) gives

$$\frac{\partial\, n}{\partial y} = 3\frac{\partial\, n}{\partial r} + \frac{\partial^2\, n}{\partial r^2}. \tag{1.12}$$

This equation is related to the one-dimensional diffusion equation by a further change of variables. To see this, begin with the diffusion equation

$$\frac{\partial\, n(z,s)}{\partial s} = \frac{\partial^2\, n(z,s)}{\partial z^2}\ , \tag{1.13}$$

and change the variables from z and s to r and y, where

$$r = z - 3s \tag{1.14}$$

$$y = s\ . \tag{1.15}$$

By the chain rule, one has

$$\begin{aligned}\frac{\partial\, n}{\partial s} &= \frac{\partial\, n}{\partial r}\frac{\partial\, r}{\partial s} + \frac{\partial\, n}{\partial y}\frac{\partial\, y}{\partial s} \\ &= -3\frac{\partial\, n}{\partial r} + \frac{\partial\, n}{\partial y}\ ,\end{aligned} \tag{1.16}$$

since $\partial\, r/\partial s = -3$ and $\partial\, y/\partial s = 1$. Also by the chain rule,

$$\begin{aligned}\frac{\partial\, n}{\partial z} &= \frac{\partial\, n}{\partial r}\frac{\partial\, r}{\partial z} + \frac{\partial\, n}{\partial y}\frac{\partial\, y}{\partial z} \\ &= \frac{\partial\, n}{\partial r}\ ,\end{aligned} \tag{1.17}$$

as $\partial\, r/\partial z = 1$ and $\partial\, y/\partial z = 0$. Eq. 1.17 then implies

$$\frac{\partial^2\, n}{\partial z^2} = \frac{\partial^2\, n}{\partial r^2}\ . \tag{1.18}$$

Substituting Eq. 1.16 and Eq. 1.18 into the diffusion equation 1.13 gives

$$\frac{\partial\, n}{\partial y} = 3\frac{\partial\, n}{\partial r} + \frac{\partial^2\, n}{\partial r^2}\ , \tag{1.19}$$

which is the same as Eq. 1.12.

The solution of the one-dimensional diffusion equation for an *infinite* medium is given by

$$n(z,s) = \frac{1}{\sqrt{4\pi\, s}}\int_{-\infty}^{\infty} n_0(z')\exp\left\{-\frac{(z-z')^2}{4s}\right\}\, dz'\ , \tag{1.20}$$

where $n_0(z')$ is the initial distribution when $s = 0$. With the change of variables $z = 3y + r$ and $r = \ln(x)$ the solution becomes

$$n(x,y) = \frac{1}{\sqrt{4\pi y}}\int_{-\infty}^{\infty} n_0(z')\exp\left\{-\frac{(\ln(x)+3y-z')^2}{4y}\right\}\, dz'\ , \tag{1.21}$$

where $z' = \ln(x')$. This solution to Kompaneets' equation was first obtained by Zeldovich & Sunyaev (1969).

For a monochromatic injection of photons this has a Gaussian profile that spreads out (broadens) in frequency with time, with the peak of the distribution moving to higher energies.

1.2.3 Moderate optical depth regime

Sunyaev & Titarchuk (1980) have developed a means of using the solution (Eq. 1.21) to calculate the spectrum from a medium of finite extent and therefore finite optical thickness (see also Illarionov, Kallman, McCray & Ross 1979).

Consider the injection of a certain number of photons into an electron plasma, where the energy of the photons is small compared to that of the electrons, and the electrons are non-relativistic so that the Thompson cross-section applies. Assume also that the plasma has a semi-infinite slab geometry. The solution to the infinite problem Eq. 1.21 gives the energy of the photons after some time t. The method used by Sunyaev & Titarchuk (1980) is the following; if one knew how many of the photons had escaped from the slab between time t and $t + dt$, that is, the distribution of photons over the escape time from the slab, one could convolve this with Eq. 1.21 and determine the spectrum of escaping photons.

To find the distribution of photons over the escape time, Sunyaev and Titarchuk solved a spatial diffusion equation. Therefore, this technique relies on a double diffusion approximation: diffusion in space and diffusion in frequency (Eq. 1.13).

To investigate the spatial transport of photons in the slab, consider the one dimensional diffusion equation

$$\frac{\partial I(\tau,u)}{\partial u} = \frac{1}{3}\frac{\partial^2 I(\tau,u)}{\partial \tau^2}\ , \tag{1.22}$$

where $u \equiv y/\Theta$ is a dimensionless time parameter and $\tau \equiv n_e \sigma_T\, r$ where the variable r measures the distance from the slab mid-plane. I is the angle-averaged intensity, where the photon occupation number is related to the intensity I by $I \equiv b n x^3$. Let us also assume that one face of the slab is along the plane $\tau = 0$ and the other face is at $\tau = 2\tau_0$ where $\tau_0 \equiv n_e \sigma_T h$, with h the half-thickness of the slab.

The equation (Eq. 1.22) is separable, so if one looks for solutions of the form $X(\tau)R(u)$ one obtains

$$I(\tau,u) = \sum_{n=1}^{\infty} c_n X_n(\tau) \exp\left\{-\frac{(\lambda_n)^2}{3}u\right\}\ . \tag{1.23}$$

In general, the boundary condition of the problem is used to determine the separation constant λ_n, while the initial distribution $n(x,0)$ is used to determine the coefficients c_n. For an arbitrary injection of photons, there may be infinitely many terms in the series solution Eq. 1.23. However, because λ_n increases with n, after some time the higher terms or modes will have died away compared to the first term or 'fundamental' mode. Therefore, the spatial distribution of photons approaches the distribution given by the first eigenfunction $X_1(\tau)$ of the spatial equation. That is, at 'late times' one has

$$I(\tau,u) \rightarrow c_1 X_1(\tau)\exp(-\beta u)\ , \tag{1.24}$$

where $\beta \equiv (\lambda_1)^2/3$.

The distribution of photons over the escape time is simply the intensity at the boundary of the slab as a function of time u, and this can be given by Eq. 1.24. A normalisation condition is also required for the fraction of photons that have escaped. Using Eq. 1.24,

$$\begin{aligned} P(u) &\equiv \frac{I(0,u)}{\int_0^\infty I(0,u)\,du} \\ &= \frac{c_1 X_1(0)\exp(-\beta u)}{c_1 X_1(0)/\beta} \\ &= \beta\exp(-\beta u)\ . \end{aligned} \tag{1.25}$$

This function $P(u)$ is the required distribution of photons over the escape time. As discussed above, if the function $P(u)$ is known it can be convolved with the solution to Kompaneets' equation to give the spectrum from a plasma cloud of finite extent,

$$N(x) = \int_0^\infty n(x,u)P(u)\,du\ . \tag{1.26}$$

Therefore the parameter β must be determined. This is done by appealing to the boundary condition of the problem.

Consider the spatial part of the problem. One has the equation

$$X_n^{''}(\tau) + \lambda_n^2 X_n(\tau) = 0\ , \tag{1.27}$$

which has the orthogonal solutions

$$X_n = \cos[\lambda_n(\tau_o - \tau)] + \sin[\lambda_n(\tau_o - \tau)]\ . \tag{1.28}$$

If one appeals to symmetry about the mid-plane of the disk and discards the $\sin$ solution,

$$X_n = \cos[\lambda_n(\tau_o - \tau)] \; . \tag{1.29}$$

This equation is then used with the boundary condition to give λ_n (or equivalently β).

The boundary condition from diffusion theory is (Zweifel 1973)

$$\frac{I}{2} = -D\frac{\partial I}{\partial \tau} \; . \tag{1.30}$$

where the diffusion constant D in this case equals $1/3$, from Eq. 1.22. This boundary condition says that the number of escaping photons (the right hand side) is equal to half of the number of photons at the boundary (the left hand side). Presumably the other half of the photons are directed back into the cloud due to the assumed isotropy of the photon distribution.

It has been said that this condition holds that no photons are incident on the cloud from the outside. However, diffusion theory speaks only of the nett flow of particles (i.e. photons). Therefore, this condition says that there is no **nett** influx of photons from outside the cloud. Within the framework of diffusion theory, this is the best that can be done.

In practice, even this boundary condition presents difficulties. An easier approach begins by considering the linear extrapolation

$$I(\tau) = I(0)(1 - k\tau) \; . \tag{1.31}$$

Substituting this into the boundary condition (1.30) and solving for k gives $k = 3/2$. So the flux outside the surface of the cloud can be taken to obey

$$I(\tau) = I(0)(1 - (3/2)\tau) \; . \tag{1.32}$$

This says that the intensity goes to zero at a distance $\tau = 2/3$ outside the boundary. This gives a new and simple boundary condition: evaluate the intensity at this point outside the boundary (the so-called extrapolated length) and set it equal to zero. Doing this, one has

$$X_n(-2/3) = 0 \Rightarrow \cos[\lambda_n(\tau_o + 2/3)] = 0 \; , \tag{1.33}$$

so

$$\lambda_n = \frac{(2n-1)\pi}{2(\tau_o + 2/3)} \Rightarrow \beta = \frac{\lambda_1^2}{3} = \frac{\pi^2}{12(\tau_o + 2/3)^2} \; . \tag{1.34}$$

Now that β is known, everything about the distribution of photons over the escape time $P(u)$ is known. It is also seen that the spatial transport depends only on the optical depth τ_o.

This analysis can be repeated for spherical and cylindrical geometries, the principle difference being that the value of β (obtained from the boundary condition) is different.

1.2.4 The stationary equation

Knowing the distribution of photons over the escape time, and given Eq. 1.26, the spectrum from a finite cloud can be found by performing the integration. However, more insight can be gained by using the same equations to derive another equation for the spectrum of a finite cloud, one that is stationary in time.

Begin with the Kompaneets equation Eq. 1.10. It is possible to construct an equation for the time-independent spectrum $N(x)$

$$N(x) = \int_0^\infty n(x,u)P(u)\,du\ . \tag{1.35}$$

by substituting both the Kompaneets expression for $n(x,u)$ and the equation for $P(u)$, Eq. 1.25.

Dropping the $n(x,u)^2$ term in Kompaneets' equation, multiplying each side by $P(u)$ and then integrating gives

$$\begin{aligned}\int_0^\infty \beta\frac{\partial\, n}{\partial u}\exp(-\beta u)\,du &= \frac{\Theta}{x^2}\frac{\partial}{\partial x}x^4\left\{\int_0^\infty \beta n\exp(-\beta u)\,du + \frac{\partial}{\partial x}\int_0^\infty \beta n\exp(-\beta u)\,du\right\} \\ &= \frac{\Theta}{x^2}\frac{\partial}{\partial x}\left[x^4\left(\frac{\partial\, N(x)}{\partial x} + N(x)\right)\right]\ . \end{aligned}\tag{1.36}$$

The left hand side equals

$$\begin{aligned}&[\beta n\exp(-\beta u)]_0^\infty + \int_0^\infty \beta^2 n\exp(-\beta u)\,du \\ &= 0 - \beta n(x,0) + \beta N(x) \\ &= -\frac{\beta f(x)}{x^3} + \beta N(x)\ . \end{aligned}\tag{1.37}$$

where $f(x)$ is a source that is equal to $n(x,0)x^3$. So the equation becomes

$$\frac{1}{x^2}\frac{\partial}{\partial x}\left[x^4\left(\frac{\partial\, N(x)}{\partial x} + N(x)\right)\right] = \gamma N(x) - \gamma\frac{f(x)}{x^3}\ . \tag{1.38}$$

where $\gamma \equiv \beta/\Theta$.

The left hand side is identical to the Kompaneets equation. The first term on the right hand side describes the escape of photons from the plasma cloud, while the second term describes the injection of photons due to a source $f(x)$. The value of γ is given by the spatial diffusion problem.

By looking for a power law solution to the stationary equation of the form

$$N(x) = ax^{-(\alpha+3)} \ . \tag{1.39}$$

it is found that

$$\alpha(\alpha+3) = \gamma = \frac{\pi^2}{12\Theta(\tau_o + 2/3)^2} \ . \tag{1.40}$$

for a slab geometry (using the value of β found earlier).

This quadratic equation can be solved to give

$$\alpha = -\frac{3}{2} \pm \sqrt{\frac{9}{4} + \frac{\pi^2}{12\Theta(\tau_o + 2/3)^2}} \ . \tag{1.41}$$

This equation relates the energy spectral index α to the temperature and optical depth of the cloud. The spectrum produced by inverse Compton scattering depends only on the electron temperature and optical depth. It is also seen that the spectral slope is inversely proportional to Θ and τ_o.

1.2.5 Spectral characteristics

Here the origin of the power law should be clarified. Where does the power law come from? What stops the energy gain from continuing indefinitely?

Consider again Kompaneets' equation with the $n(x,y)^2$ term neglected,

$$\frac{\partial\, n(x,y)}{\partial y} = \frac{1}{x^2}\frac{\partial}{\partial x}\left[x^4\left(\frac{\partial\, n(x,y)}{\partial x} + n(x,y)\right)\right] \ . \tag{1.42}$$

Kompaneets' equation can be used to investigate the rate of energy exchange between photons and electrons, including both Doppler and recoil terms. Recall that the photon occupation number is related to the intensity I by the formula $I = bnx^3$, and the total energy of the photons can be obtained by integrating over the intensity. The rate of energy exchange is therefore

$$\frac{1}{b}\frac{dE}{dy} = \frac{d}{dy}\int_0^\infty n(x,u)x^3\, dx = \int_0^\infty \frac{d\, n(x,u)}{dy}x^3\, dx \ . \tag{1.43}$$

Substituting Kompaneets' equation for $dn(x,u)/dy$ (and ignoring any distinction between partial and total derivatives) gives

$$\begin{aligned}\frac{1}{b}\frac{dE}{dy} &= \int_0^\infty x\frac{\partial}{\partial x}\left[x^4\left(\frac{\partial\, n(x,y)}{\partial x} + n(x,y)\right)\right] dx \\ &= \int_0^\infty x\frac{\partial}{\partial x}\left[x^4\frac{\partial\, n}{\partial x}\right] dx + \int_0^\infty x\frac{\partial}{\partial x}\left[x^4\, n\right] dx \ ,\end{aligned} \tag{1.44}$$

Integrating both terms by parts (twice on the first term), and discarding the boundary terms (because n is taken to be zero at $x = 0,\ \infty$) one has

$$\frac{1}{b}\frac{dE}{dy} = 4\int_0^\infty \left[x^3\, n\right]\, dx - \int_0^\infty \left[x^4\, n\right]\, dx\ . \tag{1.45}$$

For small x, the first term dominates and a first order differential equation for E results

$$\frac{dE}{dy} = 4E\ \Rightarrow\ E = E_0 \exp\left(4\, y\right)\ . \tag{1.46}$$

The gain of energy by the photons from the electrons increases exponentially with time (because y depends linearly on t).

For photons at higher frequencies the second (recoil) term becomes comparable with the first (Doppler) term. To see this, consider those photons at a frequency of $x = 4$, that is, put $n = n_0\, \delta(x - 4)$ into the above expression. This gives

$$\frac{dE}{dy} = 4n_0\, (4)^3 - n_0\, (4)^4 = 0\ . \tag{1.47}$$

That is, no nett energy is transferred to these photons. The Doppler term balances the recoil term. For photons at still higher energies the recoil effect dominates and photons lose energy.

It is seen that for inverse Compton scattering in an infinite medium, no power law is formed (Eq. 1.21). In a medium of finite extent, however, the exponential increase of the photon's energy can be balanced by the rate of escape from the cloud (for instance, the $\beta \exp\left(-\beta u\right)$ function for the distribution of photons over their time of escape from the cloud). This balancing act forms a power law.

The power law does not extend indefinitely in energy, however. As a photon's energy approaches the energy of the scattering electrons the recoil effect becomes important and limits the amount of energy exchanged, until a photon at $x = 4$ experiences no nett gain or loss of energy. A cutoff in the spectrum is therefore produced by the recoil effect when the energy of the photons is approximately the same as the energy of the electrons $\sim kT_e$.

1.3 Compton scattering in astrophysical objects

Astrophysical systems in which Comptonization is an important process include radio-quiet active galactic nuclei, galactic black hole candidates, and magnetised compact stars. These are discussed below.

1.3.1 Disk-corona systems

Active galactic nuclei (AGN) are sources of X-rays and gamma-rays. The standard picture for explaining the required energy release is the accretion of material onto a central supermassive black hole. Accretion is capable of liberating on the order of 10% of the rest-mass energy of the accreting material, and therefore can in principle provide enough power to account for the high energy emission. The accreting material will have angular momentum and therefore will most probably form an accretion disk.

Assuming the accretion energy at a distance r in the disk is dissipated locally, and that the disk is optically thick, the local disk emission will be blackbody (Peterson 1997). Equating the luminosity per unit area of a blackbody sphere of radius r with the Stefan-Boltzmann law σT^4 gives an estimate for the local blackbody temperature, $T_{bb} = (L/4\pi r^2\sigma)^{1/4} \simeq 2\times10^5\ (L/L_{Edd})^{1/4}(r/10r_g)^{-1/2}(M/10^7 M_\odot)^{-1/4}\mathrm{K}$, where L_{Edd} is the Eddington luminosity, $M_\odot$ is the mass of the Sun, M is the mass of the black hole, r_g is the gravitational radius and σ is the Stefan-Boltzmann constant. Thus accretion disks in AGN are a source of optical/UV photons, but are incapable of generating radiation at higher energies through blackbody emission.

In order to explain the observed X-ray emission in AGN spectra, it is necessary to postulate the existence of hot plasma located in the innermost regions of the accretion disk. This hot plasma is typically referred to as a corona (Haardt & Maraschi 1991). The most direct evidence for disk-coronae comes from galactic black hole systems that are approximately edge on to our line of sight: when an eclipse occurs some X-ray flux is still observed. This is interpreted as being due to material above and below the plane of the system scattering X-rays into our line-of-sight.

It is suggested (Liang 1979) that coronae in accreting compact systems cool primarily via the Comptonization process, with the low energy 'soft' photons being Comptonized in the hot corona. The soft photons are emitted by the optically thick accretion disk, and thus have a blackbody distribution. The Comptonized photons form a power law (Section 1.2).

Seyfert galaxies are radio-quiet AGN whose X-ray spectra typically consist of a power law $I_\nu \propto \nu^{-\alpha}$ with $\alpha \sim 1$. Observationally, α is known to be almost constant. A constant α in Eq. 1.40 then implies the existence of some feedback mechanism between the electron temperature and optical depth. If the temperature Θ were to increase (say), the value of the optical depth τ must decrease correspondingly if α is to remain constant. Determining the nature of the feedback mechanism is the focus of *two-phase disk-corona* models (Haardt & Maraschi 1991), where for a given optical depth the temperature is

regulated by photon interaction between the cloud and an accretion disk.

A number of possibilities exist for the geometry of the accretion disk corona in these systems. One possibility is slab-like region located above and below the disk or some portion of the disk. Alternatively, there may be many 'active regions' heated by magnetic fields, which would be distributed over the surface of the disk. The optical depth τ within the corona or active region is thought to be between $10^{-3} - 1$ with the temperature being in the range of a few hundred keV.

1.3.2 Galactic black hole candidates

In the case of galactic black hole candidates (BHCs), two stars orbit about each other, one of which is a compact object. The two types of galactic black hole candidates that can occur are the wind fed system, where material outflowing from the companion star is captured and accreted by the compact object, and the Roche-lobe filling system where the companion is an evolved star (Lewin, van Paradijs & van den Heuvel 1996). Material from the evolved star is transferred to the compact companion by Roche lobe over-flow. In either case the accreting material will have angular momentum, and therefore will form an accretion disk.

The X-ray spectra observed from galactic black hole candidates can be classified into two main states, referred to as a soft state and a hard state (Tanaka & Lewin 1996). The soft state continuum spectrum consists of at least two components; a thermal component with a temperature of the order of 1 keV, and a power law with an energy spectral index α that falls within the range $1.2 - 1.7$, while the hard state consists of a single extended power law with a spectral index in the range $0.4 - 0.9$ (Esin et al. 1998).

The power law spectra are attributed to Comptonization; however the geometry of the Comptonizing plasma is not well understood. The favoured geometry consists of a hot spherical or quasi-spherical region in the central part of the accretion flow (the 'hot' solution of Eardley, Lightman & Shapiro 1975). The mechanism heating the coronal electrons is also not definitively known. However, the electron distribution is most often modeled as being a relativistic Maxwellian distribution of temperature of the order of 100 keV, with an optical depth τ of a few.

1.3.3 Accreting magnetic compact stars

Magnetised white dwarf and neutron stars may accrete material that has overflowed the Roche lobe of a companion star. The accreting (ionised) material is then channeled by

the magnetic field lines of the compact star into an accretion column above the magnetic pole.

Electrons are heated at a standing shock formed near the base of the accretion column, while the radiative cooling of the post-shock electrons is usually considered to be dominated by Bremsstrahlung emission. It is expected that the accretion column will contain both temperature, velocity and density gradients in the post-shock region, as material settles onto the surface of the star.

The hot post-shock material can emit the observed iron Kα and Kβ lines (Fujimoto & Ishida 1997). It is possible for the accretion column to be optically thick to Compton scattering of these line photons, especially within the post-shock region.

1.4 Thesis outline

The outline of this thesis is as follows. Chapter 2 discusses a linear Monte Carlo (MC) numerical technique. Chapter 3 presents a non-linear Monte Carlo code and a method of extending the algorithm to account for density variations. Chapter 4 is an investigation of a two-phase disk-corona model. The linear MC approach is used in Chapter 5 to investigate the time-lags due to Comptonization through a possible coronal geometry for Cyg X-1. Chapter 6 applies the modified non-linear code to a study of Comptonization in bulk accretion flows; in a white dwarf accretion column where the electron density, temperature and velocity are all functions of position in the column, and in a torus of material orbiting around some compact object.

References

Eardley, D. M., Lightman, A. P. & Shapiro, S. l. 1975, ApJ, 199, L153

Esin, A. A., et al. 1998, ApJ, 505, 854

Fujimoto, R. & Ishida, M. 1997, ApJ, 474, 774

Haardt, F. & Maraschi, L. 1991, ApJ, 380, L51

Illarionov, A., Kallman, T., McCray, R., & Ross, R. 1979, ApJ, 228, 279

Liang, E. P. T. 1979, ApJ, 231, L111

Peterson, B. M. 1997, "An Introduction to Active Galactic Nuclei", (Cambridge Univ. Press)

Rybicki, G. B. & Lightman, A. P. 1979, "Radiative Processes in Astrophysics", (New York: Wiley)

Sunyaev, R. A. & Titarchuk, L. G. 1980, A&A, 86, 121

Tanaka, Y., Lewin, W. H. G. 1996, "X-Ray Binaries", eds. W. H. G. Lewin, J. van Paradijs & E. P. J. van den Heuvel (Cambridge Univ. Press.)

Zeldovich, YA. B. & Sunyaev, R. A. 1969, Ap.& Space Sci., 4, 301

Zweifel, P. F. 1973, "Reactor Physics", (New York: McGraw-Hill)

Part II

Technical

Chapter 2

Monte Carlo numerical approach

Comptonization in astrophysical systems is frequently treated using the Monte Carlo method. This Chapter presents an introduction to the numerical techniques used in linear Monte Carlo photon transport codes.

2.1 Monte Carlo photon transport

The diffusion approach discussed in Chapter 1 is limited in a number of ways. The energy diffusion assumption does not hold in most plasmas of astrophysical interest, because the photon energy changes by a large amount at a scattering event. In rarefied plasmas, the distance between scattering events can be large, so the spatial diffusion approximation is also a poor one. In addition, the mean free path of the photons is a function of photon energy as well as plasma density, which also complicates the spatial transport. The situation is further complicated if the geometry of the plasma is not trivial, if other processes (such as absorption) are taken into account, and if complicated photon source functions are to be investigated. Spectra that are formed by this process are therefore more easily calculated using numerical or semi-analytic techniques.

Semi-analytic approaches include the radiative transfer approach (Nagirner & Poutanen 1993) and the kinetic equation approach (Coppi 1992). Of the numerical approaches, the most commonly used is the Monte Carlo technique (MacKeown 1997) for simulating the transport of photons through a plasma. An advantage of using Monte Carlo simulations is their flexibility; these codes can be easily modified to be applicable to many astrophysical settings.

Most Monte Carlo simulations of inverse Compton scattering are ‘analogue’ simula-

tions, so-called because the logical structure of the code is chosen to resemble as closely as possible the physical situation under consideration. The general flow of the Monte Carlo codes considered in this thesis is the following (Pozdnyakov, Sobol & Sunyaev 1983):

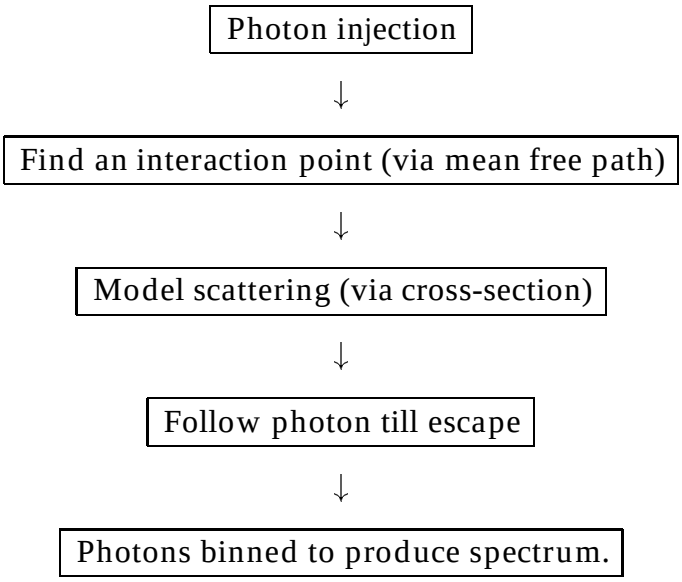

Photons are assigned an energy (from e.g. a blackbody distribution) and injected into the electron plasma with some initial direction of propagation. The distance to a scattering event is determined and the photon is propagated to this point. At the scattering event the energy and direction of the photon changes in a way that is consistent with the differential cross-section and the kinematics of the interaction. The photon continues along its new direction until a new scattering event is reached, or until the photon escapes from the electron plasma. Escaping photons are sorted into energy bins to form a spectrum.

In the case of thermal Comptonization, the code inputs are the Maxwellian electron temperature $\Theta \equiv kT_e/m_ec^2$, and the Thompson optical depth, which for a spherical geometry is $\tau \equiv n\sigma_T R$, where n is the electron density, σ_T is the Thompson cross-section, and R is the radius of the plasma cloud. Although all codes follow this basic pattern, there are two different techniques for determining where an interaction point is located, one due to Pozdnyakov, Sobol & Sunyaev (1983), and the other due to Stern et al. (1995). This thesis presents results from Monte Carlo Comptonization codes developed using both of these techniques, and for the purposes of this thesis I will refer to these codes

as 'linear' and 'non-linear' respectively (even when the 'non-linear' code is being used in a 'linear' mode). Each code was written using algorithms published in Pozdnyakov, Sobol & Sunyaev (1983) and Stern et al. (1995). Other papers discussing the algorithms used for inverse Compton simulations are Górecki & Wilczewski (1984), and Hua (1997).

Below an introduction to the basic Monte Carlo method is given, then the method for modeling electron-photon scattering events is presented in Section 2.1.3. The method of transporting photons through the simulation is discussed in Section 2.1.4. The emphasis in this Chapter is on the methods behind linear Monte Carlo codes, although the modeling of the actual scattering events uses the same algorithm for both the linear and non-linear approaches.

2.1.1 Introduction to the Monte Carlo technique

The Monte Carlo technique can best be illustrated by a physical example. Consider the problem of initially injecting a photon into the electron cloud. Suppose one wishes to assign a frequency to the photon in such a way that after injecting a large number of photons, the distribution of all the injected photons is a blackbody. Essentially the blackbody distribution $B(\nu)$ must be inverted to find a particular value of frequency ν each time a photon is injected. The Monte Carlo technique uses random numbers to do this.

Given the $B(\nu)$ distribution, one way of inverting it would be to integrate over the distribution to find the cumulative probability distribution (CPD). The CPD is by definition a function whose range is between $[0, 1)$. Therefore, one sets the CPD equal to a random number ξ which is evenly distributed between $[0, 1)$ and inverts the CPD to find a value of frequency ν for the photon. This procedure is called *sampling* or *drawing* from the distribution. The technique is a general one, so any distribution (in principle) can be inverted using random numbers. In practice, one hopes that the integration and inversion can be done in closed form, but this is rarely the case.

A number of methods have therefore been constructed to manipulate distributions into a manageable form for sampling. One of these techniques, outlined in the next Section, is the von Neumann rejection technique. The technique can be used to efficiently draw from a blackbody distribution (see Pozdnyakov, Sobol & Sunyaev 1983) and many other distributions, and it is used in the codes described in this thesis.

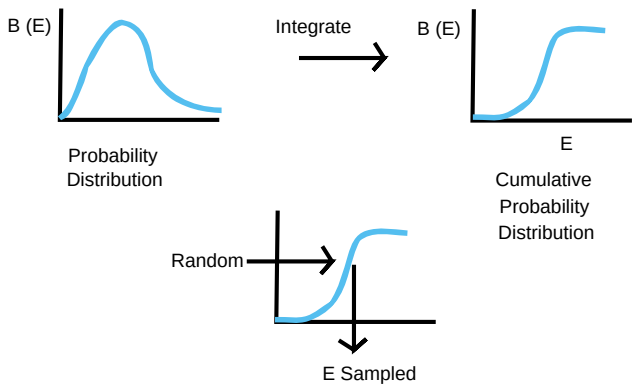

Figure 2.1: Illustration of the basic direct inversion Monte Carlo method

2.1.2 von Neumann method

Many distributions of interest can be written as the product of other distributions. In particular, the differential cross-section for Compton scattering can be written in this form

$$P(x) = F(x)\,G(x)\,. \tag{2.1}$$

If one of these two functions, $G(x)$ say, can be drawn from, and the function $F(x)$ is bounded by some value c, then there exists a technique for using the value of x drawn from one function $G(x)$ to find an x that is drawn from the product $P(x)$. This procedure, originally due to von Neumann, is the following (MacKeown 1997).

1. draw a random number and use it to invert $G(x)$. Let this particular value of x be denoted by χ.

2. Evaluate $F(\chi)$ and compare it with a second random number. If the second random number is greater than $F(\chi)/c$, discard all the values and start again. Otherwise accept x=χ.

This is a *rejection* technique. Not every value x that is drawn is consistent with the distribution $P(x)$. Those values that are not consistent with $P(x)$ are thrown away, and a new attempt is made. This method is particularly useful when one distribution, $G(x)$, say, can be drawn from with ease, and drawing from the other distribution $F(x)$ is difficult. One does not need to draw from $F(x)$, but simply evaluate it for some $x = \chi$.

2.1.3 Modeling a scattering event

Finding an electron

Pozdnyakov, Sobol & Sunyaev (1983) and Górecki & Wilczewski (1984) have used the von Neumann technique to sample from the distributions describing a scattering event. The following discussion outlines how this method is implemented in linear Monte Carlo codes.

Consider a photon propagating in some direction $\mathbf{\Omega}$ with some energy $h\nu$. First, an electron must be found to interact with the photon. Therefore one needs to consider the distribution of scattering electrons, which is of the form

$$\hat{\sigma}(x)\,(1-\mathbf{\Omega}.\mathbf{v}/c)\,N(p)\;, \tag{2.2}$$

where $N(p)$ is the momentum distribution for the electrons, **v** is the direction of electron motion, and $\hat{\sigma}(x)$ is the cross-section with

$$x \equiv 2\left(\frac{h\nu}{m_e c^2}\right)\gamma(1-\mathbf{\Omega}.\mathbf{v}/c)\;, \tag{2.3}$$

where γ is the electron Lorentz factor and ν is the photon frequency.

In the case where the electron distribution $N(p)$ is Maxwellian ($N(p) \equiv n_e(p)$), an algorithm for sampling $N(p)$ is known. It can also be shown that the pre-factor $f(x)$ is bounded,

$$f(x) \equiv \hat{\sigma}(x)\,(1-\mathbf{\Omega}.\mathbf{v}/c) \;\leq\; 2\hat{\sigma}(x) \;\leq 8/3\;. \tag{2.4}$$

Therefore, one can sample the Maxwellian distribution and then use the von Neumann method to sample the product Eq. 2.2. The method is

1. Draw a value for the electron momentum from $N(p)$, and a direction of motion for the electron from an isotropic distribution,

2. Use these values to evaluate $f(x)$,

3. if a random number ξ is

$$\xi \;<\; (3/8)\,\hat{\sigma}(x)\,(1-\mathbf{\Omega}.\mathbf{v}/c)\;, \tag{2.5}$$

   then accept the electron momentum p and direction of motion v, else

4. reject the electron values and draw new values for the electron momentum and direction.

The scattering event

Having found an electron to scatter with the photon, it is then necessary to find a new direction of propagation and a new energy for the photon after the scattering event. This is done by sampling the Klein-Nishina differential scattering cross-section (see Chapter 1).

The differential cross-section can be written as a product of the form

$$P(\mu,\varphi)\,Y \tag{2.6}$$

where

$$P(\mu,\varphi) = \frac{1}{4\pi\gamma^2(1-\mu v/c)^2}\ , \tag{2.7}$$

with μ being the angle cosine between the electron and the photon and v the electron velocity. The other part of the product has the following form

$$Y \equiv \left(\frac{x^{'}}{x}\right)^2 \Psi(x,x^{'})\ , \tag{2.8}$$

$$\Psi(x,x^{'}) \equiv \frac{x}{x^{'}} + \frac{x^{'}}{x} + 4\left(\frac{1}{x}-\frac{1}{x^{'}}\right) + 4\left(\frac{1}{x}-\frac{1}{x^{'}}\right)^2\ , \tag{2.9}$$

with

$$x \equiv 2\left(\frac{h\nu}{m_e c^2}\right)\gamma(1-\mu v/c) \quad \text{and} \quad x^{'} \equiv 2\left(\frac{h\nu^{'}}{m_e c^2}\right)\gamma(1-\mu^{'} v/c)\ . \tag{2.10}$$

The function Y is bounded ($Y \leq 2$), and can be evaluated easily if x and $x^{'}$ are known. The prime denotes quantities after scattering. The angular factor $P(\mu,\varphi)$ can be inverted directly (Section 2.1.1) for the scattering angles:

$$\mu = \frac{v/c + (2\xi - 1)}{1 + (v/c)(2\xi - 1)} \tag{2.11}$$

$$\varphi = 2\pi\xi_1\ . \tag{2.12}$$

where ξ and ξ_1 are uniform random numbers on [0,1). Using these angles a new direction of propagation $\mathbf{\Omega}^{'}$, and the cosine of the scattering angle $\mathbf{\Omega}.\mathbf{\Omega}^{'}$, can be computed. The function Y is then found by evaluating Ψ where

$$\frac{x^{'}}{x} = \left[1 + \frac{h\nu(1-\mathbf{\Omega}.\mathbf{\Omega}^{'})}{\gamma m_e c^2(1-\mu v/c)}\right]^{-1}\ . \tag{2.13}$$

The differential cross-section then consists of one part that can be sampled ($P(\mu,\varphi)$, Eq. 2.11 and Eq. 2.12), and another part (Y) that is bounded and that can be evaluated

given the angles. Therefore the rejection test can be applied for sampling the differential cross-section (Eq. 2.6). The procedure is

1. Draw from the angular factor $P(\mu, \varphi)$ using Eq. 2.11 and Eq. 2.12, and use them to find $\mathbf{\Omega}.\mathbf{\Omega}^{'}$

2. Use the parameters of the photon, the electron and $\mathbf{\Omega}.\mathbf{\Omega}^{'}$ to compute Y.

3. If a random number $2\xi_2 < Y$ then set $\mathbf{\Omega} = \mathbf{\Omega}^{'}$, and the new energy of the photon is

$$E^{'} = x^{'}[2\gamma(1 - \mu v/c)]^{-1} m_e c^2 \ , \tag{2.14}$$

   else

4. reject the scattering event, draw another two angles $\mu \, \text{and} \, \varphi$, and try again with the same electron.

2.1.4 The photon transport technique

In addition to modeling scattering events, the other key technique required for linear Monte Carlo simulations is a method for transporting the photons from one scattering event to the next. In a linear code, the following procedure is used.

The distance l to the next scattering point is determined by inverting the cumulative probability distribution

$$\xi = \exp(-\tau) \equiv \exp\left(-\int_0^l n(s)\sigma \, ds\right) , \tag{2.15}$$

where ξ is a uniform random number between zero and one and the cross-section σ has been averaged over the distribution of target electrons. For a constant density $n(s) = n$, the expression becomes

$$l = -\frac{1}{n\sigma}\ln(\xi) \ . \tag{2.16}$$

or

$$l = -\overline{\lambda}\ln(\xi) \ , \tag{2.17}$$

where $\overline{\lambda}$ is the mean free path. In the linear simulation, the mean free path is determined by averaging the cross-section over the Maxwellian electron momentum distribution $n_e(p)$, which in spherical polar co-ordinates takes the form

$$\overline{\lambda} = \frac{4\pi \int_0^\infty n_e(p) p^2 \, dp}{2\pi n_e \int_0^\infty n_e(p) p^2 \int_{-1}^1 \sigma_{KN}(x)(1 - \mu v/c) \, d\mu \, dp} \tag{2.18}$$

(Pozdnyakov, Sobol & Sunyaev 1983) with x defined in Eq. 2.10. Given a photon propagating in a direction Ω and with $\mathbf{r}$ being the current position of the photon in the simulation, the new position $\mathbf{r}'$ of the photon is then

$$\mathbf{r}' = \mathbf{r} + l\Omega \, . \tag{2.19}$$

This technique, while being very clear and obvious, is limited because the method for calculating the mean free path $\overline{\lambda}$, Eq. 2.18, has assumed the electron plasma is homogeneous and isotropic. If bulk flows of electrons exist in the plasma, evaluating the mean free path integral becomes more difficult (Janiuk, Czerny & Zycki 2000).

2.2 Summary

In this Chapter, the structure of linear Monte Carlo photon transport codes has been reviewed, including an introduction to the basic Monte Carlo technique. Section 2.1.3 gave a discussion of how scattering events are modeled, and Section 2.1.4 discussed how a photon is transported through a plasma of constant density. Although the linear Monte Carlo procedure as outlined in this Chapter is a flexible way of treating the Comptonization problem, the next Chapter introduces (and modifies) the non-linear approach to make the numerical method even more flexible.

References

Coppi, P. S. 1992, MNRAS, 258, 657
Górecki, A. & Wilczewski, W. 1984, Acta Astron., 34, 141
Hua, X. 1997, Com. Ph. 11, 660 (physics/9709023)
Janiuk, A., Czerny, B. & Zycki, P. T. 2000, MNRAS, 318, 180
MacKeown, P. K. 1997, "Stochastic Simulation in Physics", (Springer-Verlag, Singapore)
Nagirner, D. I. & Poutanen, J. 1993, A&A, 275, 325
Pozdnyakov, L. A., Sobol, I. M. & Sunyaev, R. A. 1983, Ap.& Space Sci. Reviews, 2, 189
Stern, B., et al. 1995, MNRAS, 272, 291

Chapter 3

Photon transport through plasmas with density and velocity structure

Linear Monte Carlo codes (Chapter 2) are typically applied to scattering in plasmas without temperature and density gradients. Treating bulk motion can be difficult even for simple cases. With the introduction into the field of algorithms associated with non-linear Monte Carlo (NLMC) codes, these problems are now more tractable numerically. NLMC can already handle arbitrary velocity structures in a plasma. Here the NLMC technique is discussed, and an extension of the algorithm is proposed that enables the easy calculation of photon transport in plasmas with non-constant density as well as non-constant temperature and / or bulk motion.

3.1 Overview

Monte Carlo simulations of photon scattering are analogue simulations. As discussed in the previous Chapter, after a photon of some energy is injected into the plasma, the location of the next scattering point is sampled using the mean free path. The scattering event is modeled by sampling the differential cross-section, and the new energy and new direction is assigned to the photon. The photon is followed until it escapes the plasma. After following many photons a spectrum is generated. A weighting technique (see Section 3.4.1) is generally used to treat the spatial transport, whereby a weighted fraction of the photon is forced to scatter, while the rest of the photon escapes. The weight function is determined at each scattering point by the probability of escape from the plasma (Molnar & Birkinshaw 1999). This is useful when the probability of a given

photon undergoing a scattering event is very small.

A linear algorithm (Pozdnyakov, Sobol, & Sunyaev 1983) has been used to treat the Comptonization problem in regions where the plasma has a well defined temperature and a homogeneous density. However, astrophysical plasmas are often inhomogeneous and non-isothermal. Additionally, treating bulk motion of the plasma with such a code is difficult even for simple cases.

By dividing the plasma into various zones, with each zone having a different temperature and density, temperature and density variations can be studied in a crude way, for instance, by having the density decrease in a series of steps. An improvement on this situation was made by Hua (1997), who developed a code to treat smooth density variations; however the plasma was still required to be isothermal, and no bulk motion was considered.

As an alternative, the non-linear algorithm was introduced by Stern et al. (1995). The main difference in this non-linear approach is the way the photons are transported, since this method uses a von Neumann rejection algorithm for finding the location of the next scattering point. In the following Section the method of photon transport currently used by non-linear Monte Carlo methods is reviewed. Section 3.3 presents a method of combining the Hua and Stern algorithms that enables the treatment of smooth density variations in the presence of temperature variations and bulk motion. Sections 3.4 and 3.5 discuss implementation of the modification and give examples of astrophysical applications. Detailed discussions of how to model the actual scattering events have been given by Pozdnyakov, Sobol & Sunyaev (1983), Gorecki and Wilczewski (1984), Hua (1997), and in Chapter 2 of this thesis.

3.2 Non-linear Monte Carlo simulation

3.2.1 Conventional algorithm

A photon has a certain probability of interacting with each of the electrons around it. Each of these probabilities can be written as a partial interaction rate,

$$P_{iT} = \frac{\sigma}{\mathrm{vol}} \mathrm{V}_{rel} \ . \tag{3.1}$$

where V_{rel} is the relative velocity between the photon and a given electron, vol is the volume of the plasma-filled region, and σ is the cross-section. The subscript i denotes the incident particle, and the subscript T the target particle.

To find the total interaction rate, that is, the total number of scattering events per second, one sums all the partial interaction rates,

$$P_i = \sum_T P_{iT} \ . \tag{3.2}$$

The time of flight to the next scattering event is then sampled with the expression

$$t = -\frac{\ln(\xi)}{P_i} \ , \tag{3.3}$$

where ξ is a random number uniformly distributed on $[0, 1)$ (Chapter 2). This time can be converted into the distance propagated l by including a factor of c. An electron is chosen to interact with the photon based on the partial interaction rates, and then the scattering event is simulated using the technique described previously in Section $2.1.3$.

3.2.2 Current non-linear Monte Carlo method

Stern et al. (1995) proposed a technique that increases efficiency by making use of the concept of a virtual cross-section (Woodcock et al. 1965, Nelson, Hirayama & Rogers 1985). This technique enables the simulation of photon scattering by electrons in bulk flow.

The rate of scattering events for a beam of photons (where the beam consists of a single photon, say) incident with a beam of electrons at some point is $n\sigma_{\rm KN}V_{\rm rel}$, with n the electron density at the point. This quantity, which is used to determine if a scattering event takes place, depends on the photon's energy through the Klein-Nishina cross-section $\sigma_{\rm KN}$, and the energy of the electrons through the relative velocity $V_{\rm rel}$.

In the case of a photon interacting with electrons, the relativistic expression for scattering rate is (Landau & Lifshitz 1971)

$$\sigma_{\rm KN}\frac{P_{1\mu}P_2^{\mu}}{E_1E_2}\,n \tag{3.4}$$

where $P_{1\mu}$ is the momentum four-vector of particle 1, P_2^{μ} is the momentum four-vector of particle 2, E_1 and E_2 are the energies of particles 1 and 2, $\sigma_{\rm KN}$ is the cross-section and n is the density of target particles, in this case electrons.

The four-vector contraction is $P_{1\mu}P_2^{\mu} = E_1E_2 - \mathbf{p_1}\mathbf{p_2}$ where $\mathbf{p_1}$ and $\mathbf{p_2}$ are the momentum vectors of the particles, and so

$$\frac{P_{1\mu}P_2^{\mu}}{E_1E_2} = \frac{E_1E_2 - \mathbf{p_1}\mathbf{p_2}}{E_1E_2} = (1 - \frac{\mathbf{p_1}}{E_1}.\frac{\mathbf{p_2}}{E_2}) = (1 - \mathbf{\Omega}.\mathbf{v}) \tag{3.5}$$

where $\mathbf{\Omega}$ is the unit vector in the photon propagation direction and $\mathbf{v}$ is the electron velocity vector, and units where $c \equiv 1$ have been assumed. On comparison of Eq. (3.4) with $n\sigma_{\rm KN}V_{\rm rel}$, one sees that correct scattering rates are obtained if the quantity $(1-\mathbf{\Omega}.\mathbf{v})$ is identified as $V_{\rm rel}$.

The non-linear simulation is divided into a series of time steps, with multiple photons being followed simultaneously (their parameters being stored in arrays). Within each time step, and for each photon, the interaction rate (above) is used to sample the time between scattering events (which must be smaller than the time step), rather than the distance (Eq. 2.16), with

$$t = -\frac{1}{n\sigma_{\rm KN}V_{\rm rel}}\ln(\xi)\ , \tag{3.6}$$

where $n\sigma V_{\rm rel}$ is the rate of scattering events, and it has been assumed that all the electrons have the same $V_{\rm rel}$. This is, of course, an approximation. Each electron has a different velocity $V_{\rm rel}$ relative to the photon. The real interaction rate (which for a complicated situation is difficult to evaluate) is the sum of all the partial interaction rates of all the electrons in the plasma. One does not wish to sum over all the electrons in the simulation, so the algorithm used by non-linear codes assumes the existence of a virtual process, such that

$$n(\sigma_{\rm KN} + \sigma_{\rm virt})V_{\rm rel} \equiv n\sigma_{\rm T}2c \tag{3.7}$$

(Stern et al. 1995), where $\sigma_{\rm virt}$ is the cross-section of the virtual process and σ_T is the Thompson cross-section. If scattering in regions of homogeneous density is to be considered, n can be dropped from the above to give

$$(\sigma_{\rm KN} + \sigma_{\rm virt})V_{\rm rel} = \sigma_{\rm T}2c\ . \tag{3.8}$$

The purpose of introducing the virtual process is that the right hand side of Eq. 3.7 is an upper limit on the real interaction rate, and is constant along the photon's path, so it is easy to use this value to sample the time to the next interaction event with

$$t = -\frac{1}{n\sigma_{\rm T}2c}\ln(\xi)\ . \tag{3.9}$$

An electron for the photon to scatter with is then found. But, having used the RHS of Eq. 3.7, the virtual (unphysical) process or channel must be disregarded to determine if a real scattering event takes place. To put it another way, at each point along the trajectory the probability of an interaction is the sum of the probability of the virtual process occurring, and the probability of the real process occurring. Therefore, the real scattering event (or channel) is accepted / selected with a probability $(\sigma_{\rm KN}V_{\rm rel})/(\sigma_{\rm T}\ 2c)$,

otherwise the event is rejected as being due to the virtual process, and the photon continues without scattering until the next time step.

This rejection algorithm is efficient unless the electron is moving relativistically in the same direction as the photon, in which case $V_{\rm rel}$ becomes small, and if the photon energy is very large, in which case the cross-section $\sigma_{\rm KN}$ becomes small. The benefits of such a procedure are

- it can be extended easily to include other processes,
- no integrals for determining the mean free path through the electrons are required, and
- because finding a tentative scattering point does not require any knowledge of the velocity structure in the accretion flow, this algorithm can easily handle problems where there is bulk motion of the flow, as expected for accretion problems.

Figure 3.1 shows spectra that result when this procedure is implemented, in this case for a homogeneous sphere of plasma with electron temperature 25 keV. Solid lines are output from the non-linear code and dotted lines from the linear code (see Chapter 2). Five different optical depths for the sphere are considered, 3, 4, 5, 7 and 10. The photons that are initially injected into the plasma are sampled from a blackbody distribution with a temperature equivalent to $10^{-8} m_e c^2$. The results are consistent with the results obtained using the linear algorithm of Pozdnyakov, Sobol & Sunyaev (1983).

To use the NLMC method to treat bulk motion of the flow, first determine a (potential) scattering point using $n\sigma_{\rm T}2c$ as the rate of scattering events (Eq. 3.7). One then determines the direction and momentum of the flow. This gives the relative velocity of the electron that is needed for the rejection test. One then calculates the real cross-section and accepts or rejects the scattering event using $(\sigma_{\rm KN}V_{\rm rel})/(\sigma_{\rm T}\ 2c)$. If the event is rejected the photon continues on its way until the next time step. If studying an accretion flow with a temperature gradient at the tentative scattering point, determine what the temperature is at this point, draw an electron from a distribution with this temperature, and then decide to accept or reject the scattering event.

3.3 Refined algorithm

The previous section assumed an interaction rate $n\,\sigma_{\rm T}\,2c$ that is constant along the photon's path, because the density is taken to be a constant. Hua (1997) described how a

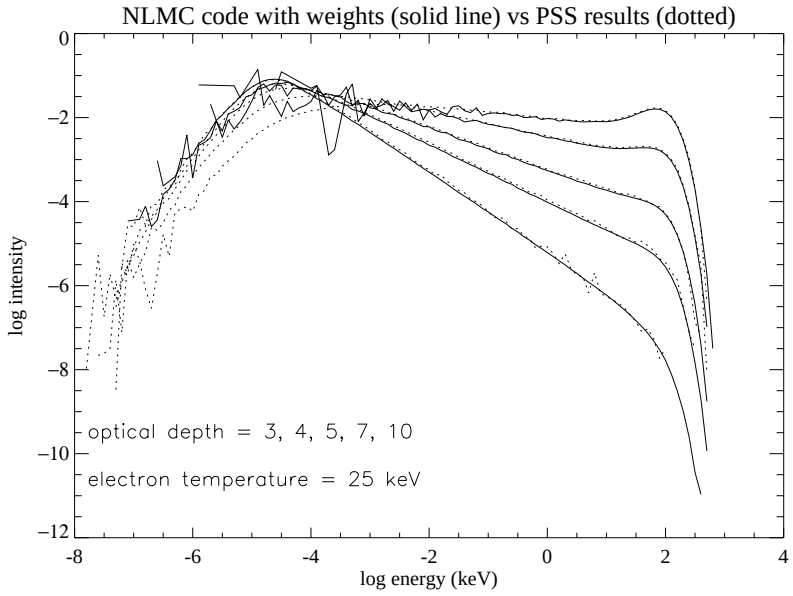

Figure 3.1: Test runs comparing the output spectrum of the non-linear and the linear code for a sphere of plasma, of different optical depths. Log of intensity is on the vertical axis and log of photon energy is on the horizontal axis.

non-constant density profile can be integrated over to find the next scattering point using an expression equivalent to Eq. 2.15. In that work, the procedure was implemented for an isothermal plasma with an r^{-1} and $r^{3/2}$ density profile, using a linear code. This idea can be included in the NLMC method by considering that instead of sampling the next scattering point using $n\,\sigma_{\rm T}\,2c$, one samples the scattering location by integrating over a non-constant density profile. The interaction rate at each point is now given by $n(s)\;\sigma_{\rm T}\;2c$, where $n(s)$ is the electron density along a photon path parameterized by s.

To sample the time between scattering events for the case where the density (i.e. the interaction rate) along the photon trajectory is not constant, Eq. 3.9 is generalised to

$$\xi = \exp(-\int_0^{2ct} n(s)\sigma_{\rm T}\;ds)\;, \tag{3.10}$$

(c.f. Eq. 2.15) or rearranging,

$$\int_0^{2ct} n(s)\sigma_{\rm T}\;ds = -\ln(\xi)\;. \tag{3.11}$$

If $n(s)$ is constant then the above reduces to Eq. 3.9. The factor of $2c$ in the upper limit of the integral is required because the rate of scattering events is assumed to be given

by $n(s)\,\sigma_{\rm T}\,2c$. The distance to the next scattering point is then just the time multiplied by the speed of light.

The distance above can be thought of as an lower limit on how far the photon actually travels, because it uses an upper limit on the interaction rate. In reality, the cross-section is not $\sigma_{\rm T}$ and the relative velocity is not $2c$. So this scattering point is only 'tentative'.

Having found a tentative interaction point using the above method, the real interaction rate at the scattering point plus the virtual interaction rate is taken to be

$$n(s)(\sigma_{\rm KN} + \sigma_{\rm virt})V_{\rm rel} \equiv n(s)\ \sigma_{\rm T}\ 2c\ . \tag{3.12}$$

So one accepts the tentative scattering event with probability

$$\frac{n(s)\ \sigma_{\rm KN}\ V_{\rm rel}}{n(s)\ \sigma_{\rm T}\ 2c} \quad = \quad \frac{\sigma_{\rm KN}\ V_{\rm rel}}{\sigma_{\rm T}\ 2c}\ . \tag{3.13}$$

This procedure is analogous to that described in the previous Section. Note that no integral is required in Eq. 3.13 as the expression is evaluated at the (potential) scattering point, not along the photon's path (however the integral in Eq. 3.10 is along the photon's path). To summarise the extended algorithm, a particular interaction rate ($n(s)\,\sigma_{\rm T}\,2c$) has been *assumed* to hold at all points along the photon's path. This enables the distance to the next scattering point to be sampled with ease (Eq. 3.11) using the Hua method. However, by assuming an interaction rate $n(s)\,\sigma_{\rm T}\,2c$, the number of scattering points along a trajectory has been over-sampled. Some scattering points must be rejected to give a physical simulation. At each (potential) scattering point, the fraction of scattering events that are kept (accepted as being due to the physical cross-section) is given by Eq. 3.13, with the rejected scattering points being due to the virtual cross-section.

The only difference between this proceedure and the conventional (Stern) algorithm is that one is now performing the distance integral explicitly, rather than using an expression that can be integrated in closed form and inverted. This procedure is valid in the relativistic limit and is exact: no approximations have been made.

3.4 Implementation of the method

This modified algorithm can still be used if photons are weighted in energy (in fact, this is often required for good spectral resolution, Stern et al. 1995). Note also that the efficiency of accepting a scattering event is independent of the density at that point, because $n(s)$ has canceled in Eq. 3.13. The integration over the density profile is now the

most time-intensive part of the simulation. Once a scattering point is accepted a simple evaluation of the velocity profile or temperature profile gives the electron properties required for modeling the electron / photon scattering event. It is not necessary to search through an array of electrons (Stern et al. 1995), because electrons are not followed in the simulation. The velocity or temperature profiles (specified beforehand) give all the information about the electrons at the scattering point. This increases the speed of the code but also means the code cannot treat processes where electrons must be followed (i.e. pair annihilation). The main advance is that arbitrary density and temperature gradients, with or without bulk motion, can be considered without recourse to zones. Furthermore, this can be done while retaining all of the features that have made Monte Carlo codes popular, such as the capacity to treat complex geometries and source functions.

As for how such an algorithm may be used, it can be used to consider bulk motion or temperature gradients, as before, but now it can also be used to study density gradients. For instance, Hua's model can be extended to include temperature gradients. A mixture of thermal and bulk motion for the electrons can be studied at the tentative scattering point, by first considering a frame instantaneously co-moving with the flow so that an electron can be drawn from a Maxwellian distribution and assigned a random direction of motion. Having the electrons (thermal) properties, a Lorentz Transform can be performed out of the flow frame and into the laboratory frame to obtain the resultant vector. This vector (momentum and direction of the electron) is then sent to the rejection algorithm Eq. 3.13 to determine if the interaction is accepted or not. This has numerous applications in high energy astrophysics, such as line scattering in accretion columns with density, temperature and velocity structure in magnetic cataclysmic variables and X-ray pulsars, or accretion flows surrounding black holes.

3.4.1 An illustrative example

As an example of the technique discussed above, photon scattering by cold and freely-falling electrons is considered. The geometry of the electron plasma is assumed to be spherical, with the photon source located at the centre. Two different photon source functions are specified; a line at 6.4 keV and a power law extending from $2 - 100$ keV. A line source function is common in X-ray astrophysics, while a power law source function will be used in Chapter 6 to study the interaction between coronal (power law) photons and an accretion disk. In this Chapter one might imagine the power law being produced in a central corona, with subsequent scattering events taking place in

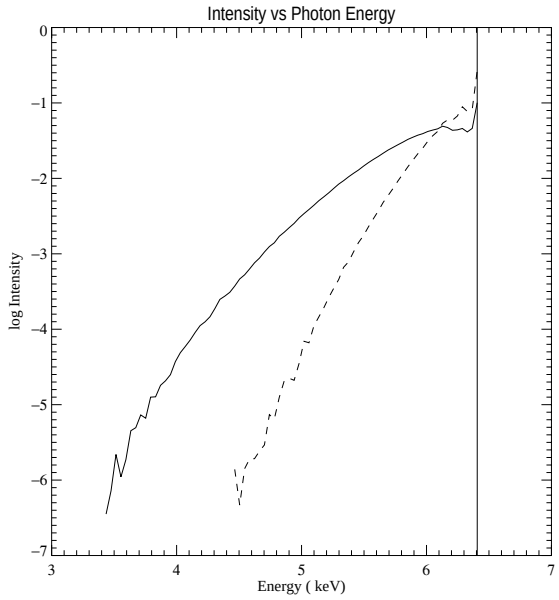

Figure 3.2: Scattering of a 6.4 keV line by cold electrons.

surrounding material. Previous treatments of this problem have had to assume a cross-section constant with energy and slowly moving electrons (Colpi 1988). Here the Klein-Nishina cross-section is used, with no restriction on the electron velocity.

Firstly, figure 3.2 shows a Comptonized line with injected energy of 6.4 keV. The solid curve represents the photon spectrum after scattering in a sphere of cold (stationary) electrons of Thompson optical depth $\tau = 3.0$, while the dashed line represents the resultant spectrum after scattering with cold electrons with a radial density profile of the form

$$n(r) = n_0 \, (\frac{r}{R} + 1)^{-3/2}, \tag{3.14}$$

with n_0 is the density at the origin defined so that a sphere of constant density n_0 would have a Thompson optical depth of 3.0. Both lines are injected at the origin (centre of the sphere). This demonstrates that line broadening occurs due to electron scattering in both cases.

Figure 3.3 shows the same 6.4 keV line scattering through the same density gradient, but where a velocity gradient of the form

$$v(r) = v_0 \, (\frac{r}{R} + 1)^{-1/2} \ . \tag{3.15}$$

has been added. A density profile $\propto r^{-3/2}$ and a velocity profile $\propto r^{-1/2}$ are appropriate

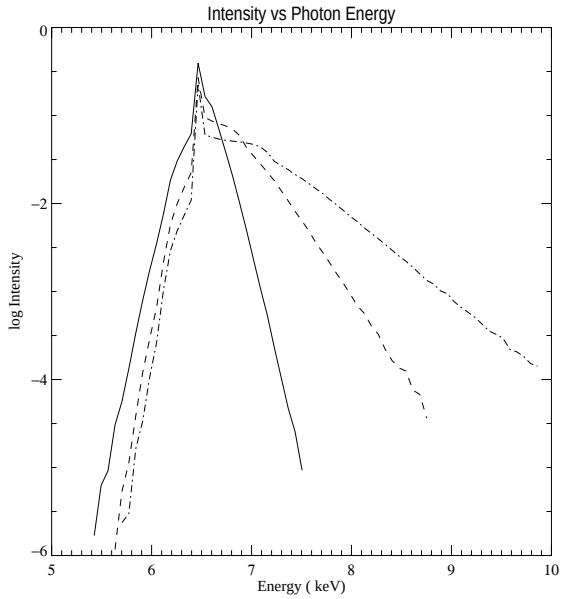

Figure 3.3: Scattering of a 6.4 keV line by freely-falling electrons.

for electrons that are falling freely under gravity onto some accreting object. The solid, dashed and dot-dashed curves in figure 3.3 correspond to $v_0/c = 0.03, 0.05$ and 0.07 respectively. It is evident that the slope of the high-energy wing of the line depends on v_0.

Figure 3.4 shows the distortion of a power law of spectral index $\alpha = 1.0$ due to scattering by cold electrons in a spherical geometry. The solid curve is the injected power law, which extends from 2 keV to 100 keV. The power law photons are injected at the origin of the sphere. The dashed curve is the resulting Compton scattered spectrum for a sphere of constant density and optical depth $\tau = 3.0$. The dot-dashed curve represents the result of scattering by cold electrons with a density profile given by Eq. 3.14. The presence of the density gradient pushes up the energy at which the break in the power law occurs, because there is less total optical depth from the centre to the edge of the sphere so fewer scattering events take place.

Figure 3.5 shows the distortion of a power law of spectral index $\alpha = 1.0$ due to scattering by electrons with a density profile given by Eq. 3.14, and a velocity profile given by Eq. 3.15. The dot-dot-dot-dashed, dot-dashed, short-dashed and long-dashed curves correspond to a v_0/c of 0.1, 0.3, 0.6 and 0.8, respectively (the long-dashed curve has been shifted downwards compared to the other curves because extra energy bins

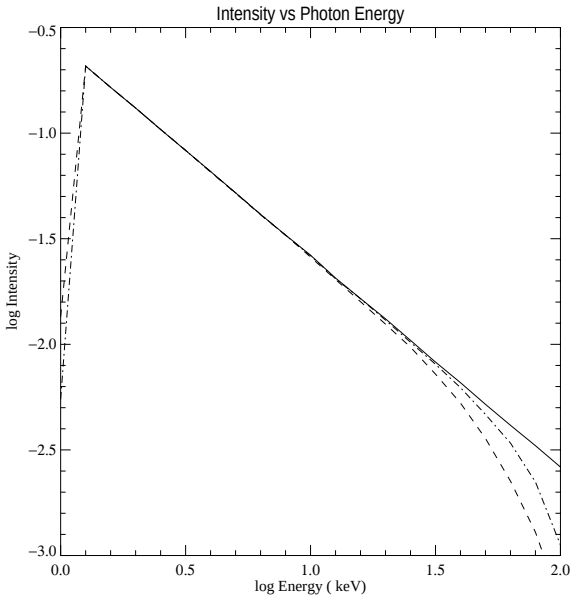

Figure 3.4: Scattering of power law photons by cold electrons with constant density and by electrons with a density gradient.

were used for this case). For low velocities the spectrum has almost the same form as for the cold electron case. As the velocity increases, curvature is introduced into the power law, then the power law becomes flat ($\alpha \sim 1.0$). At large velocities a peak is formed above 100 keV.

Low optical depth

Low optical depths present a problem as many photons can be injected and then escape without scattering at all. The problem of scattering at low optical depths has been treated with linear codes using a technique of forced scattering. Each simulation photon carries a number or 'weight', which describes the number of 'real' photons it corresponds to. Instead of the usual method of finding the scattering point, the normalisation of the cumulative distribution function is changed to force the photon to scatter in the plasma,

$$\xi = \frac{(1 - e^{-n\sigma l})}{(1 - e^{-n\sigma d})} \, , \tag{3.16}$$

where d is the distance to the edge of the cloud along the photon's path and l is the distance the photon travels (constant density has been assumed for this Section). Inverting

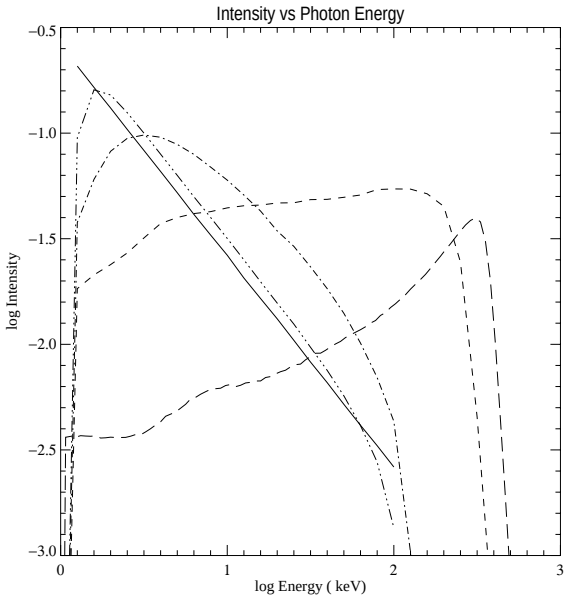

Figure 3.5: Scattering of power law photons by freely-falling electrons.

this for l gives

$$l = -\frac{1}{n\sigma}\ln\left[1 - \xi(1 - \mathrm{e}^{-\mathrm{n}\sigma\mathrm{d}})\right] \ . \tag{3.17}$$

To make this procedure physical, the photon's weight w_{old} is then changed so that part of the weight associated with the photon escapes from the plasma and is binned. The photon (with a suitably reduced weight) continues scattering inside the cloud. The escaping weight has the value

$$w_{esc} = w_{old}e^{-n\sigma d}, \tag{3.18}$$

while the photon weight is given the new value

$$w_{new} = w_{old} - w_{esc}. \tag{3.19}$$

After following many photon trajectories the escaping weights w_{esc} build up the resulting spectrum. This procedure has been used to investigate the Sunyaev-Zeldovich effect (Molnar & Birkinshaw 1999).

This procedure can also be made to work for NLMC transport. This enables investigation of bulk motion scattering and scattering through temperature gradients in low optical depth plasmas without making approximations.

Consider a simulation photon at some point in the plasma, and take $\sigma = \sigma_T$ in the above expressions. A fraction of the weight given by Eq. 3.18 escapes and is binned.

Eq. 3.17 is then used to find a tentative scattering point. Note that the escaping fraction of the weight is binned whether or not the tentative scattering event is accepted or not. The photon then has its weight adjusted. If the scattering event is accepted the photon changes energy and direction, and the simulation proceeds. If the scattering event is rejected, the photon location is updated to the location of the tentative scattering point and another tentative scattering point is drawn without changing the photon's direction. The photon can 'step' its way through the plasma with part of its weight escaping at each 'step' even if it is not scattering.

This procedure has been used to produce the curves in figure 3.6. The solid curve is a blackbody spectrum injected at the origin of a sphere of constant density. The optical depth of the sphere is $\tau = 0.001$. The dashed line is the resulting Comptonized spectrum for an isothermal plasma of temperature 250 keV, while the dot-dashed line is produced by bulk motion Comptonization in a converging spherical flow of constant density. The flow is directed towards the origin at the centre of the sphere, and the flow velocity is constant and set equal to $v/c = 0.67$. The optical depth is again $\tau = 0.001$. Different velocity profiles and/or temperature profiles can be included as described in Section 3.4. This is a flexible way of treating velocity and temperature gradients in low optical depth plasmas.

3.5 Some remarks

The NLMC transport method has been extended to include density gradients. This could have various applications in astrophysics where plasmas may not be homogeneous and isothermal. The density can be smoothly varying, and density zones are not required. The method of forced scattering has also been demonstrated to work within the framework of the NLMC method, meaning that plasmas containing temperature and velocity structure can now be considered even if the scattering plasma is of small optical depth.

One of the original reasons the NLMC codes were developed was to study the cooling of a plasma by inverse Compton scattering in a self consistent manner. An example of such a calculation has been given by Malzac & Jourdain (1999), where the optical depth of a homogeneous plasma is allowed to vary until the rate of energy loss through scattering events equals the rate of energy injection in the form of new particles. In principle this is still possible for the modified algorithm considered here, by fixing the shape of the density and temperature distributions, while allowing the normalization

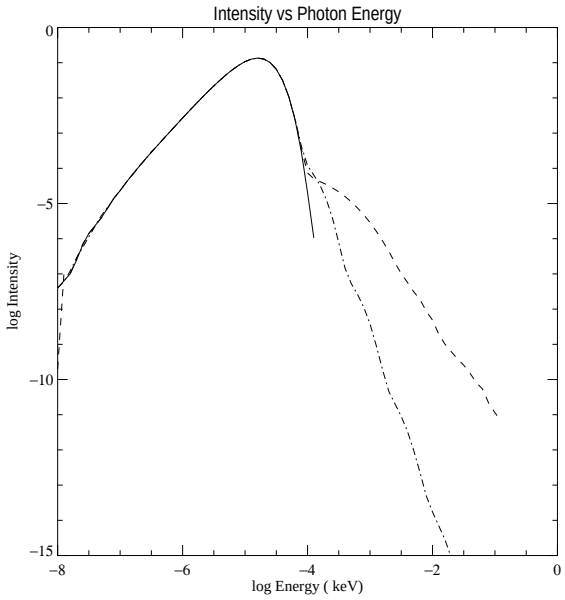

Figure 3.6: Bulk motion scattering for $\tau = 0.001$, and thermal scattering for $\tau = 0.001$, for blackbody source photons.

of the density profile to move up and down. This corresponds to injecting more electrons or removing electrons, until the rate energy is removed equals the rate energy is being injected (which would be calculated by integrating over the density and temperature distributions). Such calculations are more demanding than pure Comptonization problems, and so have not been considered here.

A restriction on the method is that only photons are followed in the code, which means that it cannot, for instance, study electron-positron pair cascades. In other respects it is a flexible way of treating the Comptonization problem.

References

Colpi, M. 1988, ApJ, 326, 223

Gorecki, A. & Wilczewski, W. 1984, Acta Astron., 34, 141

Hua, X. 1997, Com. Ph. 11, 660 (physics/9709023)

L. D. Landau, L. D. & E. M. Lifshitz, E. M. 1971, "The Classical Theory of Fields", Chapter 2, Section 12, (3rd edition, Pergamon Press)

Malzac, J. & Jourdain, E. 1999, Pro. third INTEGRAL workshop, astro-ph/9901186

Molnar, S. M. & Birkinshaw, M. 1999, ApJ, 523, 78 (astro-ph/9903444)

Nelson, W. R. Hirayama, H. & Rogers, D. W. O. 1985, "The EGS code system", SLAC Report 266, Stanford Linear Accelerator Center, section 2.4 (particle transport), see also http://ehssun.lbl.gov/egs/egs.html

Pozdnyakov, L. A., Sobol, I. M. & Sunyaev, R. A. 1983, Ap.& Space Sci. Reviews, 2, 189

Stern, B., et al. 1995, MNRAS, 272, 291

Woodcock et al. 1965, "Techniques used in the GEM code for Monte Carlo neutronics calculations in reactors and other systems of complex geometry", Proc. of the conference on the application of computing methods to reactor problems, ANL-7050, Argone National Lab.

Part III

Astrophysical

Chapter 4

Comptonized Spectra from AGN

The standard two-phase disk–corona model for the high-energy spectra of active galactic nuclei (AGN) is modified to include an additional component — an outflow or wind which is assumed to provide an additional source of disk cooling. Earlier slab disk–corona models predict a spectral index which is consistent with observations only if all the accretion power is dissipated in the corona. For the models investigated here, energy spectral indices that are consistent with observations can be obtained with less accretion power being dissipated in the corona, as a result of an outflow / wind. However, the luminosity ratio of the hard component to the soft component is required to be greater than one, which is not consistent with observations.

4.1 Accretion disk coronae

The accretion disks that exist in AGN (and also in X-ray binaries) are often modeled using the standard geometrically thin, optically thick formalism of Shakura & Sunyaev (1973). Such a description, however, cannot account for the observed emission at high energies; the inflowing material cannot radiate at energies higher than the local blackbody temperature, $T_{bb} = \left(\frac{L}{4\pi r^2 \sigma}\right)^{1/4} \simeq 2 \times 10^5 \ (L/L_{Edd})^{1/4} (r/10 r_g)^{-1/2} (M/10^7 M_\odot)^{-1/4}\mathrm{K}$. Two possible explanations for the observed high energy emission are: a hot accretion disk solution, first suggested by Shapiro et al. (1976), and an accretion disk corona, first proposed by Liang & Price (1977) and Bisnovatyi-Kogan & Blinnikov (1977). The hot disk solution has been found to be thermally unstable, however.

The accretion disk corona is an optically thin layer of plasma above and below the innermost regions of the accretion disk, where the bulk of the accretion power is ulti-

mately dissipated. Although the heating mechanism for accretion disk coronae is not yet known, the current consensus is that magnetic processes are involved (see e.g. Miller & Stone 2000). The primary cooling mechanism is inverse Compton scattering off soft photons emitted by the disk.

The observed spectral energy distributions of most AGN (Seyfert galaxies and radio-quiet quasars) reveal a power law at X-ray energies with a spectral index that varies remarkably little from a value close to unity. Observed spectral indices of Seyferts fall in the range $\alpha \sim 0.80 - 1.10$ (Pounds et al. 1990, Nandra & Pounds 1994). This has led to the formulation of the standard two-phase disk–corona models, proposed by Haardt & Maraschi (1991, 1993) (see also Svensson & Zdziarski 1994, Haardt et al. 1994, 1997) and subsequent various modifications (e.g. Dove, Wilms & Begelman 1997 and references therein). These models can reproduce the observed X-ray spectra with spectral indices $\alpha \simeq 1$, consistent with the values deduced from observations. The other main observational result is that the ratio of the luminosity in the hard component to the luminosity in the soft component L_C / L_s is typically found to be less than one.

The key ingredients of the disk–corona models are a 'standard' optically thick (i.e. 'cool'), geometrically thin accretion disk surrounded by an optically thin (i.e. 'hot'), extended atmosphere / corona. This two-phase system interacts via a radiation field that is largely generated by thermal reprocessing effects; the X–rays and γ–rays are produced in the diffuse corona as a result of upscattering (Comptonization) of soft (optical / UV) disk photons, which are in turn produced partly by the re–emission of photoabsorbed X–rays and partly by radiating away energy directly dissipated in the disk. For a slab coronal geometry it is required that the fraction, f, of the accretion power dissipated in the corona be close to unity, so as to obtain a spectral index $\alpha \approx 1$. (e.g. Haardt, Maraschi & Ghisellini 1994). However, in its simplest form the slab corona geometry cannot account for the spectral index of all Seyferts (Petrucci et al. 2000), because the spectral index obtained cannot be made to be less than one, as is sometimes observed.

To resolve these difficulties, Haardt et al. (1994) introduced a covering factor so that some fraction of the soft photons escape from the disk without passing through the corona and being Comptonized. The parameter f can then take a smaller value because such a 'photon starved' corona cools less efficiently, so less accretion power is required for a given coronal temperature. Because such a corona is in general hotter, the amplification factor is larger, and spectral indices that are less than unity can be produced. Other proposed resolutions to this problem so far include the introduction of bulk motion of coronal material away from the disk (Beloborodov 1999) and the possibility of a highly ionised disk surface (Nayakshin, Kazanas & Kallman 2000).

What these models have in common is the idea of reducing the flux of reprocessed disk photons entering the corona. Because the corona cools via inverse Compton scattering of these photons, the cooling rate is reduced and the hotter corona produces a harder spectra. For instance, a covering factor enables reprocessed soft disk photons to escape without entering the corona. Photons that scatter in the bulk motion model are preferentially scattered away from the disk (if the bulk flow is directed away from the disk), reducing the number of photons that are reprocessed by the disk. The ionised disk model also reduces reprocessing by the disk as many photons are reflected away due to the larger albedo.

One component that has been generally overlooked in disk–corona models to date is a disk outflow. Despite the understanding that outflows may be common in these systems (for a discussion see e.g. Heyvaerts 1992), the effect of outflows on the energy balance of the system and hence their effect on the high–energy spectra are only now being investigated.

If a disk wind exists in Seyfert galaxies, it will extract energy from the accretion disk, reducing the number of soft photons that are required to dissipate the accretion power in the disk. As the disk emits fewer soft photons, coronal electrons cannot cool as efficiently by inverse Compton scattering, and so the corresponding coronae are hotter, leading to harder spectra.

The exact mechanism producing winds from accretion disks has not been definitively established, but one possibility is that the outflow is an electromagnetic / Poynting-flux dominated wind (Michel 1987). Such an outflow could be launched from a magnetised accretion disk, and the fraction of available accretion power extracted from the disk can be of order one (Lovelace, Wang & Sulkanen 1987).

Other possibilities are that a centrifugally driven wind can remove a significant amount of disk energy (Blandford & Payne 1982), or, if the accretion rate is low, a modification to the advection dominated accretion flow (ADAF) model has been proposed that includes a powerful wind that carries away mass and energy from the accreting material (Blandford & Begelman 1999). Compton heated winds are probably ruled out, however, as the Compton temperature is much less than the virial temperature (Begelman, McKee & Shields 1983).

Here, a disk–corona model is considered in which the disk and the corona are coupled in the usual manner, but where some of the energy in the disk, including some of the energy the disk has absorbed from hard illuminating photons, is dissipated in an outflow or wind. This provides an additional avenue for disk cooling (figure 4.1).

This model is then compared to a second possible disk–corona model involving out-

flows and magnetic fields (de Kool, Bicknell & Kuncic 1999). This model considers an outflowing corona in which the corona is heated predominantly by the dissipation of buoyant magnetic flux tubes emerging from the disk.

The spectral indices predicted by these 'windy' disk–corona models are determined and compared to those predicted by the standard two-phase model.

4.2 A modified two-phase model

The model developed here follows the method of Haardt & Maraschi (1991), which draws on energy balance equations for the disk and corona to parametrise the partitioning of accretion power $P_{\rm a}$ between the phases.

4.2.1 Energy Balance

Initially, some fraction f of the total accretion power is dissipated in the corona, while the remaining fraction $(1-f)P_{\rm a}$ is dissipated directly in the disk. Because the coronal geometry in particular is still uncertain, it is taken to be a simple slab coronal geometry. Geometrical factors would further complicate the analysis without providing additional insight.

The total luminosity emitted by the corona is given by $AL_{\rm s}$ where A is the amplification factor due to Comptonization of the soft input photon luminosity $L_{\rm s}$. Thus, the Compton luminosity is $L_{\rm C} = L_{\rm uC} + L_{\rm dC} = (A-1)L_{\rm s}$ where $L_{\rm uC}$ and $L_{\rm dC}$ are upward-directed and downward-directed components of $L_{\rm C}$, respectively. The downward-directed photons can produce a reflected component in the X–ray spectrum, $L_{\rm ref} = aL_{\rm dC}$, where a is the albedo, and the remaining fraction is absorbed by the disk.

Not all of the absorbed radiation need be re–emitted at soft energies and contribute to $L_{\rm s}$, if some fraction of this energy is removed via a disk wind. Because of the uncertainty in the exact physics responsible for launching disk winds, in this work the efficiency of the wind is parameterised by β, where β is the ratio of the energy extracted from the disk by the wind to the luminosity of the hard photons absorbed by the disk. This means that a fraction of the absorbed power $(1-\beta)(1-a)L_{\rm dC}$ contributes to $L_{\rm s}$. Other parameterisations are certainly possible, but are essentially equivalent mathematically.

With this choice of parameterisation, the rate of energy deposited in the wind from

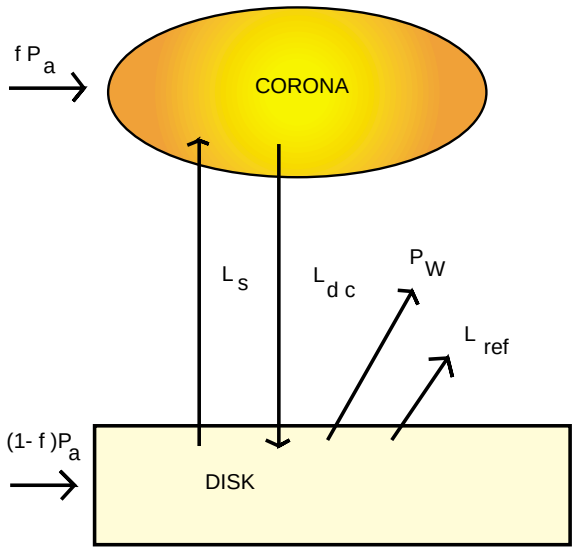

Figure 4.1: A schematic illustration of the energy balance for the modified two-phase model used in this work. If $P_W = 0$ the conventional disk–corona model is recovered (Haardt & Maraschi 1991).

the accretion disk is

$$P_{\rm w} = \beta(1-a)L_{\rm dC} = \eta(1-a)\beta L_{\rm C} = \eta(1-a)\beta(A-1)L_{\rm s}\ . \tag{4.1}$$

where $\eta \equiv L_{\rm dC}/L_{\rm C}$.
The energy balance equation for the optically thick phase, the accretion disk, is

$$L_{\rm s} = (1-f)P_{\rm a} + (1-a)L_{\rm dC} - P_{\rm w} = (1-f)P_{\rm a} + (1-\beta)(1-a)L_{\rm dC}\ , \tag{4.2}$$

while the energy balance equation for the optically thin phase, the corona, is

$$L_{\rm C} = fP_{\rm a} = (A-1)L_{\rm s}\ . \tag{4.3}$$

From Eq. 4.3 the amplification factor is

$$A \;=\; 1 + \frac{fP_{\rm a}}{L_{\rm s}}\ . \tag{4.4}$$

Solving for $L_{\rm s}$ in Eq 4.2 using $P_{\rm w}$ and A (Eq. 4.4) gives the luminosity of the soft photons from the accretion disk,

$$L_{\rm s} \;=\; [(1-f) + \eta(1-a)(1-\beta)f]P_{\rm a}\ . \tag{4.5}$$

Solving for A using Eq. 4.4 and Eq. 4.5 yields the desired amplification factor

$$A = 1 + \frac{f}{1 - f[1 - \eta(1-a)(1-\beta)]} \ , \tag{4.6}$$

which is independent of the total accretion power $P_{\rm a}$. Note that if β is set to zero (the no wind case), the original amplification factor given in Haardt & Maraschi (1991) is recovered.

The values of β considered in this Chapter run from zero to one. Note that $\beta = 1.0$ does not correspond to all of the disk energy being removed in the wind, only some fraction (Eq. 4.1) there of. A larger value for β is allowed, which would have the effect of reducing the amplification factor (Eq. 4.6).

The total outward luminosity is

$$L_{\rm out} = L_{\rm s} + L_{\rm uC} + L_{\rm ref} \ , \tag{4.7}$$

where

$$L_{\rm uC} = (1 - \eta) f P_{\rm a} \ , \tag{4.8}$$

is the luminosity of the upward-directed photons.

It should also be noted that the accretion power in the system is carried out not only by the upward-directed Comptonized photons from the hot corona but also by the wind from the accretion disk. Using Eq. 4.1 & Eq. 4.4 gives $P_W = \eta(1-a)\beta f \leq 0.51$ since β and f can at most be equal to unity, so that up to half of the accretion power can be carried away by the wind rather than the radiation. This is why $L_{\rm out}$ does not equal $P_{\rm a}$ (cf. Haardt & Maraschi 1991), as some power is dissipated in the wind from the disk. It is, however, not difficult to verify $L_{\rm out} + P_{\rm w} = P_{\rm a}$.

4.3 Spectral Index and Temperature

To determine the observational effects of a wind, it is necessary to determine the spectrum of this model. To do this, an iterative approach is used to solve for the parameters of the corona.

4.3.1 Iterative Method

For optical depth ($\tau \equiv n\sigma_T h$ with n the electron density, σ_T the Thompson cross-section and h the height of the slab corona above the disk) less than one, the Comptonized

spectrum can be approximated by a power law

$$I(\epsilon) = I(\epsilon_0) \left(\frac{\epsilon}{\epsilon_0}\right)^{-\alpha} , \tag{4.9}$$

where

$$\alpha = -\frac{\ln(\tau)}{\ln(A_1)} , \tag{4.10}$$

(Rybicki & Lightman 1979, Pozdnyakov, Sobol & Sunyaev 1983), ϵ_0 is the average energy of the soft photons, and A_1 is the amplification factor describing the average energy gain for a single scattering. In Titarchuk & Lyubarskij (1995) more accurate expressions for α, which take into account the effects due to geometry and optical depths, are given (see also Haardt & Maraschi 1993). However, for the purpose of this study, using the simple expression for α in Eq. 4.10 or the accurate expressions given elsewhere will not lead to qualitatively very different results. In terms of the corona temperature (in units of the electron rest mass energy $\Theta = kT_{\rm c}/m_{\rm e}c^2$),

$$A_1 = 16\Theta^2 + 4\Theta + 1 , \tag{4.11}$$

(e.g. Haardt, Maraschi & Ghisellini 1997). Assuming that $L_{\rm s} \simeq I(\epsilon_0)\epsilon_0$, the energy gained by the photons traversing the corona is then given by

$$A - 1 = \frac{1}{I(\epsilon_0)\epsilon_0} \int_{\epsilon_1}^{3kT_{\rm c}} I(\epsilon)\, d\epsilon \tag{4.12}$$

$$= (1-\alpha)^{-1} \left[\left(\frac{3kT_{\rm c}}{\epsilon_0}\right)^{1-\alpha} - {A_1}^{1-\alpha} \right] , \tag{4.13}$$

where $\epsilon_1 = \epsilon_0 A_1$ is the energy gain due to the first scattering of the soft photons in the corona, ϵ_0 is the average energy of the soft input photons and α is the spectral index of the resulting Comptonized spectrum.

The expression for the amplification factor A, in Eq. 4.6, is substituted into Eq. 4.13 and the resulting expression solved iteratively for the spectral index α as a function of τ and Θ for various values of f and β.

The effects of the spectral temperature of the soft black body photons on the spectral index in the energy range 2-10 keV is generally insignificant due to the large energy shift per scattering event. Therefore the mean photon energy is fixed to $\epsilon_0 = 50$ eV in this study. For simplicity, it is assumed that the scattering albedo and the downscattering parameter have constant values of $a = 0.15$ and $\eta = 0.6$ respectively. (A detail discussion on the effects due to anisotropy ($\eta \neq 0.5$) and the variations in a and η with the optical

depth can be found in Haardt & Maraschi 1993). For the $\beta = 0$ case (i.e. the conventional two-phase no wind disk–corona model) the '$\alpha - \mathrm{Log}(\tau)$' and '$\mathrm{Log}(\Theta) - \mathrm{Log}(\tau)$' relations are consistent with those in Figure 1 of Haardt & Maraschi (1991). (The exact values of a and η considered by those authors were 0.15 and 0.6 respectively, however their expression of A_1 was obtained by a fit to Monte Carlo simulations. Their results can be reproduced here if $a = 0.17$ and $\eta = 0.5$.)

Now consider spectra produced using the amplification factor given in Eq. 4.6 with f = 0.5 and for various values of β. The spectral index α and the logarithm of the coronal temperature Θ as functions of the optical depth τ are shown in Figures 4.2a and b. Figure 4.3a, and b shows the results for the cases with $\beta = 0.75$ and various values of f. Figure 4.4a, and b shows the results for the extreme cases of f = 1.0, β = 0.99, and f = 0.9999, β = 1.0. For comparison, we also show the '$\alpha - \mathrm{Log}(\tau)$' relation of the conventional two-phase disk–corona model with $f = 1$ as the solid line in Figure 4.4a.

The inclusion of a disk wind term in this modified disk–corona model removes energy from the disk that would otherwise have gone into soft photon emission. The accretion disk emits fewer soft photons, and so the corresponding corona is hotter and photons can be up-scattered to higher energies. While the Haardt & Maraschi (1991) amplification factor can never be larger than about 3.4, the amplification factors in the wind model considered here can in principle be arbitrarily large, resulting in much flatter spectra.

To investigate the dependence of the spectra on the wind parameter in a more detailed way, figure 4.5 presents the results of Monte Carlo simulations of Comptonization in a plane-parallel slab geometry with an isotropic point source of blackbody photons located on the disk midplane. The temperature of the blackbody source was set equal to that of the monoenergetic photon source used in all the semi-analytic calculations. The temperature of the coronal electrons was determined by the energy balance as described above.

For all curves, the optical depth is $\tau = 0.1$. The solid curve is the spectrum produced when the electron temperature is given by the Haardt & Maraschi amplification factor (1991), which gives a temperature of $\Theta = 0.45$ ($f = 1.0$ case). The other curves are the spectra produced when the electron temperature is given by the amplification factor presented in Section 4.2.1. For the dashed, the dot-dashed and the dot-dot-dot-dashed curves, the temperature Θ is 0.54, 0.68, 0.80. This corresponds to $f = 1.0$ and $\beta = 0.5, 0.8, 0.9$. The peak just above 100 eV is the blackbody injection spectrum.

As the wind parameter β is increased, the spectra become progressively flatter. The temperature of the electrons increases by about 200 keV between the $\beta = 0.5$ case and

the $\beta = 0.9$ case. Because of the temperature increase, spectra with slopes harder than those found by Haardt & Maraschi can be obtained self-consistently with the amplification factor presented in section 4.2.1.

4.4 Investigation of a magnetically-heated corona

The importance of magnetic fields in any realistic coronal model has been made clear by numerical MHD simulation (Balbus & Hawley 1998, Miller & Stone 2000). Recently Kuncic & Bicknell (2001) have analytically investigated a magnetised turbulent accretion disk coupled to a corona by buoyant magnetic fields as well as the radiation field. They also consider the effects of an outflow from the disk.

Using the thin-disk equations, Kuncic & Bicknell (2001) investigated both the structure of a magnetised accretion disk by considering momentum transport, as well as energy balance. The energy balance equation they derive from first principles is

$$L_D \simeq \frac{GM\dot{M}_a(r_o)}{2r_o} - \int_{r_o}^{\infty} \frac{GM}{2r}\, d\dot{M}_w - \int_{r_o}^{\infty} 2\pi r\, dr \left[2v_z^+ \frac{\langle B_\phi^2 \rangle}{8\pi} - 2v_\phi \frac{\langle B_\phi^+ B_z^+ \rangle}{4\pi} + 2\frac{\langle v_z B_\phi \rangle^+}{8\pi} \right] + \xi L_c + L_Q \ , \qquad (4.14)$$

where $\dot{M}_a(r_o)$ is the rate material passes through the inner edge of the disk at r_o, $\dot{M}_w$ is the rate at which material is being removed in the vertical direction from the disk by the wind, r is the radius in the disk, ξ is the fraction of coronal luminosity absorbed by the disk, v is the velocity of disk material and B is the magnetic field where cylindrical coordinates have been used, M is the mass of the central object and G is the gravitational constant. A '+' superscript denotes a quantity evaluated at the disk surface. Angled brackets denote the statistical mean of a quantity. The first two terms are the rates at which gravitational potential energy is extracted by inflow (accretion) and removed by outflow (wind). The terms in square brackets in Eq. 4.14 represent the *z* component of the Poynting flux; the first term in the square brackets is the rate at which the magnetic energy density is lost in the wind, the second term is the work done against the disk by magnetic tension of field lines bending out of the disk surface, and the third term is interpreted as the buoyant escape of magnetic flux to a corona (see Kuncic & Bicknell 2001 for further details). The last two terms are the fraction of coronal luminosity that is absorbed by the disk, and the heat flux at the disk surface due to thermal conduction, respectively.

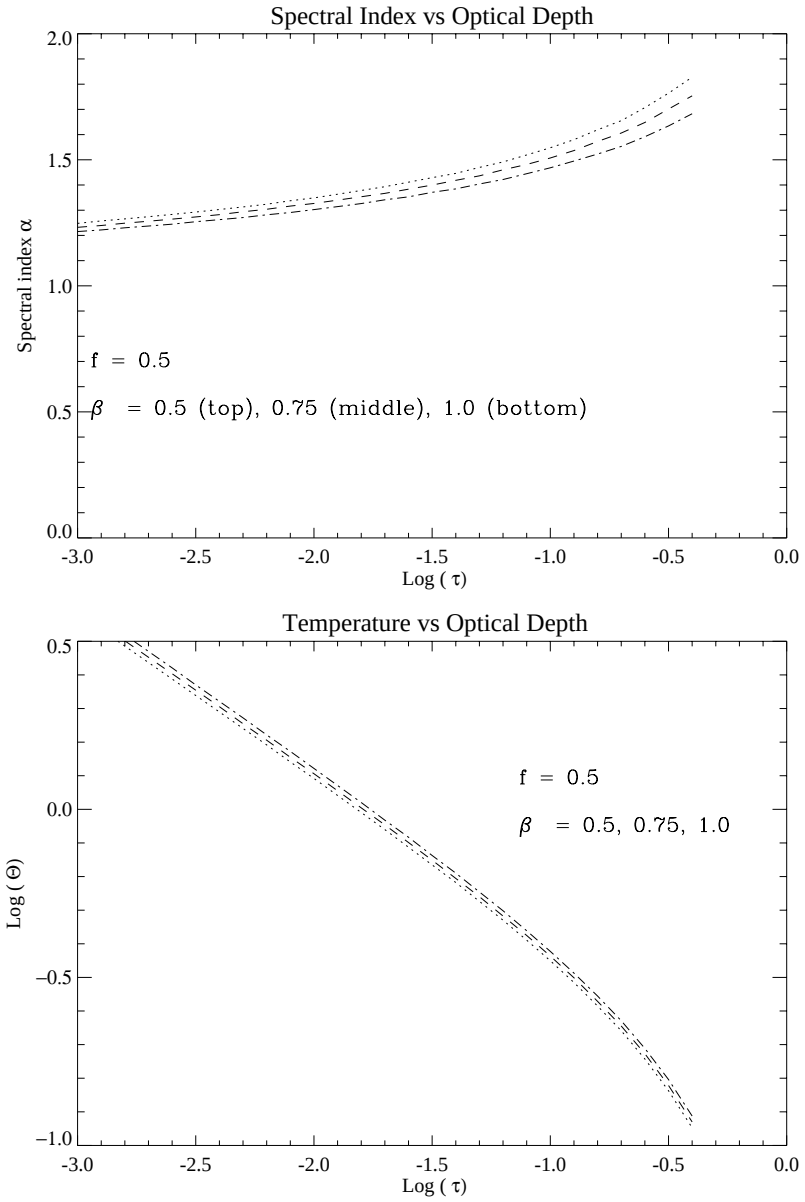

Figure 4.2: (a, top panel) Spectral index as a function of the total optical depth for f = 0.5, $a = 0.15$, $\eta = 0.6$ and various values of β, calculated using the amplification factor in Section 2.1. (b, bottom panel) Corresponding curves for the electron temperature of the corona as a function of the total optical depth.

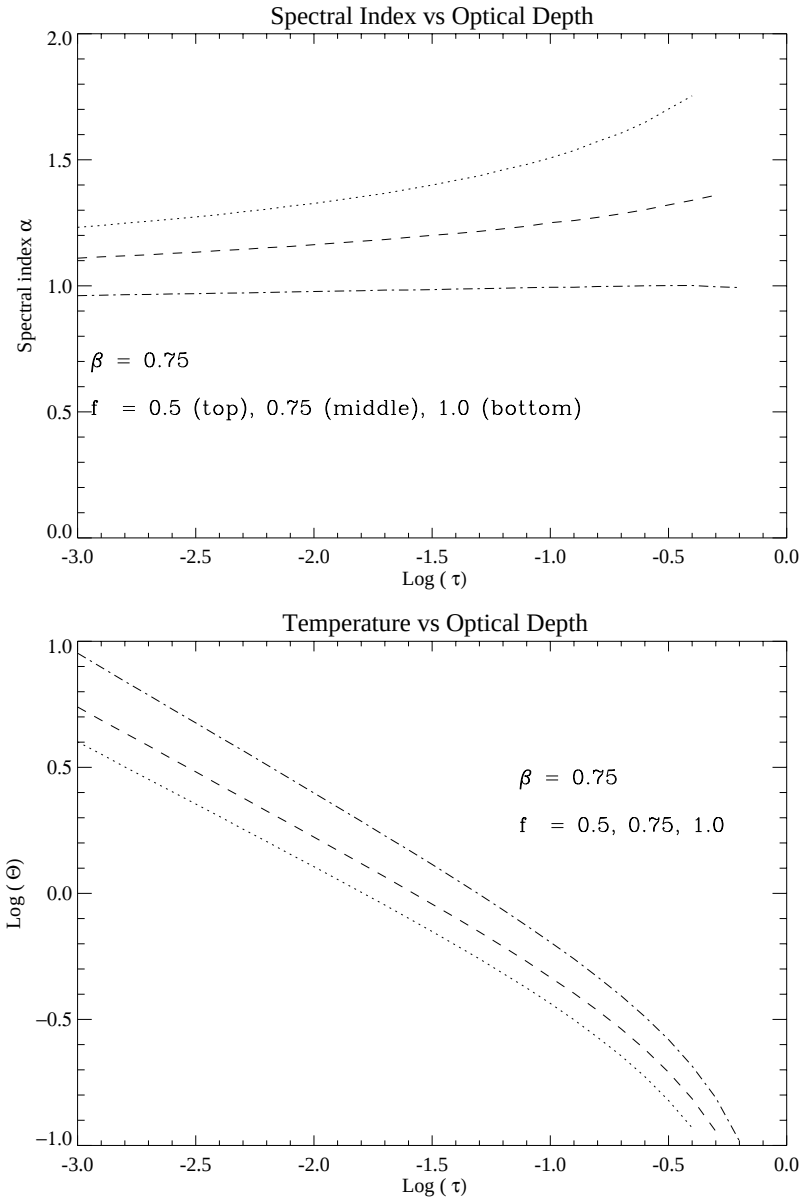

Figure 4.3: (a, top panel) Spectral index as a function of the total optical depth for $\beta = 0.75, a = 0.15, \eta = 0.6$ and various values of f. (b, bottom panel) Corresponding curves for the electron temperature of the corona as a function of the total optical depth .

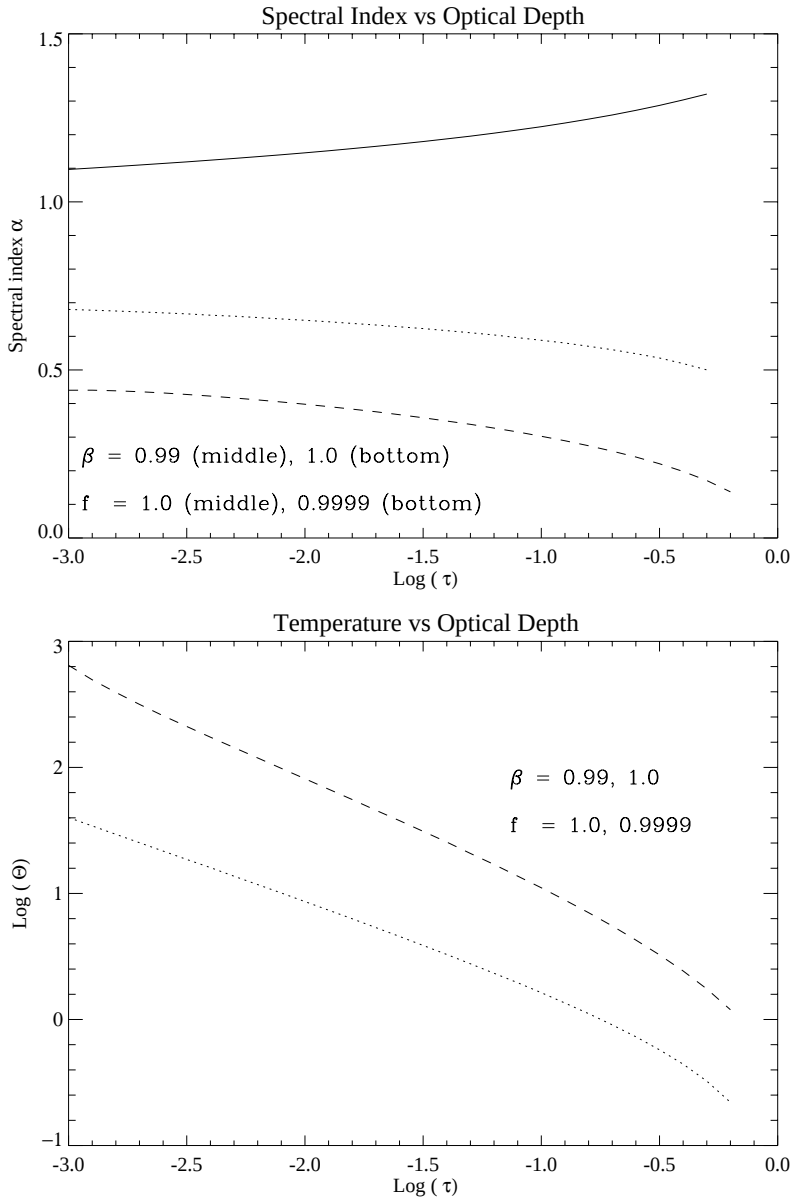

Figure 4.4: (a, top panel) Spectral index as a function of the total optical depth for $f = 1.0$, $\beta = 0.99$, $a = 0.15$, $\eta = 0.6$, and also $f = 0.9999$, $\beta = 1.0$. The conventional disk–corona model with $a = 0.17$, $\eta = 0.5$ and $f = 1$ (solid curve) is also shown for comparison. (b, bottom panel) Corresponding curves for the electron temperature of the corona as a function of the total optical depth.

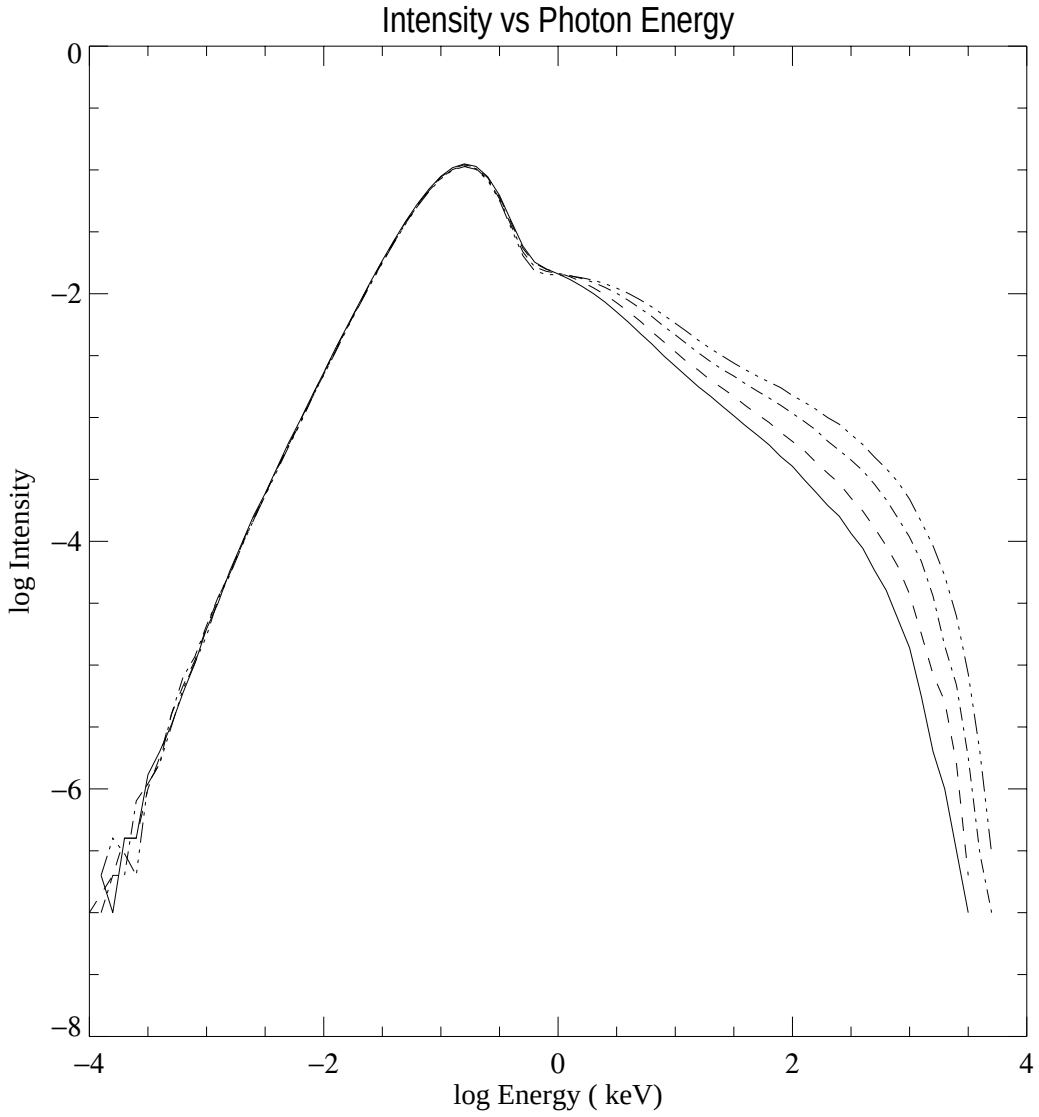

Figure 4.5: Spectra produced by Comptonization of soft photons in a slab geometry with an isotropic photon source, as calculated by a linear Monte Carlo code. All curves are for an optical depth $\tau = 0.1$. The solid curve is the standard Haardt & Maraschi model with $f = 1.0$, while the other three curves are for the modified model presented in Section 4.3, with $f = 1.0$ and $\beta = 0.5, 0.8, 0.9$ for the dashed, dot-dashed and dot-dot-dot-dashed curves respectively.

Parametrising the magnetic and conduction terms as $f_B P_G$ and $q_c f_B P_G$ respectively, the following expression for the amplification factor is obtained;

$$A - 1 = \frac{L_c}{L_D} = \frac{(1 - q_c) f_B}{1 - f_w - f_B[1 - \xi(1 - q_c) - q_c]} , \tag{4.15}$$

where f_w, f_B, and q_c represent the fraction of energy in the disk outflow, the magnetic heating of the corona, and the thermal conductivity of the disk, respectively, and ξ is the fraction of coronal luminosity absorbed by the disk. Following the same procedure as for the previous Section, this amplification factor is used to find the spectral index and coronal temperature as a function of optical depth.

Although de Kool et al. derive expressions for the parameter f_B, they do not explicitly suggest values for the other parameters. Here, to explore the parameter space of the amplification factor given by Eq. 4.15, the value of a given parameter is varied while other parameters are held constant. In figure 4.6a, the fraction of accretion power released into a wind is varied. The value of the spectral index drops to unity as f_w increases. Figure 4.6 b shows the corresponding temperature of the corona for the same values. Figure 4.7a, and b, show the results for the cases with f_w = 0.5, $q_c = 0.1$ and various values of f_B. Figure 4.8a, and b, show the results for the cases with f_w = 0.5, $f_B = 0.5$ and various values of q_c.

One sees the same qualitative behaviour as for the previously considered amplification factor, given in Eq. 4.6, in that a hotter corona produces a flatter spectrum. Again the amplification factor can be larger than the Haardt & Maraschi value.

The parameters f_w and f_B appear to be the most important factors in producing a hotter corona, while varying the coronal thermal conductivity has a relatively small effect on the spectral index.

Note here that one can write the wind parameter of Section 4.2.1 in terms of the de Kool et al. wind parameter f_w using Eq. 4.3 and Eq. 4.4

$$\beta = \frac{1}{(1 - a)\eta f} \frac{P_{\rm w}}{P_{\rm G}} = \frac{1}{(1 - a)\eta f} f_w \tag{4.16}$$

where $\frac{P_{\rm w}}{P_{\rm G}}$ is taken to be the same as f_w. This relation, when substituted into Eq. 4.6 gives the de Kool et al amplification factor if $\xi = (1 - a)\eta$ and $q_c = 0$. Thus over some of the parameter space the two models considered here are equivalent.

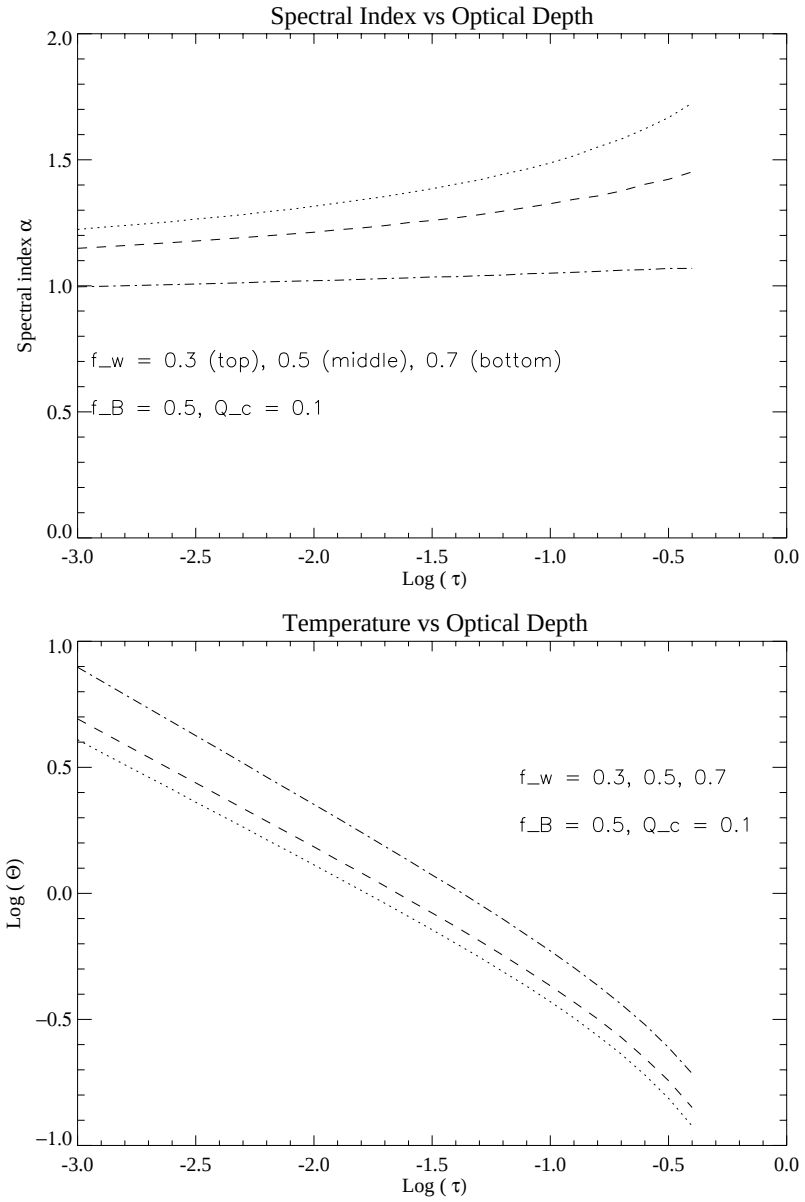

Figure 4.6: (a, top panel) Spectral index as a function of the total optical depth for $f_B = 0.5$, $q_c = 0.1$, $\xi = 0.51$ and various values of f_w, calculated using the de Kool, Bicknell & Kuncic amplification factor. (b, bottom panel) Corresponding curves for the electron temperature of the corona as a function of the total optical depth.

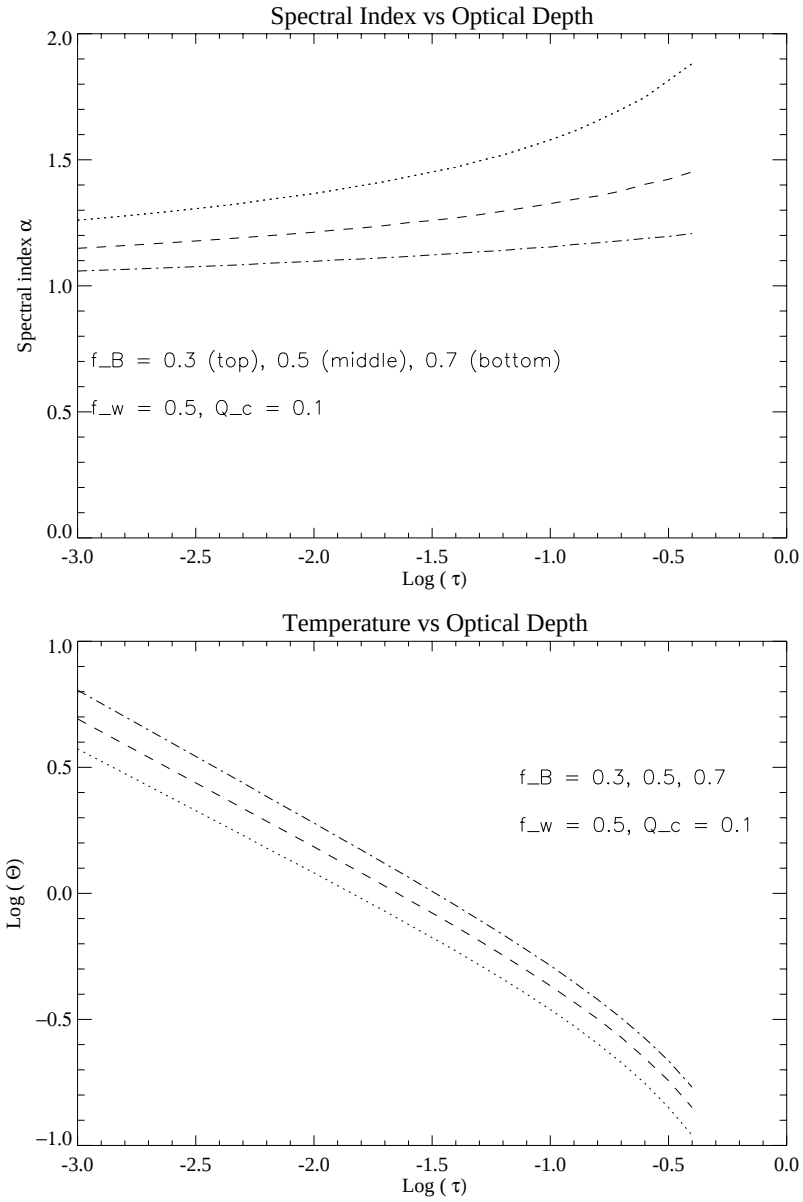

Figure 4.7: (a, top panel) Spectral index as a function of the total optical depth for $f_w = 0.5$, $q_c = 0.1$, $\xi = 0.51$ and various values of f_B. (b, bottom panel) Corresponding curves for the electron temperature of the corona as a function of the total optical depth .

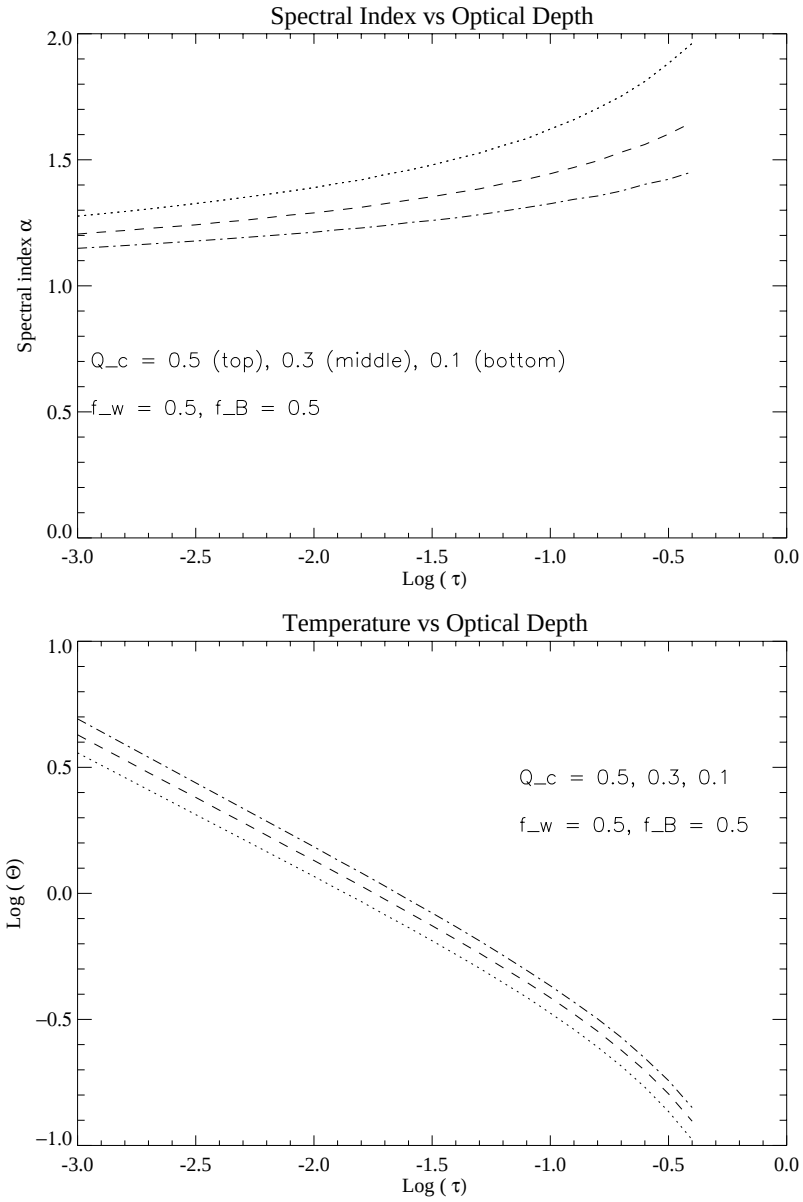

Figure 4.8: (a, top panel) Spectral index as a function of the total optical depth for $f_w = 0.5$, $f_B = 0.5$, $\xi = 0.51$ and various values of q_c. (b, bottom panel) Corresponding curves for the electron temperature of the corona as a function of the total optical depth.

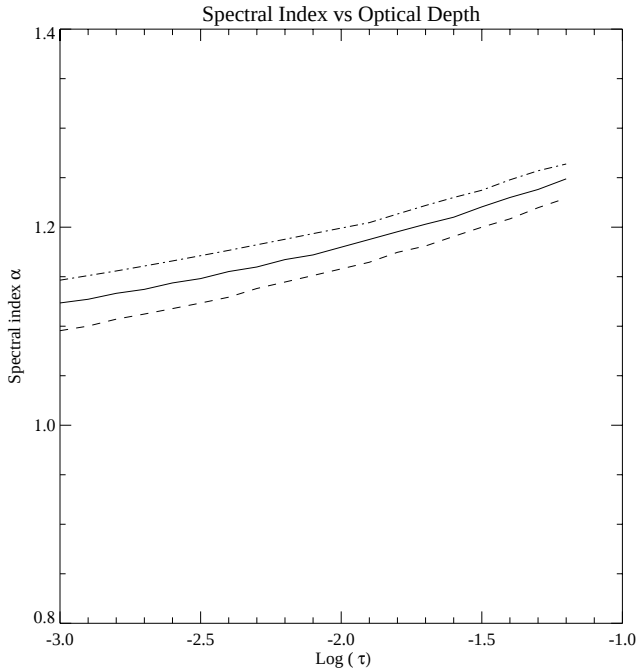

Figure 4.9: Spectral index as a function of the total optical depth for f = 1.0, $a = 0.15$, $\eta = 0.6$ and $\epsilon_0 = 50,\ 5$ and 200 eV for the solid, dashed and dot-dashed curves respectively. This demonstrates the dependence of spectral index on the temperature of the injected photons.

4.5 Dependence of spectral index

The previous results have assumed constant values for certain key parameters. Here the dependence of the resulting spectral index on variations of these parameters is considered.

Figures 4.9 and 4.10 illustrate the dependence of the spectral index on the values of the chosen constants. Figure 4.9 investigates the variation in spectral index with different temperatures for the injected photons. Figure 4.10a investigates different fractions of downward-directed photons, and figure 4.10b investigates different values of the disk albedo. There is a small variation in spectral index with injected photon temperature, and a larger dependence on both the fraction of downward-directed photons η and the albedo of the disk a. The solid curve in each of these figures is the canonical $f = 1.0$ curve with no outflow.

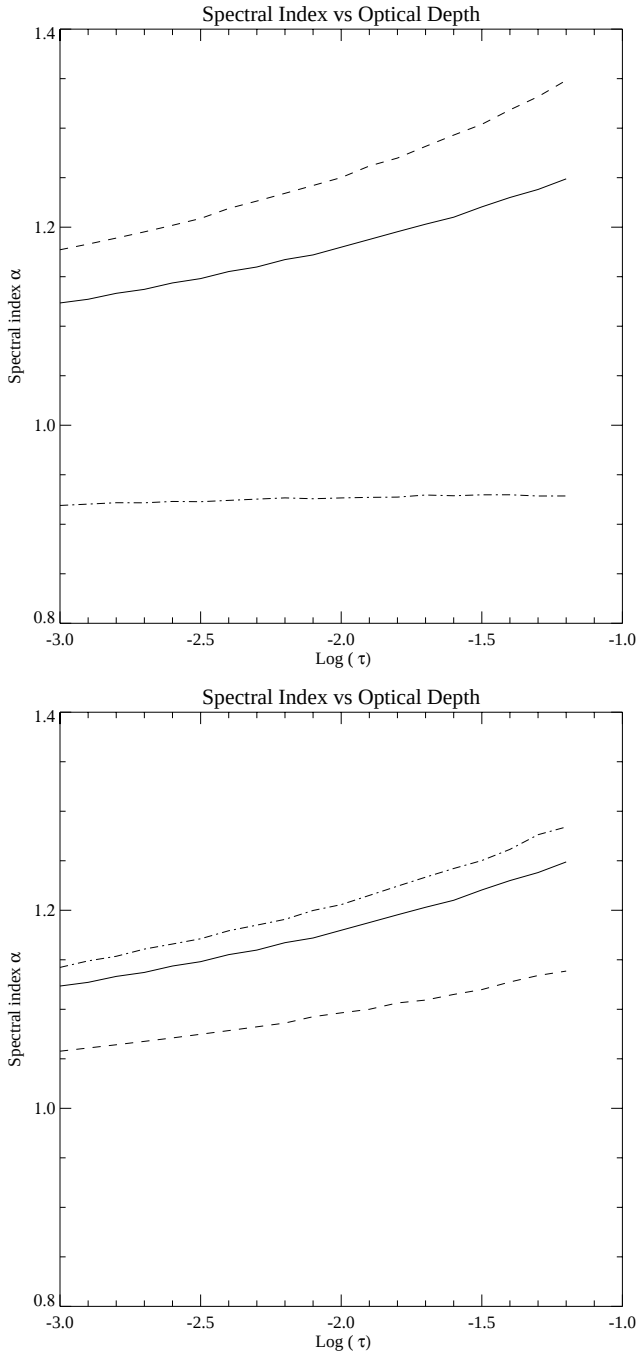

Figure 4.10: (a, top panel) Spectral index as a function of the total optical depth for f = 1.0, $a = 0.15$, $\epsilon_0 = 50$ eV and $\eta = 0.6,\ 0.1$ and 0.9 for the solid, dashed and dot-dashed curves respectively. This demonstrates the dependence of spectral index on the fraction of downward-directed photons. (b, bottom panel) Spectral index as a function of the total optical depth for f = 1.0, $\eta = 0.6$, $\epsilon_0 = 50$ eV and $a = 0.15, 0.005$ and 0.5 for the solid, dashed and dot-dashed curves respectively. This demonstrates the dependence of spectral index on the albedo of the disk.

4.6 Conclusion

As mentioned in the introduction, a disk wind extracts energy from the accretion disk, leading to a larger coronal amplification factor and harder spectra. The 'windy' disk–corona then mimics a photon starved geometry. This can be seen, for example, in figures 4.4a and b. The spectral index curves are well below 1, and the corresponding coronal temperatures are larger. This behaviour is expected for 'patchy' coronae. Therefore, the inclusion of an outflow has approximately the same effect as a covering factor, in that energy can now leave the system (in the form of a wind, rather than soft photons).

As mentioned in Section 4.1, observed spectral indices of Seyferts fall in the range $\alpha \sim 0.80 - 1.10$. The original two-phase model accounts for spectral indices of one and above, but cannot account for $\alpha < 1$. In particular, by the inclusion of a disk wind, these modified models can in principle account for AGN with spectral indices smaller than one.

It is possible to relax the $f = 1$ requirement for a slab corona to a certain extent, if the wind parameter is large. Considering the first modified disk–corona model, a spectral index curve similar to the '$\alpha - \mathrm{Log}(\tau)$' relation for $f = 1$ given in Haardt & Maraschi (1991) can be reproduced by the model with the parameters $f = 0.75$ and $\beta = 0.75$. A spectral index much less than unity can also be obtained, if appropriate values for the parameters are chosen (figure 4.4a).

As noted previously, the two models considered here are equivalent over some of the parameter space if $q_c = 0$. Using the second model (de Kool et al. 1999) a spectral index at or less than unity can also be obtained, again if the corona is wind dominated, for the same reason as discussed above. For example, in figure 4.7a, 'α' is close to unity for f_B = 0.5 if 'f_w' is 0.7. This model can therefore also account for Seyfert galaxies that have Comptonized components with $\alpha \leq 1$.

The shape of the Comptonized spectrum depends on both temperature and optical depth. The spectral index curves for the standard disk–corona model increase with increasing 'τ', while the coronal temperature is decreasing. That is, the trend of the spectral index is determined predominantly by optical depth. For the first model considered here, if the wind parameter and the heating rate are both large, the spectral index can be made to decrease with increasing 'τ' and follow the temperature in trending downward. The spectral index is now in a regime where it is being determined mainly by the temperature (figure 4.4a).

Compared to the Haardt & Maraschi model, the corona for both models can be substantially hotter. The observational constraints on the temperature of the coronal plasma

depend on the energy of the spectral cut-off, which is not well determined. However, the maximum temperature seem to be in the range of a few hundreds of keV. This would restrict these models to an optical depth of ~ 0.1 or greater as at lower optical depths electron cooling is inefficient.

It should be mentioned that to determine if the higher coronal temperatures required by 'windy' disk–coronae are reasonable requires a non-linear Monte Carlo simulation of the type performed by Stern et al. (1995). Such a simulation allows the coronal heating to balance inverse Compton cooling and determine a coronal temperature self-consistently (whereas linear Monte Carlo simulations assume a temperature as input).

An electromagnetic wind is almost impossible to directly observe (Michel 1987). If the wind is of the type associated with an ADAF or an inflow/outflow solution, observation of the wind is still difficult, although the wind could potentially be observed if the wind passes through a terminal shock (Blandford & Begelman, 1999). In this case, it is difficult to know what, if any, observational relationship might exist between shocked-wind emission and the power law index.

One possible observational effect is whether there is a correlation between the variability of the soft component and the variability of the hard component. If the wind is unstable, and some material is entrained with the wind, and the system is being observed along a line of sight that passes through the wind, then the line-of-sight electron density will be time-dependent. The amount of absorption soft photons experience will vary, while the hard photons will experience little absorption. Therefore, the soft component will be fluctuating with respect to the hard component.

The drawbacks of the models are that producing the observed value of the hard to soft components is not possible, as the amplification factor required for a flat spectrum gives an L_C/L_s ratio of greater than one. Observationally, the ratio L_C/L_s is typically less than one. This has also been a problem with previous slab corona models. Also, as this work considers the albedo of the disk to be constant, the models cannot account for the observed correlation between spectral index and the amount of disk reflection. This correlation seems to require complex ionisation structure, as investigated by Done & Nayakshin (2001), or perhaps bulk motion in the corona (Beloborodov 1999).

In summary, the spectra from disk–corona models with outflows have been investigated. There exists a regime in which the dependence of spectral index on temperature is the opposite of that usually expected; cooler coronae may produce harder spectra (figure 4.4a). Because of the formal similarity between these windy models and photon-starved models, one might speculate that this result may also hold for very photon-starved models. With both of the models considered in this work, spectral indices con-

sistent with observations can be obtained in a slab geometry without requiring all the accretion power to be dissipated directly to the corona, because an outflow has approximately the same effect on the system as a covering factor.

References

Balbus, S. A. & Hawley, J. F. 1998, “Accretion processes in astrophysical systems; some like it hot!”, eds. S. S. Holt & T. R. Kallman (AIP conference proceedings 431)

Begelman, M.C., McKee C.F. & Shields G.A. 1983, ApJ, 271, 70

Beloborodov, A.M. 1999, ApJ, 510, L123

Bisnovatyi-Kogan, G. S. & Blinnikov, S. I. 1977, A&A, 59, 111

Blandford, R.D. & Begelman, M.C. 1999, MNRAS, 303, L1

Blandford, R.D. & Payne, D.G. 1982, MNRAS, 199, 883

Done, C. & Nayakshin, S. 2001, ApJ, 546, 419

Dove, J.B., Wilms, J. & Begelman, M.C. 1997, ApJ, 487, 747

Haardt, F. & Maraschi, L. 1991, ApJ, 380, L51

Haardt, F. & Maraschi, L. 1993, ApJ, 413, 507

Haardt, F., Maraschi, L. & Ghisellini, G. 1994, ApJ, 432, L95

Haardt, F., Maraschi, L. & Ghisellini, G. 1997, ApJ, 476, 620

Heyvaerts, J. F. 1992, “Physics of AGN”, eds. W. J. Duschi & S. J. Wagner (Heidelberg: Springer-Verlag)

de Kool, M., Bicknell, G. V. & Kuncic, Z. 1999, PASA, 16, 3, 225

Kuncic, Z. & Bicknell, G. V. 2001, ApJ, submitted.

Liang, E. P. T. & Price, R. H. 1977, ApJ, 218, 247

Lovelace, R. V. E., Wang, J. C. L. & Sulkanen, M. E. 1987, ApJ, 315, 504

Michel, F. C. 1987, ApJ, 321, 714

Miller, K. A. & Stone, J. M. 2000, ApJ, 354, 398

Nandra, K. & Pounds, K. A. 1994, MNRAS, 268, 405

Nayakshin, S., Kazanas, D. & Kallman, T.R. 2000, ApJ, 537, 833

Petrucci, P. O., Haardt, F., Maraschi, L., Grandi, P., Matt, G., Nicastro, F., Piro, L., Perola, G. C. & De Rosa, A. 2000, in press (astro-ph/0004118)

Pounds, K. A., Nandra, K., Stewart, G. C., George, I. M. & Fabian, A. C. 1990, Nature, 344, 132

Pozdnyakov, L. A., Sobol, I. M. & Sunyaev, R. A. 1983, Ap. & Space Sci. Reviews, 2, 189

Rybicki, G. B. & Lightman, A. P. 1979, “Radiative Processes in Astrophysics”, (New York: Wiley)

Shakura, N. I. & Sunyaev, R. A. 1973, A& A, 24, 337

Shapiro, S. L., Lightman, A. P. & Eardley, D. M. 1976, ApJ, 204, 178

Stern, B. E., Poutanen, J., Svensson, R., Sikora, M., & Begelman, M. C. 1995, ApJ, 449, L13

Svensson, R. & Zdziarski, A. A. 1994, ApJ, 436, 599

Titarchuk, L. & Lyubarskij, Y., 1995, ApJ, 450, 876 (astro-ph/0006151)

Chapter 5

Time lags due to Comptonization in multi-temperature plasmas surrounding compact objects

In this Chapter, the two-zone model proposed by Moskalenko, Collmar and Schönfelder (1998) for plasma surrounding galactic black hole candidates is investigated, by determining the spectral and temporal behaviour. In this case, the scattering region consists of a hot shell surrounding a cooler spherical core.

To numerically calculate the spectra predicted by this model in the keV and MeV energy ranges, a linear Monte Carlo code has been developed, as described in Chapter 2. It is found that the time lag information may in principle be able to determine whether this particular geometry is a realistic model for the material surrounding galactic black hole candidates.

5.1 Compton scattering in galactic black hole candidates

Galactic black hole candidates (BHCs) are known to be sources of high energy photons. This emission is thought to be powered by the gravitational potential energy release resulting from material accreting onto a compact object, by either wind accretion or Roche-lobe overflow from a companion. The spectra of galactic BHCs are often described as being in either a "high" state, or a "low" state depending on the spectral characteristics in the $2-10$ keV band. The high state spectrum consists of a blackbody component of temperature ~ 1 keV and a power law of photon spectral index $\sim 2.2{-}2.7$,

while the low state spectrum consists of a single power law of photon spectral index in the range $1.4 - 1.9$ (Esin et al. 1998).

The power law component is attributed to blackbody photons being up-scattered by electrons (that is, the photons gain energy from the electrons via the inverse Compton process) as they traverse a corona of hot plasma with a Maxwellian electron temperature $\sim 10 - 100$ keV (Bisnovatyi-Kogan & Blinnikov 1976, Sunyaev & Titarchuk 1980). If the Comptonization is saturated, where the photons are in thermal equilibrium with the electrons, then the cut-off in the spectrum occurs at $\sim 3kT_e$ where kT_e is the thermal temperature of the coronal electrons. However, the COMPTEL instrument on the Compton gamma-ray Observatory satellite has detected significant gamma-ray emission up to energies of several MeV (Johnson et al. 1993), which cannot be explained by the canonical Comptonization model because the energy of the gamma-rays exceeds reasonable estimates of the coronal temperature.

While inverse Compton (IC) scattering is understood to be one of the important processes for producing high energy photons from galactic BHCs (as well as accreting neutron stars and active galactic nuclei), the physical geometry of the coronal plasma responsible for scattering the photons is not well constrained by current observations. This is partly due to the nature of IC scattering: in general, it depends only on the temperature and the optical depth of the plasma, rather than depending on the physical dimensions directly.

The two geometries that are commonly assumed for spectral calculations are the plane-parallel "slab" corona above a standard thin accretion disk, and a spherical or quasi-spherical corona surrounding the innermost part of an accretion disk. Based on the results of non-linear Monte Carlo spectral simulations (Dove et al. 1997) the spherical corona plus disk geometry best accounts for the low (hard) state spectrum of galactic black hole candidates. For example, Cyg X-1 spends most of its time in the low state.

The problem then remains of how to produce gamma-ray photons. Possibilities that have been considered are a non-thermal tail to the electron Maxwellian distribution, which would be generated by some magneto-hydrodynamic (MHD) process, or a compact electron-positron pair dominated plasma. It has been pointed out that the latter possibility is unlikely (Moskalenko, Collmar & Schönfelder 1998; hereafter MCS), as the luminosity of the gamma-rays, although small, still exceeds the Eddington limit for a pair plasma.

MCS have suggested that a two-zone corona model can explain both the X-ray and gamma-ray emission of BHCs such as Cyg X-1 (see figure 5.1). In this model, the plasma geometry consists of two concentric spheres of plasma, each with a different tempera-

ture and optical depth. The compact spherical inner corona of Thompson optical depth of approximately $\tau \simeq 1.4 - 2.4$ is responsible for the X-ray power law component, while a tenuous extended spherical outer corona of $\tau \simeq 0.05$ consists of relativistic electrons that are responsible for the hard gamma-ray tail.

The acceleration mechanism for the outer corona electrons is not given in MCS but could be, for instance, stochastic acceleration (Li, Kusunose & Liang 1996). The outer coronal density is low, so two-body cooling processes are inefficient and hence the temperature is high ($\simeq 400$ keV). The estimated cooling time of these electrons due to IC scattering is a few seconds, so the outer coronal electrons are effectively confined to a region a few light seconds across (at most).

It has also been emphasised (Kazanas, Hua & Titarchuk 1997) that any realistic model for a corona in galactic BHCs must also account for their temporal behaviour, such as the hard X-ray time lags, as well as the spectral fit. These time lags are produced as photons diffuse through the corona. The photons that scatter numerous times are delayed with respect to those photons that escape after undergoing few scatterings. Photons that scatter many times on average gain more energy than the other photons and so the high energy photons are delayed (take longer to escape from the plasma cloud) when compared to lower energy photons.

As recent investigations (Kazanas, Hua & Titarchuk 1997, Böttcher & Liang 1998) have shown, this time delay or lag between high and low energy photons is sensitive to the exact geometry of the up-scattering plasma, including density gradients, and so provides us with a tool that can in principle determine the geometry of the coronal plasma in galactic BHC systems.

Here, a linear Monte Carlo code (c.f. Chapter 2) is used to investigate whether the two-zone model suggested by MCS can explain both the X-ray and gamma-ray emission of BHCs, by obtaining the spectrum produced by such a model for the "low" state where IC is the dominant process. The photon time lags between the energy bands $2 - 10$ keV and $0.01 - 10$ MeV are also calculated. The time lags for this model have not previously been considered.

5.2 Description of the numerical approach: galactic black hole candidates

The linear Monte Carlo code for this study is based on the Monte Carlo algorithms presented in Pozdnyakov, Sobol & Sunyaev (1983), and discussed in Chapter 2. The code

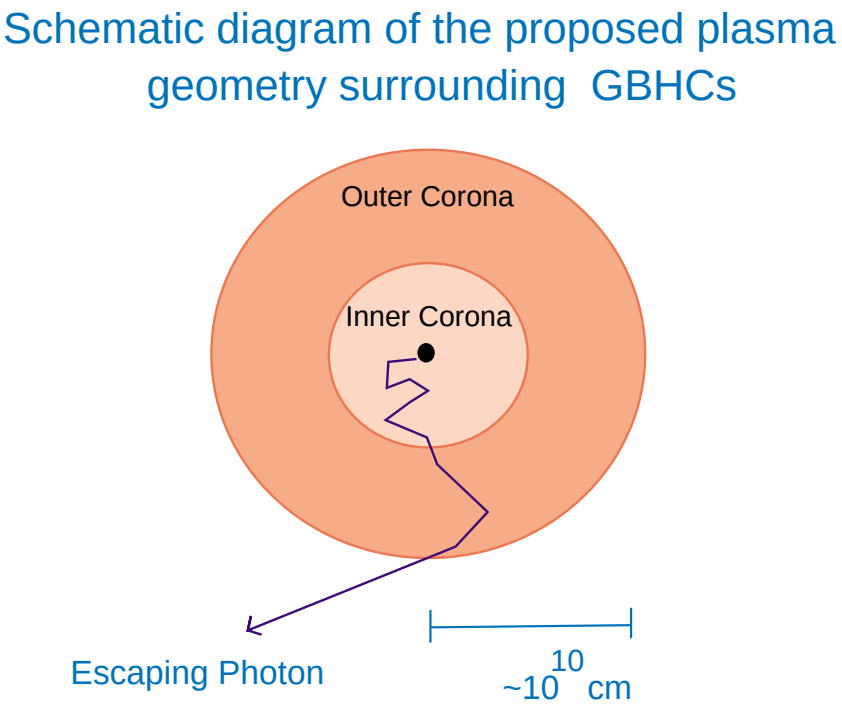

Figure 5.1: Schematic diagram of the plasma geometry surrounding galactic BHCs as considered in this paper. We consider a model in which an inner spherical corona of plasma is surrounded by an outer spherical corona of hotter, tenuous plasma. Photons emitted in the central regions (taken to be a point source) gain energy from the electrons in these coronae by inverse Compton scattering. The inner optically thick corona produces the canonical X-ray power law, while the outer corona scatters some of the escaping photons up to gamma-ray energies. The time lags between different energy bands (due to different photon escape times from the cloud) can then be found by summing over the pathlength traveled by the escaping photons.

simulates inverse Compton scattering of photons off relativistic Maxwellian electrons in a plasma of given electron temperature and optical depth. The evaluation of the mean-free-path integral (see Pozdnyakov, Sobol' & Sunyaev 1983) assumes that the plasma is homogeneous, that is, the electron temperature and the electron density are constant. The geometry of the coronal plasma is assumed to be spherically symmetric, with the source of photons at the centre of a plasma cloud. To investigate the MCS model, the plasma is divided into a shell and a spherical core. The plasma in both of these regions is homogeneous, but the two regions have different temperatures and optical depths (figure 5.1). The cloud is illuminated by a central source of blackbody photons with injection taken to be a delta function in time. In the simulations the outermost radius of the cloud is fixed to be 1.0 light second across.

The photons are injected at the centre after being assigned an energy drawn from a blackbody distribution as well as some initial direction of propagation. The injection is isotropic. Knowing the mean-free-path, the distance to the first scattering point is obtained using Eq. 2.17. All three components of the position vector of the photon are stored, as are all three components of the direction of propagation vector. After the photon is moved to the location of the scattering event (Eq. 2.19), but before the scattering event itself is modeled, the distance of the photon from the origin at the centre of the sphere is determined. This distance is compared to the radius of the inner corona, and if it is larger the photon must have crossed the boundary between the inner and the outer corona (that is, from the core to the shell). When a photon crosses this boundary, it is brought back along its path to the boundary, and (without changing its direction of propagation) a new mean free path is calculated based on the temperature and optical depth of the outer corona. A new distance to a scattering point is drawn using this new mean-free-path and the photon enters the outer corona. Because the optical depth of the outer corona is low, the mean-free-path of the photons is very large. Therefore, most photons in the simulation propagate through the shell and escape without scattering. Escape is determined by again comparing the distance of the photon from the origin to the outer radius of the shell. If the photon does scatter after entering the outer corona, a routine will determine if the photon is heading back towards the inner cloud and will re-enter the core. If it does, the distance from the photon's present location to the boundary is determined by solving a simple quadratic equation. The photons that subsequently re-enter the inner corona are again placed on the boundary, and the optical depth and temperature are reset to their values in the inner cloud. The original mean-free-path is used to draw a new distance to a scattering point, and the simulation proceeds. A photon that escapes from the plasma cloud is binned in energy, and a

new photon injected. In this way, after many photon trajectories have been followed a spectrum is obtained.

The pathlength travelled by each photon is tracked and summed to give the total distance traveled (in units normalized to the outer cloud radius). This is converted into an escape time from the cloud which is binned to give the light curves, that is, the intensity in various bands as a function of time. These light curves are therefore Green's functions in the sense that they represent the response of the system to a delta-function source term.

The Fourier time lags are then produced from the light curves (see Section 5.4) using the Fast Fourier Transform (FFT) routines in IDL. (Results were checked with those obtained numerically by Kazanas, Hua & Titarchuk (1997).)

5.3 Results: spectra

Figure 5.2 shows the single-temperature (isothermal) coronal Comptonized spectrum produced by a spherical homogeneous cloud of plasma of optical depth $\tau = 2.39$ and electron temperature of $kT_e = 76.7$ keV (dotted line). Figure 5.2 also shows the spectrum produced by assuming the MCS model (solid line). The inner cloud parameters are the same as in the single cloud case, and the outer cloud is of effective optical depth $\tau = 0.06$ and electron temperature $kT_e = 396$ keV. These temperatures and optical depths are the best fit values (as determined by MCS) to the spectra obtained by *CGRO* BATSE-COMPTEL observations of Cyg X-1 taken when it was in the low state. Also shown is the injected source spectrum which is assumed to be a blackbody distribution of temperature 130 eV. The ratio of radius of the inner cloud to the outer cloud radius is a free parameter, but the overall energy spectrum is insensitive to this. Here it is fixed to be 0.1.

In both cases, photons gain energy by Comptonization as they diffuse through the cloud, producing a power law spectrum. It can be seen from figure 5.2 that the single-temperature corona spectrum has a cutoff at below 1.0 MeV, while the multi-temperature model produces substantial numbers of photons with energies in the MeV range. This high energy excess is due to the photons that are scattered up to gamma-ray energies in the high temperature outer cloud.

Note that the X-ray power law part of the spectrum has the same slope between $2 - 100$ keV for both the single and double corona models. This is required as the canonical single corona model accounts well for the X-ray part of the spectrum. But while

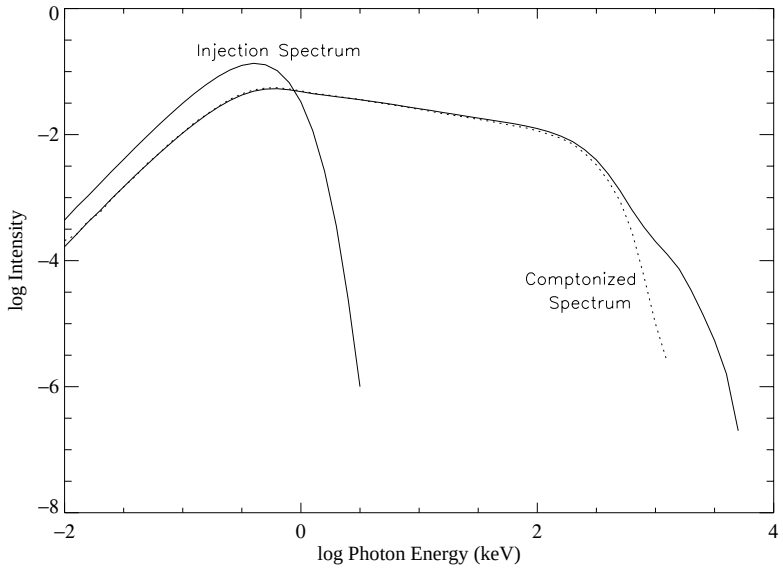

Figure 5.2: Typical spectrum produced by the two-zone model, as well as the injection spectrum and the single-temperature (isothermal) corona spectrum (dotted line, for comparison). The injected spectrum is a blackbody distribution. Photons gain energy by inverse Compton scattering as they diffuse through the cloud, forming a power law. The single-temperature corona spectrum has a cutoff below 1.0 MeV, while the multi-temperature model extends upwards into the MeV range. This high energy excess is due to the photons that are scattered up to gamma-ray energies in the high temperature outer cloud. Note that the X-ray power law part of the spectrum has the same slope for both the single and double corona models. This is required as the canonical single corona model accounts well for the X-ray part of the spectrum.

the canonical X-ray power law is still produced, there is now at high energies an excess of photons above the cutoff energy for a single temperature model. The optical depth of the outer cloud is low enough that the shape of the Comptonized spectrum at low energies is not distorted, however it does act to scatter some photons up to higher energies than they could have reached propagating through a cooler isothermal inner cloud. Therefore, this geometry can potentially explain the production of gamma-rays without contradicting inverse Compton models for spectral fits at X-ray energies.

5.4 Results: time lags

When IC scattering is the process responsible for producing high energy photons, there will be a 'hard' time lag between the photons at high and low energies. To see this, consider the rate of energy gain by soft photons in a plasma of constant density. The energy gain (initially) increases exponentially with time (see Eq. 1.46), so if one imagines a burst of photons within a corona, the photons that escape promptly are of low energy. They have not had time to be scattered up to high energies. At progressively later times, the photons observed escaping will have progressively higher energies, simply because they will have undergone more scattering events on average. Consider two narrow energy bands, E_1 and E_2. If photons are injected at time zero with energy E_0 then photons will be in energy band E_1 at time t_1, and some time after that will be in energy band E_2 at time t_2. Because the energy gain is exponential, one has the equations $E_1 = E_0 \exp(4yt_1)$ and $E_2 = E_0 \exp(4yt_2)$. A simple estimate for the time lag is then the difference between the two times $t_2 - t_1 = \frac{1}{4y}(\ln(E_2/E_0) - \ln(E_1/E_0))$, or $\frac{1}{4y}\ln(E_2/E_1)$.

The photon time lags between two different energy bands essentially represent the difference in photon pathlength (or escape time) between bands; photons in the higher energy bands tend to have undergone more scattering events, and therefore have traveled further in order to escape the corona. In fixing the two energy bands, one is effectively choosing an average number of scattering events.

Time lags can be studied by means of Fourier transforms, resulting in a plot of time lag verses Fourier frequency. Time lags in the X-ray are indeed observed from galactic BHCs, however interpretation of the situation is not straightforward, because the form of the lags is not consistent with a simple homogeneous corona model. The time lags created by Comptonization in a homogeneous and isothermal corona are predicted to be constant with Fourier frequency f, whereas the observed lags are typically close to f^{-1}.

If a spherical corona has a r^{-1} radial density profile, and is illuminated from the centre, it has been shown (Kazanas, Hua, & Titarchuk 1997) that time lags of a form similar to those observed can be obtained. This is because photons scattering at a range of radii introduce a range of timescales for escape from the corona. However, Nowak et al. (1999) has considered a similar geometry, except that the corona is illuminated from the outside by soft photons from a surrounding accretion disk. They have found that the resulting time lags are constant with Fourier frequency, similar to the homogeneous case. Clearly how the illumination of the corona occurs can have a profound effect on the form of the resulting time lags.

If the lags are indeed produced by the scattering of photons through the corona, one would expect the time lag to be proportional to the number of scattering events multiplied by the average time between scattering events. The number of scattering events in an optically thin plasma is of the order of the optical depth τ, and the average time between scattering events is the radius of the corona divided by τ and the speed of light, $R_c/(\tau c)$, which gives a number of $\leq 10^{-3}\mathrm{sec}$. The magnitude of the observed time lags at low frequencies on the other hand can be up to 0.1 s. This is accounted for in the Kazanas, Hua, & Titarchuk model by allowing the outer radius of the corona to be of the order of a light-second, even though it is unclear how the corona can be heated to high temperatures at large distances from the central regions.

Another model that attempts to account for spectral and timing data is due to Poutanen & Fabian (1999). In their model the corona consists of a number of flares that move away from the disk surface as the flare occurs. The motion away from the disk causes the spectrum to become harder as time progresses, causing lags between the soft and hard photons. The magnitude of the lag is of the same order of the time-scale for the life of the flare.

There exists another statistic for variability called coherence (see Vaughan & Nowak 1997). X-ray lags are observed to have a coherence of one, meaning that they are well described by a linear transfer function between the light curves in each band. However it is not clear that multiple flares on the surface of an accretion disk preserve coherence. If the response of the scattering medium is non-linear the coherence is no longer one. The coherence of static Compton coronae is equal to one, however any fluctuation in the parameters of the corona (as might be required to account for the observed root-mean-squared variability) destroys coherence.

The third model attempting to account for time lags postulates the propagation of waves within the accretion disk (Misra 2000). Propagation models, besides requiring very slow propagation speeds, have been criticised by Maccarone, Coppi & Poutanen (2000) as not being consistent with the observed cross-correlation function between energy bands in the soft X-rays. The r^{-1} corona model of Kazanas, Hua & Titarchuk also seems unable to account for the behaviour of the cross-correlation function.

The form of the time lags with Fourier frequency seems very similar in both the hard and soft states, especially in the case of Cyg X-1 (Pottschmidt et al 2000). Models that depend on geometry for producing time lags have difficulty accounting for why this should be so, since state transitions are thought to (possibly) be due to the size of the corona changing with respect to the disk. The lags from neutron star systems are also similar in form to those from systems thought to contain black holes (Poutanen 2000).

To date, there is no theoretical model that can account for all of the spectral and timing properties of accreting compact objects.

The time lags between two energy bands can be found by Fourier transforming the light curves in the high and low energy bands (van der Klis et al. 1987, Miyamoto et al. 1988). If the number of counts (photons) in time bin k is $c_k^{(1)}$ for one light curve, and $c_k^{(2)}$ for the light curve in the other energy band, the discrete Fourier transform of each light curve gives two quantities,

$$FT(c_k^{(1)}) \equiv a_j^{(1)} \quad \text{and} \quad FT(c_k^{(2)}) \equiv a_j^{(2)} \ . \tag{5.1}$$

Here the subscript j is related to the Fourier frequency.

The discrete Fourier transforms of the light curves a_j^1 and a_j^2 are then used to form a quantity called the complex cross power spectrum (CPS). This is done by multiplying the complex Fourier amplitudes from the low-energy band with the complex-conjugate of the complex Fourier amplitudes from the high-energy band,

$$\mathrm{CPS}_j \equiv \left(a_j^{(2)}\right)^* a_j^{(1)} \ . \tag{5.2}$$

(Here the star denotes complex conjugate of the complex number $a_j^{(2)}$). The CPS is complex, and so can be thought of as a vector in the real and imaginary plane. The angle between this vector and the real axis will be the phase lag between the two energy bands. This is performed by taking the imaginary part of the complex cross power spectrum CPS_j and then dividing by its real part. Finally, the arctangent of the result is taken to find the phase lag between bands as a function of Fourier frequency,

$$\phi = \arctan\left[\frac{\mathrm{Im}(\mathrm{CPS}_j)}{\mathrm{Re}(\mathrm{CPS}_j)}\right] \ . \tag{5.3}$$

Dividing the phase lag ϕ by $2\pi f$ (where f is the Fourier frequency) then gives the hard time lag curve as a function of Fourier frequency.

This technique has been used to investigate the time variability of galactic BHCs (for example, van der Hooft et al. 1999). As discussed above, Kazanas, Hua & Titarchuk (1997) have used this method to investigate the effect of density gradients in the Comptonizing plasma, and Böttcher and Liang (1998, 1999) have attempted to determine the location of the photon source with respect to the plasma. These authors found that the time lag curve is sensitive to variations in electron density.

Here, this method is used to determine the effect a density discontinuity of the type suggested by MCS has on the time lag curve. The radius of the inner cloud is assumed to be a free parameter, while the outer radius is fixed at one light second. Changing

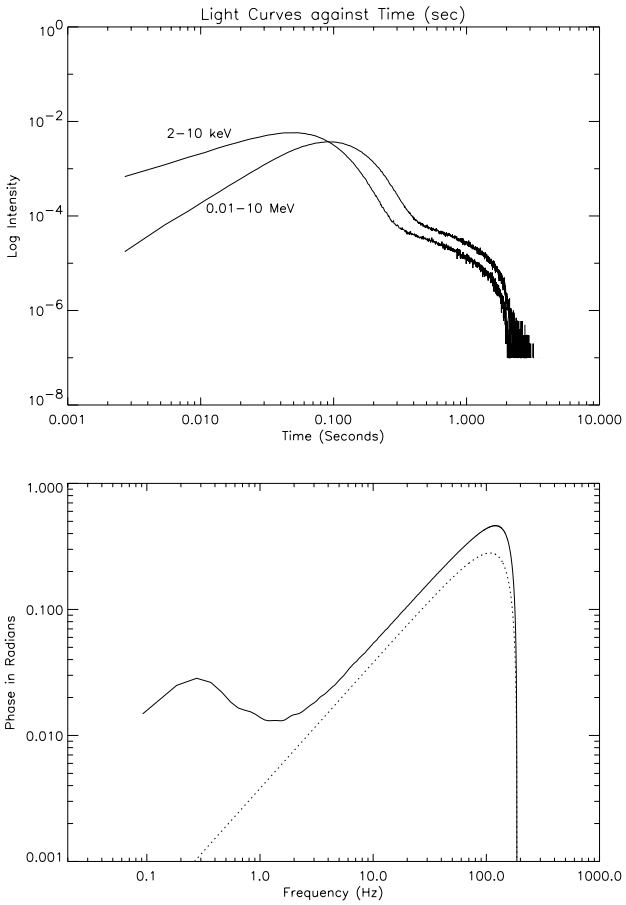

Figure 5.3: (a, top panel) Intensity in the two X-ray bands against photon escape time. In this graph the inner cloud radius is chosen to be 0.03 light seconds, and it is assumed that the physical radius of the outer cloud is 1.0 light second. The light curves are produced by Comptonization of a soft photon flare (delta function) at time zero. The cloud parameters are the best fit parameters (taken from MCS) for BATSE-COMPTEL data taken when Cyg X-1 was in the low state. They are, inner cloud: $kT_e = 76.7$ keV , optical depth $\tau = 2.39$, outer cloud: $kT_e = 396$ keV, optical depth $\tau = 0.06$. (b, bottom panel) Comparison of the phase lag for two models: the solid curve is the MCS model where the ratio of the inner and outer radii is 0.001, while the dotted curve is for a homogeneous sphere. In both cases the outer radius is fixed at one light second. The difference between the two curves at low frequencies is due to the existence of the outer shell of plasma.

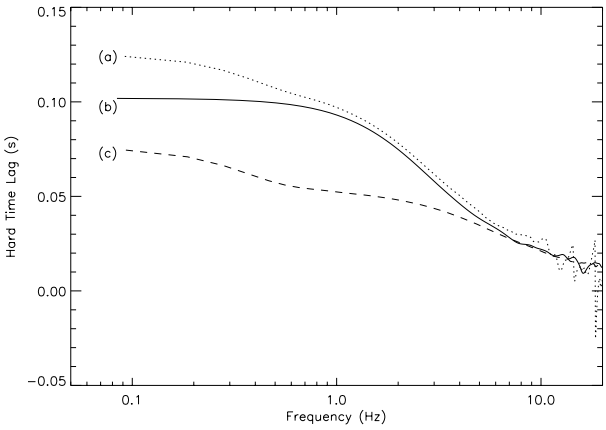

Figure 5.4: Comparison of time lags for various values of the ratio of the inner cloud radius to the outer cloud radius for the MCS model. Curve (a) is for the model where the ratio of the inner and outer radii is 0.1, while curve (c) is for a ratio of 0.05. Also shown are the lags due to the inner core only (curve b). The radius of the inner core in that case is taken to be 0.1 light seconds. The difference between curves (a) and (b) at low frequencies is due to the outer shell of plasma.

the value of the outer radius (for any fixed ratio of the two radii) simply changes the location of the curve in frequency − time lag parameter space without changing the shape of the curve. The electron temperature and optical depth of the clouds, as well as the temperature of the blackbody source photons, are the same as for Section 5.3, that is, for the inner cloud $\tau_{inner} = 2.39$ with electron temperature $kT_e = 76.7$ keV, and for the outer shell $\tau_{outer} = 0.06$ with electron temperature $kT_e = 396$ keV. The blackbody temperature is 130 eV.

The lags between two different bands, $2 - 10$ keV and $0.01 - 10$ MeV (which in this Chapter are referred to as bands one and two, respectively) are calculated with the central illumination of the cloud by the source photons taken to be an instantaneous delta function in time. Because so few photons scatter in the low optical depth outer cloud, the second band has been made large in order to make the two light curves comparable in intensity.

Figure 5.3a shows the intensity light curves as a function of time in the two bands, where the inner cloud radius is 0.03 light seconds. There is a flattening of the light curve at around 0.1-0.2 seconds due to photons scattering in the outer cloud. Although the overall spectrum is largely insensitive to the ratio of the inner and outer cloud radii,

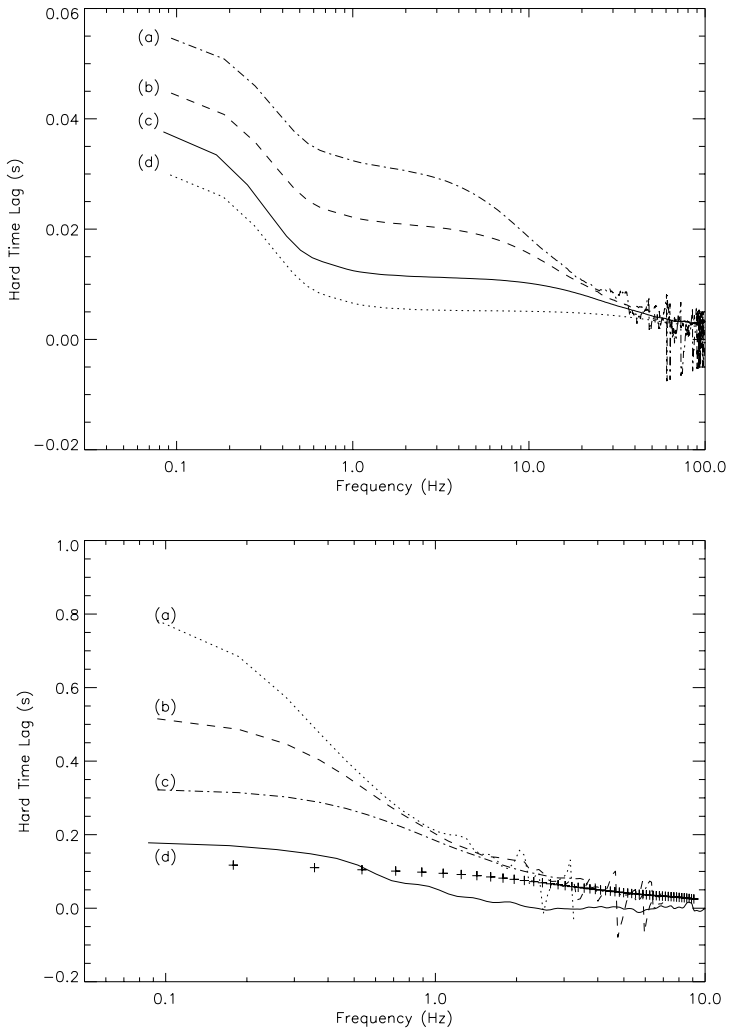

Figure 5.5: (a, top panel) Comparison of time lags for various small values of the ratio of the inner cloud radius to the outer cloud radius for the two-zone model. Curve (a) is for a ratio of 0.03, curve (b) is for a ratio of 0.02, curve (c) is for a ratio of 0.01 and Curve (d) is for a ratio of 0.005. (b, bottom panel) Comparison of time lags for various large values of the ratio of the inner cloud radius to the outer cloud radius for the two-zone geometry. Curve (a) is for a ratio of 0.8, curve (b) is for a ratio of 0.5, and curve (c) is for a ratio of 0.3. Curve (d) are the lags due to a cloud of radius one light second with parameters equal to the outer shell plasma in the MCS model. The crosses indicate the lag for a different pair of energy bands (2-10, 10-400 keV), where the ratio of radii is 0.1.

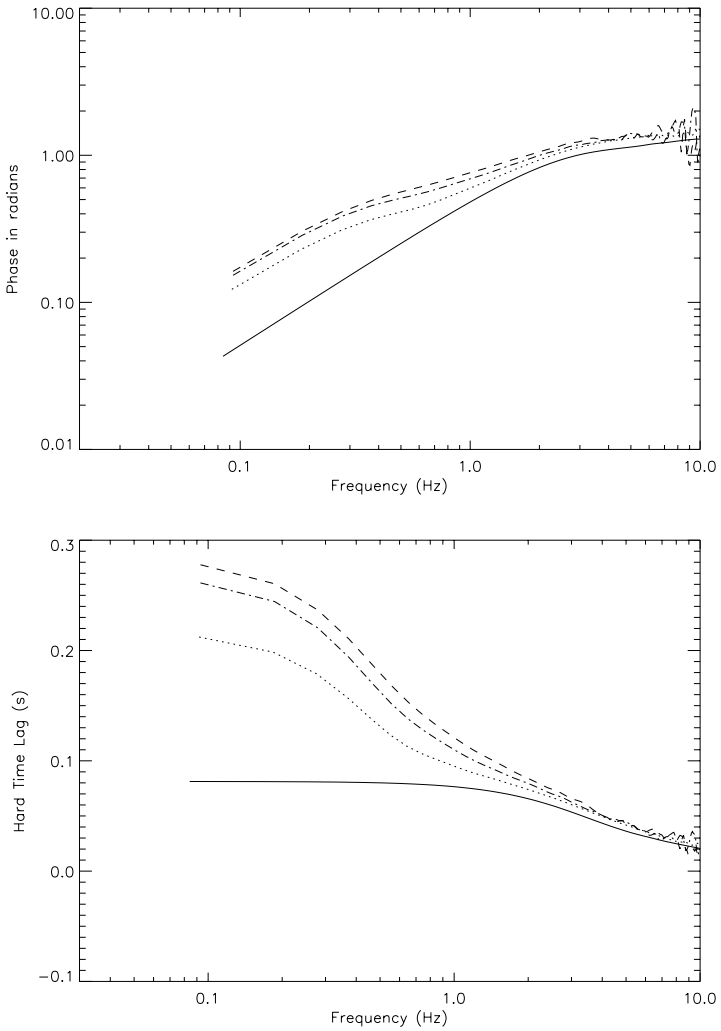

Figure 5.6: (a, top panel) Phase lag curves for the energy bands $2-10$ and $10-100$ keV bands, for optical depths of $0, 0.5, 1.0$ and 1.5 in the outer zone, for the solid, dotted, dot-dashed and dashed curves, respectively. The optical depth of the inner zone is fixed to 2, while the ratio of the inner and outer radii is 0.1. The temperatures of the inner and outer zones are those of the MCS model, with the same blackbody source as for the MCS. (b, bottom panel) The corresponding time lag curves.

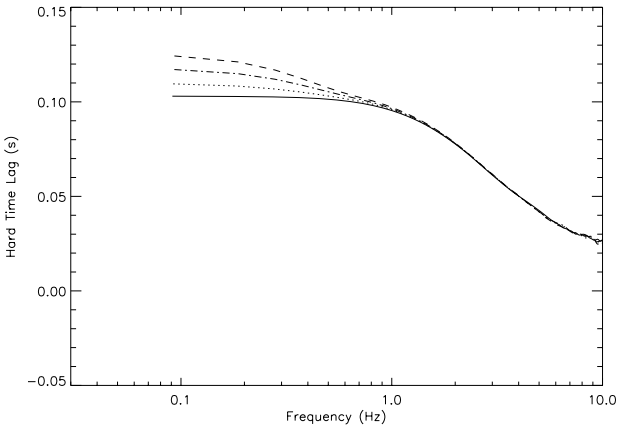

Figure 5.7: Time lag curves for the energy bands $2 - 10$ and $0.01 - 10$ MeV bands, for temperatures of $100.0, 200.0, 300.0$ and 400.0 keV in the outer zone, for the solid, dotted, dot-dashed and dashed curves respectively. The temperature of the inner zone is fixed to 76.7 keV (the MCS value), while the ratio of the inner and outer radii is 0.1. The optical depths of the inner and outer zones are those of the MCS model, with the same blackbody source as for the MCS.

variations in this ratio do result in different light curves as more or fewer photons scatter in the outer cloud, and therefore result in different hard time lags when Fourier transformed.

Figure 5.3b shows the phase lag between bands one and two as a function of Fourier frequency for two different models. The solid curve is the two-zone model with temperatures and optical depths as in Section 5.3. The dotted curve is the phase lag for a homogeneous cloud of plasma with temperature and optical depth equal to that of the inner core of the two-zone model. In both cases the outer radius is set to one light second. The solid curve develops a second peak at low frequencies, while the dotted curve is single-peaked. This rise in the solid curve at low frequencies is due to the change in temperature and optical depth in the outer shell of plasma in the two-zone model. This therefore indicates the possibility of determining if the two-zone geometry exists in BHCs.

Figures 5.4, 5.5a and 5.5b show the hard time lag curves between bands one and two as a function of Fourier frequency for various values of the inner cloud radius. For comparison, figure 5.4 also shows the time lags due to the inner cloud only (that is, with the outer plasma shell removed). With the outer shell added there is a larger lag at low

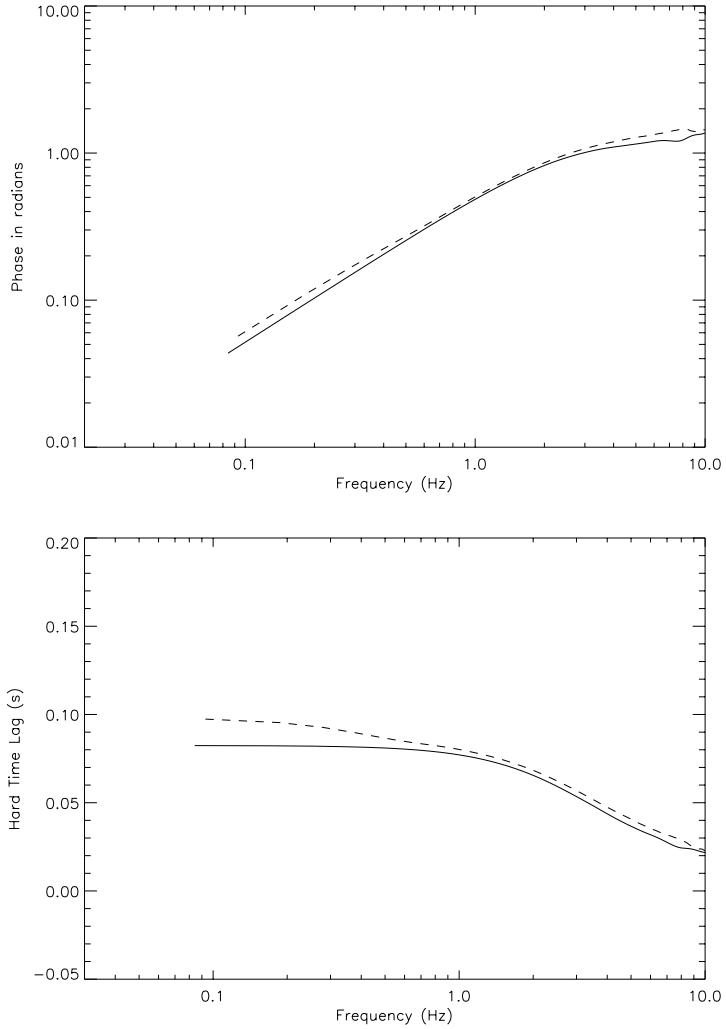

Figure 5.8: (a, top panel) Phase lags for the MCS model for the $2-10$ and $10-100$ keV bands, with the other parameters as before. (b, bottom panel) The corresponding time lags.

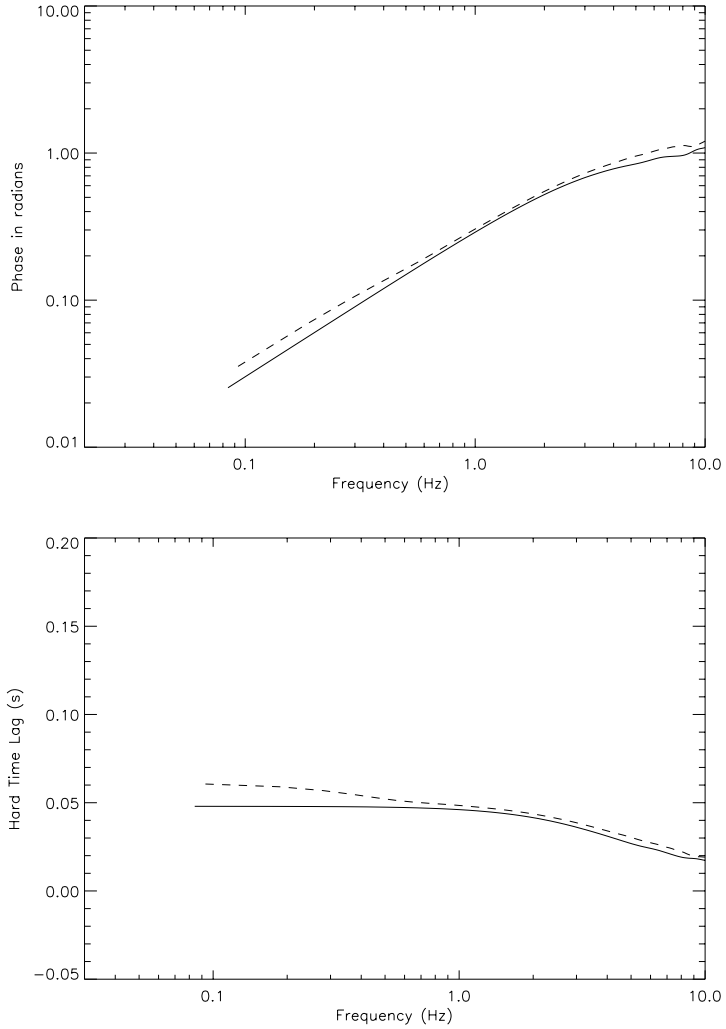

Figure 5.9: (a, top panel) Phase lags for the MCS model for the $2-10$ and $10-20$ keV bands, with the other parameters as before. (b, bottom panel) The corresponding time lags.

frequencies than for the inner cloud alone. This is the key difference between simple spherical corona models and the multi-temperature model due to MCS.

Figure 5.5a shows that for small inner-radius values, the lags become almost constant at high frequencies as the inner radius is made small, but there is still a peak at low frequencies. For large inner-radius values (figure 5.5b), one is seeing the inner cloud/core only, as fewer photon scatter in the relatively smaller outer cloud/shell. Figure 5.5b also shows the lags due to a spherical corona with electron temperature and optical depth equal to that of the outer cloud/shell in the two-zone model. This is equivalent to making the inner cloud radius and optical depth approach zero.

The crosses in figure 5.5b show the lags for a different pair of energy bands ($2-10$, $10-400$ keV, where the ratio of radii is 0.1). Because these bands do not extend up to gamma-ray energies, fewer high energy photons from the outer corona have contributed to the time lag curve. The lags are therefore almost constant with frequency as one is essentially seeing just the inner corona. In this case the lags tell us little about the outer corona.

It is possible that the various time lag curves could be used to determine the ratio of the inner and outer radii, as well as set the overall scale of the corona. Given the temperatures and optical depths (from spectral modeling) of the inner and outer coronae, the shape of the hard time lag curve determines the ratio of the inner and outer radii, while the position of the hard time lag curve in the frequency $-$ time lag parameter space determines the magnitude of the outer radius. Thus if the optical depths and the values of the radii are known, then the density of the corona is known, and one can in principle know all the physical parameters of the corona (in the context of the two-zone model). It is also possible that the outer radius can be found from other criteria, perhaps by identifying the break in the power spectral density of a light curve with the value of the outer radius as suggested by Böttcher & Liang (1998).

Figure 5.6 investigates variations in the optical depth of the outer shell. Here, optical depth parameters different from those of the MCS model have been chosen. For the inner cloud, $\tau = 2.0$ (solid line), while the optical depth of the outer shell is set to $0.5, 1.0$ and 1.5 for the dotted curve, dot-dashed curve and the dashed curve respectively. Again, the magnitude of the time lag increases at low Fourier frequencies compared to the no-shell case. The time lag curve seems to be reasonably sensitive to variations in the optical depth of the outer shell.

Figure 5.7 investigates variations in the temperature of the outer shell. Here, the optical depth of the inner and outer clouds are chosen to be those of the MCS model. For the inner cloud, the temperature is 76.7 keV, while the temperature of the outer shell

is set to $100.0, 200.0, 300.0$ and 400.0 keV for the solid curve, dotted curve, dot-dashed curve and the dashed curve respectively. At the lowest temperature, the time lag curve is essentially formed due to scattering in the inner cloud only, since photons are not scattered up to energies greater than ~ 100.0 keV and the light curves closely resemble those for the case of no outer cloud at all. As the outer cloud temperature increases, there is a rise in the curve at low Fourier frequencies ($0.1 - 0.2$ Hz). Overall, there is not much variation in the time lag curve with temperature in the outer cloud, with variations in optical depth (figure 5.6) having the larger influence on the time lags.

A more exact treatment of the curves in Figure 5.7 would begin by noting that since the scattering cross-section depends on temperature as well as density, to determine the effect of temperature only one should also vary / scale the density of the outer corona so as to keep the probability of scattering constant. Since the cross-section decreases with increasing temperature, the density in such a simulation would have to be increased to maintain the same scattering probability.

Figures 5.8 and 5.9 investigate the choice of different energy bands on the phase and time lags, for the MCS model. Figure 5.8 shows the lag between the $2 - 10$ and $10 - 100$ keV bands, while Figure 5.9 shows the lag between the $2-10$ and $10-20$ keV bands. The solid line is for the inner sphere only, and the dashed curve is for both the inner sphere and outer shell. There is an increase in the time lag curve at low Fourier frequencies of about 0.02 seconds, for both the figures. However the maximum time lag is larger in the case where the high energy band extends up to higher energies ($10 - 100$, figure 5.8) than it is when the high energy band is $10 - 20$ (figure 5.9). This is because it takes some extra time to scatter photons up to energies approaching 100 keV.

5.5 Conclusion

This Chapter has investigated in detail the two-zone model for the geometry of the plasma surrounding BHCs. In particular, this study has calculated the full spectrum produced by this model using a Monte Carlo simulation, as well as the time dependent light curves produced by Comptonization of a soft radiation flare at time zero, and the hard time lag curve between different energy bands. This is the first time the light curves and the hard time lags from a plasma with the two-zone geometry have been investigated numerically. It is found that Monte Carlo investigation of photon time lags between different energy bands can possibly be used to constrain this multi-temperature geometry for the accretion disk corona around galactic BHCs.

The energy spectrum is largely insensitive to the values of the radii used for the inner and outer clouds, as in general a Comptonized spectrum is sensitive only to the temperature and optical depth of the plasma (and the initial photon distribution if the plasma is optically thin). However, it is found that the time lag curve between energy bands is sensitive to the ratio of the two radii. This is the main result of the work in this Chapter; a sharp rise in the time lag curve at low Fourier frequencies is the temporal signature of the MCS model.

Variations in the optical depth and the temperature of the outer shell were investigated. The magnitude of the lag at low Fourier frequencies increases with both increasing optical depth and increasing temperature. However, it is seen that the time lag curve is more sensitive to variations in the optical depth (figure 5.6) than variations in temperature (figure 5.7). This may be due to the choice of energy bands, which were wide enough to bin photons regardless of whether those photons scattered in 100.0 keV plasma or 400.0 keV plasma.

Variations in the choice of energy bands were also investigated. The magnitude of the lags is larger when one of the energy bands extends up to higher energies, however judging from these results (figure 6.6 and figure 6.7) the dependence on the energy bands is not strong. A rise in the phase / time lag curve at low Fourier frequencies ought to be a general prediction for two-zone corona models with a hotter outer shell, even if the energy bands are somewhat different from those chosen here.

MCS also consider the case where bremsstrahlung photons from the tenuous outer corona are a significant spectral component. However, if the bremsstrahlung photon flux is stationary, then this component will make no contribution to the Fourier transform of the light curves, and therefore no contribution to the time lag curve. This will be the case as long as any fluctuations in the bremsstrahlung flux are small compared to the amplitude of the central Comptonized pulse. Similarly, any time independent processes such as electron-positron annihilation should not contribute significantly to the time lags.

Thus the time delay or lag can be used to determine the overall size of the corona and the ratio of the inner and outer radii, if this two-component corona geometry exists. This information combined with values for the optical depth obtained from spectral modeling can then tell us the overall density of the corona. Such a result would then give us all the physical parameters of the plasma cloud.

Observationally, the phase lag curve for galactic BHCs is typically constant with Fourier frequency (Miyamoto 1988). If the rise feature is unobserved, the absence of the feature could in theory place a constraint on the optical depth (and perhaps the

temperature) of any outer corona. If a two-zone model is found to be unviable using the time lags technique, other models for gamma-ray production will then be required.

References

Bisnovatyi-Kogan, G. S. & Blinnikov, S. I. 1976, Soviet Astron. Lett., 2, 191

Böttcher, M. & Liang, E. P. 1998, ApJ, 506, 281

Böttcher, M. & Liang, E. P. 1999, ApJ, 511, L37

Dove, J. B., et al. 1997, ApJ, 487, 759

Esin, A. A., et al. 1998, ApJ, 505, 854

van der Hooft, F., et al. 1999, ApJ, 513, 477

Johnson, W. N., et al. 1993, A & AS, 97, 21

van der Klis, M., et al. 1987, ApJ, 319, L13

Kazanas, D., Hua, X. M. & Titarchuk, L. G. 1997, ApJ, 480, 735

Li, H., Kusunose, M. & Liang, E. P. 1996, ApJ, 460, L29

Maccarone, T. J., Coppi, P. S. & Poutanen, J. 2000, ApJ, 537, L107

Misra, R. 2000, ApJ, 529, L95

Miyamoto, S., et al. 1988, Nature, 336, 450

Moskalenko, I. V., Collmar, W. & Schönfelder, V. 1998, ApJ, 502, 428

Nowak, M. A., et al. 1999, ApJ, 515, 726

Pottschmidt, K., et al. (in press) astro-ph/0008059

Poutanen, J. & Fabian, A. C. 1999, MNRAS, 306, L31

Poutanen, J. 2000, "X-ray Astronomy 1999" meeting, astro-ph/0002505

Pozdnyakov, L. A., Sobol, I. M. & Sunyaev, R. A. 1983, Ap. & Space Sci. Reviews, 2, 189.

Sunyaev, R. A. & Titarchuk, L. G. 1980, A&A, 86, 121

Vaughan, B. A. & Nowak, M. A. 1997, ApJ, 474, L43

Chapter 6

Compton scattering in bulk accretion flows

Inspired by previous studies of bulk motion Comptonization in converging accretion flows, the techniques discussed in Chapter 3 are applied here to the study of scattering in bulk motion accretion flows in both one and two dimensions.

Firstly, the case of line photon scattering in the accretion column of a magnetised white dwarf star (1D) is considered, with the resulting spectra presented for various inclination angles, accretion rates, and Cyclotron cooling rates in the post-shock region. Spectra as a function of inclination angle are also obtained, so that beaming of photons by the inhomogeneous column can be investigated.

Secondly, the case of Comptonization in a rotating torus geometry (2D) is considered, which is a first attempt at considering scattering in an orbiting accretion disk-like structure. Different photon injection spectra (a line, a power law and a blackbody) are investigated for different values of electron momentum. It is found that for a reasonable optical depth and electron momentum, lines can be significantly broadened by rotational Compton scattering.

6.1 1D: Accretion column

6.1.1 Accretion column in magnetic white dwarf stars

Magnetised white dwarf stars that accrete material from a binary companion star are sources of X-rays. After spilling out of the Roche lobe of the companion, the accreting

material is channeled by the magnetic field lines of the white dwarf into an accretion column which falls onto the pole of the white dwarf star.

A standing shock is formed near the base of the accretion column where the energy associated with free-fall is thermalised. The shock temperature is

$$kT_s = 16\,(M/0.5M_\odot)(R/10^9\mathrm{cm})^{-1}\,\mathrm{keV} \tag{6.1}$$

for a white dwarf of 0.5 solar masses and radius $10^9\mathrm{cm}$ (Frank, King & Raine 1985). Observational evidence for a temperature distribution in the post-shock plasma was presented by Ishida, Mukai & Osborne (1994). There are also expected to be velocity and density gradients in the post-shock region, which are predicted by hydrodynamic models of the accretion column (Aizu 1973, Wu, Chanmugam & Shaviv 1994).

Iron Kα and Kβ lines have been observed, for instance in EX Hydrae (Ishida et al. 1994). These are interpreted as being emitted by optically thin thermal plasma within the accretion column. The emissivity functions of Fe, Ar, S, Si and Mg have been studied (Fujimoto & Ishida 1997) and are found to peak towards the base of the accretion column, except for Fe which can be emitted at the shock.

White dwarf accretion columns can, for certain accretion rates, be sufficiently optically thick to scatter large numbers of line photons. Here, a Monte Carlo technique is used to investigate line photons that have scattered in an accretion column with density, temperature and velocity gradients. Spectra of escaping photons as a function of inclination angle are also presented. The photon transport within the accretion column is treated using the technique presented in Chapter 3.

6.1.2 Description of the numerical approach: column

The code developed for this application uses the Monte Carlo technique to simulate the scattering of line photons and free electrons in an accretion column of material, that is falling onto a weakly magnetised white dwarf star. The accretion column is modeled as a cylinder of material above the white dwarf pole (see figure 6.1). Within the accretion column, the density and velocity of the material above the shock are taken to be constants, while below the shock the density, velocity and temperature profiles are given by expressions presented in Wu et al. 1994. As discussed above, these profiles also include cooling of the post-shock material due to cyclotron radiation and to Bremsstrahlung radiation. The profiles are tabulated in arrays, to be used as needed.

The parameters of the accreting plasma used here are given by the hydrodynamic model of Wu, Chanmugam & Shaviv (1994). These authors solved the one-dimensional

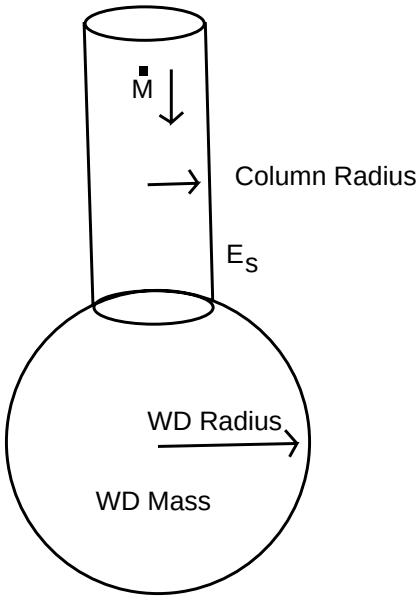

Figure 6.1: Schematic diagram of the white dwarf accretion column as modeled here. The parameters of the model are the white dwarf mass and radius, the specific accretion rate $\dot{m}$, the radius of the accretion column and the ratio of Bremsstrahlung cooling to Cyclotron cooling in the post-shock region ϵ_s.

hydrodynamics problem for accretion shock structures as well as for the shock height. The resulting expressions describe the temperature, density and velocity distributions of the plasma as a function of height in the accretion column. The formalism also includes radiative cooling of the post-shock electrons. Usually, Bremsstrahlung emission is considered as the dominant cooling mechanism for the post-shock electrons. However, Wu et al. (1994) also take into account Cyclotron emission, which is also considered here. When additional (e.g. Cyclotron) cooling is important, the height of the pressure-supported shock above the white dwarf surface is reduced as the post-shock region is cooled more efficiently.

Line photons are injected into the accretion column on a plane at some arbitrary height. For the purposes of this work, photons are either injected at the base of the accretion column, or at the shock. Photons are then given an initial random direction of propagation in the rest frame of the flow. If the photon is being injected at the shock, the initial propagation vector is Lorentz transformed out of the flow frame and into the white dwarf rest frame. The photon then propagates some distance to a possible (tentative) scattering point, the distance to which is determined using the full (relativistic)

Klein-Nishina cross-section and a variant of the non-linear transport technique introduced by Stern et al. 1995. As this is a rejection technique, not every tentative scattering event is accepted.

The original Stern rejection algorithm assumed a constant electron density. Here the algorithm is modified to include an integration over the varying electron density (in the post-shock region), but otherwise the algorithm is unchanged (see Chapter 3).

At a tentative scattering point the momentum vector of an electron is drawn from an isotropic Maxwellian distribution, whose temperature is given by the value of the temperature profile at this point (read from the arrays of tabulated values). The electron momentum vector is then Lorentz transformed out of the flow rest frame and into the white dwarf frame, using the velocity of the flow at the point. (The expression for Lorentz transforming a vector can be found in, for instance, Hua 1997). This gives the 'resultant' electron momentum vector, in the sense that part is due to thermal motion and part is due to the bulk motion of the flow. Based on the electron and the photon, the rejection algorithm then decides whether to accept or reject the scattering event. The probability of accepting the event is determined using Eq. 3.13, which depends on the cross-section and the relative velocity between the electron and photon.

If a scattering event does take place, the energy shift of the photon, and the change in propagation direction, are modeled according to the prescription given by Pozdnyakov, Sobol and Sunyaev (1983), again using the full Klein-Nishina cross-section.

Photons are followed until they escape from the accretion column, and are binned in energy for a given viewing angle. Here viewing angles of $30°$ and $60°$ are investigated. Furthermore, all escaping photons are binned in angle. Photons that hit the white dwarf surface are disregarded and do not contribute to the final spectrum.

The code inputs are the mass and radius of the white dwarf star, the specific accretion rate within the accretion column, the width of the accretion column, and the ratio of Cyclotron cooling to Bremsstrahlung cooling in the post-shock region. The code being used in this Section is used here in a 'linear' mode, so the value of the time step used by the code does not effect the results (this also holds for the code discussed in Section 6.2).

The procedure just described treats both the photon transport and the photon scattering accurately. The full white dwarf code is presented in the appendix of this thesis.

6.1.3 Results

The spectra have been investigated for different accretion rates, viewing angles, photon injection sites and cyclotron cooling ratios. The results are plotted in figures 6.2 - 6.6.

For all these figures, the radius of the accretion column was taken to be 10% of the white dwarf radius, while the mass and radius of the white dwarf were $0.5M_{\odot}$ and $10^9\mathrm{cm}$. For figures 6.2 - 6.4 the ratio of the Bremsstrahlung cooling timescale to the Cyclotron cooling timescale at the shock, ϵ_s (as defined in Wu et al. 1994), is set to zero (Bremsstrahlung cooling only).

Figures 6.2a and 6.2b show spectra for a specific accretion rate of $4\ \mathrm{g\ s^{-1}cm^{-2}}$ (solid lines), seen at $30°$ inclination (Figure 6.2a), and at $60°$ inclination from the axis of the accretion column (Figure 6.2b). The photons are injected at the shock with an energy of 6.7 keV in the rest frame of the accreting material. The dashed lines are the same except the specific accretion rate is $40\ \mathrm{g\ s^{-1}cm^{-2}}$.

Figures 6.3a and 6.3b are for the same parameters as figures 6.2a and 6.2b, except here the photon injection site is at the base of the accretion column.

To interpret figures 6.2 and 6.3, consider first those photons that scatter in the pre-shock material. In a homogeneous cold column, a typical spectrum consists of a double peaked structure, followed by a 'plateau' at lower energies, and a low energy tail. When the photon injection site is located near the white dwarf, the backscattered photons of the second (lower energy) peak have a much greater chance of hitting the white dwarf surface and being absorbed. The result is that the second peak gets is diminished as the injection site approaches the surface. The resulting spectra have a strong first peak, in some cases a remnant of the second peak, and the plateau due to photons that have scattered subsequent times. This is superimposed on a very broad feature that is due to those photons that have scattered in the post-shock material. Those photons that have encountered hot electrons near the shock are upscattered to higher energies, while photons that scatter in the dense, cool material near the white dwarf surface can lose significant amounts of energy. This results in broad wings that extend off to both higher and lower energies. Figures 6.2 show lines with the remnant of the backscattered peak between 6.7 keV and 6.5 keV. Because the photon injection site in Figures 6.3 is closer to the white dwarf surface, the backscatter peak is gone, and the peak at 6.7 keV joins smoothly onto the plateau feature.

Figures 6.4a and 6.4b show the spectrum (the number of escaping photons) as a function of the angle $\theta \equiv \cos^{-1}(\mu)$, where $\mu = 1.0$ corresponds to the direction along the column away from the white dwarf, and $\mu = -1.0$ corresponds to the direction along the column towards the white dwarf. Figure 6.4a is for the parameters used in figure 6.2, while Figure 6.4b is for the parameters used in figure 6.3. At higher accretion rates, more escaping photons are beamed down towards the white dwarf, especially if the photons are injected at the base of the column (figure 6.4b).

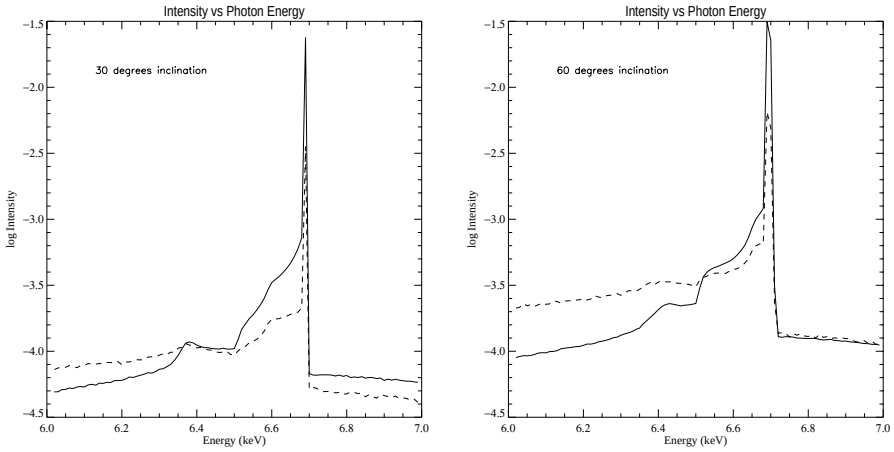

Figure 6.2: (a, left panel, and b, right panel) Spectra for photon injection at the shock. The specific accretion rate is $4\ \mathrm{g\ s^{-1}cm^{-2}}$ (solid lines) and $40\ \mathrm{g\ s^{-1}cm^{-2}}$ (dashed lines). The viewing or inclination angle was $30°$ (left panel) and $60°$ (right panel). $\epsilon_s = 0$.

Figures 6.5a and b show spectra for cases when Cyclotron cooling is present in the post-shock region. The ratio Bremsstrahlung cooling to Cyclotron cooling ϵ_s has been set to 1 (solid line) and 10 (dashed line). The accretion rate is $4\ \mathrm{g\ s^{-1}cm^{-2}}$ (the same as the previous figures). The lines are injected at the shock and are viewed at an angle of $30°$. There is little difference in the line shapes for these two cases. The dot-dashed curve represents the spectrum when $\epsilon_s = 10$ and the accretion rate is large, $\dot{m} = 60\ \mathrm{g\ s^{-1}cm^{-2}}$. The step at 6.7 keV is still visible, as are photons near the original injection energy of 6.7 keV. The spectrum as a function of angle corresponding to this case is the dot-dashed line in figure 6.5b. Fewer photons are escaping, as more photons impact on the white dwarf surface when the accretion rate is high.

Figure 6.6a represents the case when photons are injected at the base of the accretion column and Cyclotron cooling is dominant (ϵ_s large). Figure 6.6b is the corresponding spectrum as a function of angle. Almost all photons that escape are traveling upward, and fewer are escaping at $90°$ compared to figure 6.5b.

6.1.4 Discussion

The height of the accretion shock depends on the accretion rate in the column, and to a lesser extent the cooling efficiency of the post-shock electrons. Consider the case where

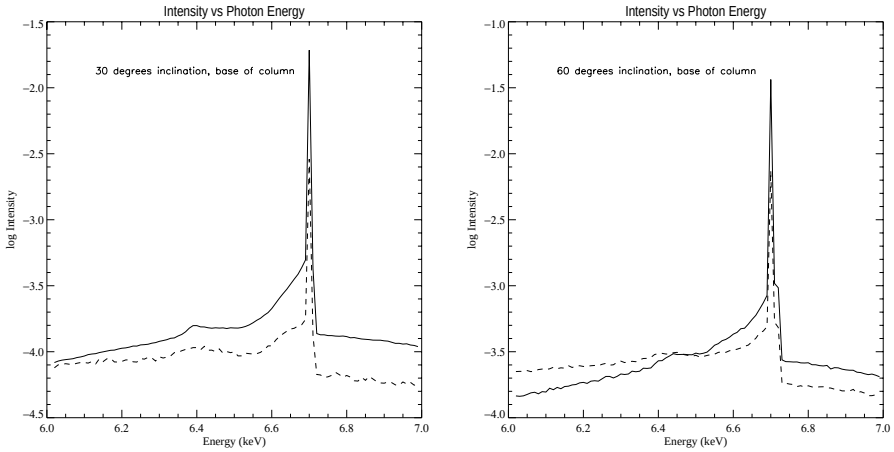

Figure 6.3: (a, left panel, and b, right panel) Spectra for photon injection at the base of the accretion column. The specific accretion rate is $4\ \mathrm{g\ s^{-1}cm^{-2}}$ (solid lines) and $40\ \mathrm{g\ s^{-1}cm^{-2}}$ (dashed lines). The viewing or inclination angle is indicated.

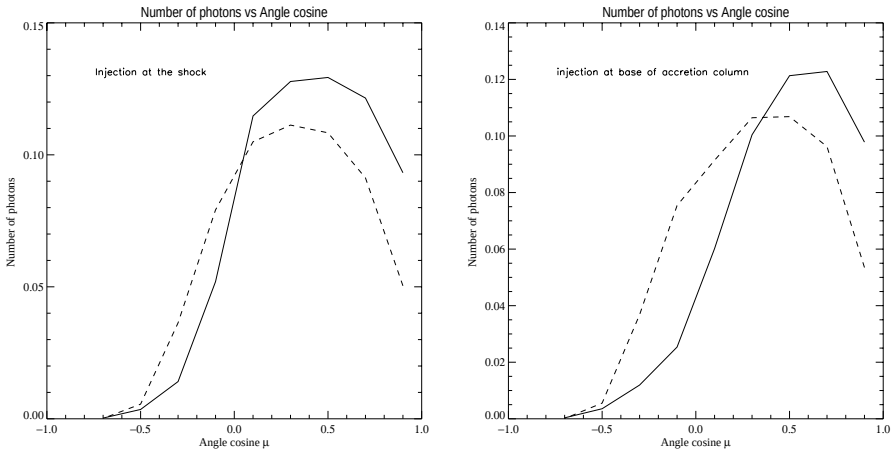

Figure 6.4: (a, left panel, and b, right panel) Specta as a function of angle for the case investigated in figure 6.2 (injection at the shock, left panel) and for the case investigated in figure 6.3 (injection at the column base, right panel). The solid lines are for a specific accretion rate of $4\ \mathrm{g\ s^{-1}cm^{-2}}$ and the dashed lines are for $40\ \mathrm{g\ s^{-1}cm^{-2}}$.

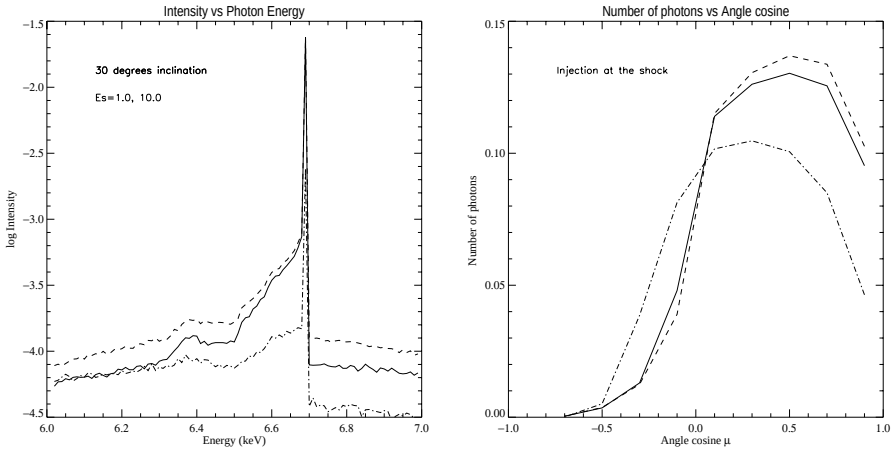

Figure 6.5: (a, left panel, and b, right panel) Spectra for photon injection at the shock. The specific accretion rate is $4\ \mathrm{g\ s^{-1}cm^{-2}}$ (solid and dashed lines). The viewing angle for all cases is $30°$. $\epsilon_s = 1.0$ for the solid line and 10.0 for the dashed line. The dot-dashed curve corresponds to an extreme case of large ϵ_s (10.0) and large accretion rate $(60\ \mathrm{g\ s^{-1}cm^{-2}})$. The right panel shows the corresponding spectra as a function of angle for the solid line, dashed line and the dot-dashed case.

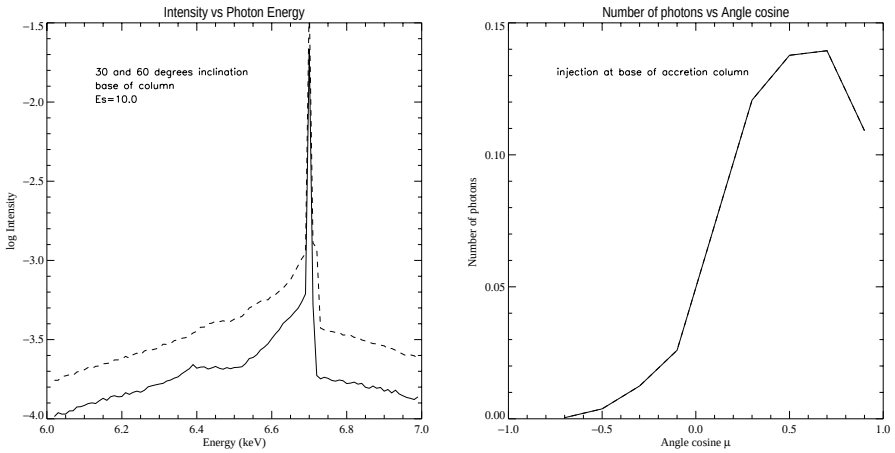

Figure 6.6: (a, left panel, and b, right panel) Spectra for photon injection at the base of the accretion column. The specific accretion rate is $4\ \mathrm{g\ s^{-1}cm^{-2}}$ (solid and dashed lines). The viewing angle is $30°$ for the solid line and $60°$ for the dashed line. $\epsilon_s = 10$ for both cases. The right panel shows the corresponding spectrum as a function of angle for this accretion rate and ϵ_s value.

photons are injected at the shock (figure 6.2). For moderate accretion rates (solid lines), the spectra consist of the 6.7 keV feature, a flat shelf or 'plateau' feature of constant intensity, and the remnant of the backscatter peak between them. At higher accretion rates (dashed lines) the backscatter peak is reduced as the shock moves downwards towards the white dwarf surface. This is due to the photons that would have contributed to the peak having a large probability of impacting onto the white dwarf surface. However the peak at 6.7 keV is always prominent, even for large accretion rates, because of photons emitted by material near the sides of the accretion column. At very high accretion rates the spectrum is smeared out, except for the 6.7 keV feature, and a step-like feature above 6.7 keV (figure 6.5a, dot-dashed curve).

For photons injected at the base of the column (figure 6.3), the backscatter feature is not recognisable, and the 6.7 keV peak joins smoothly onto the plateau feature. At higher accretion rates (dashed), the region to the low energy side of the 6.7 keV peak is 'flattened out' and smeared into one broad feature.

At high accretion rates, the injection site (at the shock or at the base of the column) makes little difference, as the shock moves down towards the base of the column so that in either case photons are being injected close to the white dwarf surface (comparing the dashed lines in figures 6.2 and 6.3).

Variations in the cooling parameter ϵ_s also make little difference to the spectra (figure 6.5a) unless ϵ_s is large (Cyclotron dominated post-shock region). For $\epsilon_s = 10.0$ (figure 6.6a) the viewing angle determines whether the plateau feature is seen, with it being visible at $30°$ (solid line) but smeared out at $60°$ (dashed line).

The spectra plotted as a function of viewing angle (figures 6.4b, 6.5b and 6.6b) generally peak near $60°$ inclination for all cases investigated here. They are heavily weighted towards positive μ as photons traveling downwards have a great likelihood of striking the white dwarf surface. At higher accretion rates more photons escape at smaller μ values, as photons are beamed downwards by the accretion column material. Figures 6.4b, 6.5b and 6.6b in general are similar to each other, although for a moderate accretion rate the case of injection at the base results in plots that are narrower and more weighted to positive μ (figure 6.4). The spectra as a function of angle show little dependence on the cooling parameter ϵ_s (figure 6.5b).

Observationally, the iron Kα and Kβ lines seen by the CCD of the *ASCA* satellite are fit by Gaussians because of the resolution of the instrument (Ezuka & Ishida 1999). The computational spectra presented in this Chapter are non-Gaussian. In particular, the prominence of the 6.7 keV peak (in the simulations) is due to little optical depth being traversed by these photons, since they are emitted near the edge of the accre-

tion column. An absence (observationally) of this non-Gaussian peak feature, if found, would suggests that a more realistic source function would be one that is located centrally within the column. A greater amount of optical depth would then be seen by the photons, smearing the intensity distribution into a broader (Gaussian-like) feature. Additionally, a photon source (emissivity function) that is peaked towards the centre of the column might also suggest the presence of a radial temperature or density gradient, from the centre to the edge of the accretion column, in addition to the gradients along the length of the column (away from the white dwarf star) as studied here. The source function can be inferred from the scattered line structure if observed at high enough resolution, for instance with the grating spectrographs on board the *Chandra* satellite and XMM-Newton.

In summary, at high accretion rates the computational spectra are similar to each other for different inclination angles and injection heights. At moderate accretion rates, and at a given the inclination angle, it may be possible in principle to determine the injection height of the photons, from the presence or absence of the backscatter peak. However, to test this conjecture in future work one should include realistic emissivity functions, so photons are injected at different heights above the surface (a straightforward modification) and perhaps at different radii within the column. The code described here can also in principle treat the case of neutron star accretion, after a modification of the post-shock cooling law and the inclusion of light bending near the neutron star.

6.2 2D: Accretion disk

6.2.1 Rotating torus

The hard X-ray spectra of accreting compact objects is often interpreted in terms of Comptonization of soft photons off relativistic electrons. In this traditional interpretation, the scattering plasma is assumed to be isotropic and have either a power law or a Maxwellian distribution. Comptonization in such a plasma has been studied intensively over a number of years, both by analytic means (Sunyaev & Titarchuk 1980) and by means of Monte Carlo simulation (Pozdnyakov, Sobol & Sunyaev 1983; Stern et al 1995).

An alternative possibility is that the momentum of the electrons is not primarily due to an isotropic distribution, but rather is due to directed bulk motion of the plasma, or

some combination of the two (Colpi 1988). For instance, Laurent & Titarchuk (1999) have investigated the effects of bulk-motion Comptonization of soft photons, where the motion of the scattering electrons is primarily due to infall onto an accreting black hole, in order to determine whether Comptonization due to bulk infall motion can be a means of producing the hard X-rays observed from galactic black hole candidates.

The inverse Compton process requires a source of soft photons to be postulated, and the location of this source is generally taken to be the accretion disk. However, there exist models (e.g. Reynolds & Begelman 1997) that refer to a source of photons beyond the innermost stable orbit of the accreting matter. It has therefore been suggested that a ring or torus of material could form and be supported by radiation pressure from sources beyond the last stable orbit (Drake 2000). Accreting material in black hole systems is expected to form an accretion disk due to conservation of angular momentum, and so this putative ring of matter may also be identified with the 'inner rim' of an accretion disk, or perhaps a centrifugal boundary layer (CENBOL) near a black hole, as has been investigated by Chakrabarti & Titarchuk (1995), and Chakrabarti (2000).

For the case of motion near a Schwarzschild black hole, the angular component of velocity v^{ϕ} is given by the expression (Shapiro & Teukolsky 1983)

$$v^{\phi} = (1 - \frac{2M}{r})^{1/2} \frac{\tilde{l}}{r\tilde{E}} \ , \tag{6.2}$$

where for a circular orbit

$$\begin{aligned} \tilde{l}^2 &= \frac{Mr^2}{r-3M} \\ \tilde{E}^2 &= \frac{(r-2M)^2}{r(r-3M)}, \end{aligned}$$

with M the mass of the black hole, and r the radial coordinate. It is interesting to note that v^{ϕ} goes to zero at the event horizon (only radial geodesics exist as $r \rightarrow 2M$). Eq. 6.2 is plotted in figure 6.7 (dashed line). At the last marginally stable orbit ($r = 6M$) v^{ϕ}/c approaches 0.5. Beyond the last marginally stable orbit, the velocity v^{ϕ}/c approaches 1 at $r = 3M$. No circular orbits exist between $3M$ and $2M$.

For the case of circular equatorial orbits near a Kerr black hole, v^{ϕ} as seen from a locally non-rotating frame is given by (Bardeen, Press & Teukolsky 1972)

$$v^{\phi} = \frac{\pm M^{1/2}(r^2 \mp 2aM^{1/2}r^{1/2} + a^2)}{(r^{3/2} \pm aM^{1/2})(r^2 - 2Mr + a^2)^{1/2}} \ , \tag{6.3}$$

where $a \equiv J/M$ is the angular momentum per unit mass of the black hole. For the case

$a = M$, the above becomes

$$v^{\phi} = \frac{\pm M^{1/2}(r^{3/2} \pm M^{1/2} r + M r^{1/2} \mp M^{3/2})}{(r^{3/2} \pm M^{3/2})(r^{1/2} \pm M^{1/2})} \,. \tag{6.4}$$

The upper sign in Eq. 6.3 and Eq. 6.4 corresponds to direct (corotating) orbits, and the lower sign to retrograde orbits. When $a = M$, stable circular orbits exist down to the horizon at $r = M$ for direct orbits, at which $v^{\phi}/c = 0.5$, and down to $r = 9M$ for retrograde orbits, at which $v^{\phi}/c = 0.42$. Eq. 6.3 and Eq. 6.4 are also plotted in figure 6.7, for both direct and retrograde orbits.

An orbital velocity $v^{\phi}/c = 0.55$ corresponds to a dimensionless electron momentum parameter (P/mc) equal to 0.66, which in turn gives an energy of about 100 keV. If there exists a ring of matter at or near the last stable orbit, as considered by Drake, the orbital kinetic energy of electrons in the ring might be of the order of 100 keV as great or greater than the thermal energy. The orbital motion of material in the innermost regions of the accretion flow may then be sufficient for bulk motion Comptonization to become important.

The problem treated here is therefore that of bulk motion Comptonization with scattering off electrons in a circular orbit, rather than in free fall as has been investigated previously (Colpi 1988, Laurent & Titarchuk 1999). The Comptonization of photons due to the bulk rotational motion of electrons in a thick inner-rim of an accretion disk or a toroidal shaped centrifugal boundary layer, has not previously been considered.

It is expected that rotational motion causes lines to be broadened by an amount

$$\Delta\epsilon/\epsilon = (GM/Rc^2)^{1/2} = 0.72\ (M/10M_{\odot})^{-1/2}(\epsilon/6.7\mathrm{keV})^{-1} R_8^{-1/2} \tag{6.5}$$

(where $R_8 \equiv 10^8 \mathrm{cm}$) assuming Keplerian motion about a ten solar mass object (Kallman & White 1989). However this estimate does not take into account any additional broadening due to scattering.

In this Section, simulations of bulk rotational motion scattering are performed. The geometry of the inner-rim of an accretion disk or of the CENBOL is modeled here as a two dimensional torus of electrons illuminated by a central photon source. The resulting scattered spectra are investigated for different injection spectra (a line, a power law and a blackbody), and for different values of electron momentum. The next Subsection describes the numerical approach used to treat the model, with Sections 6.2.3 and 6.2.4 presenting the results and a discussion of the simulations carried out.

6.2.2 Description of the numerical approach: disk

Figure 6.8 shows the geometry this code considers. The torus, which resides in the $x-y$ plane (figure 6.7 shows a cross-section), is filled with electrons that rotate counter-clockwise when looking down from the positive 'z' direction. The electron orbital motion is treated by choosing the velocity vectors of the electrons to be in the $x-y$ plane perpendicular to the radius vector. The optical depth of the torus (defined along 'R2' on the diagram, $\tau = n\sigma(R2)$) is one of the input parameters of the code. The other input parameters are the ratio of the small axis to the large axis $R2/R1$, and the momentum of the rotating electrons in the ring, η. The density inside the torus is assumed to be constant: there are no density gradients across the ring.

The electron momentum $\eta \equiv P/m_e c$ is in dimensionless units. The Lorentz factor of the electrons can be obtained using the formula $\gamma = (\eta^2 + 1)^{1/2}$. The velocity v/c is then $(v/c) = \eta/\gamma$. In this version of the code there is no thermal motion of electrons, so the electron momentum comes from bulk rotation only. The scattering between the photons and electrons is exact using the Klein-Nishina cross-section.

The source of seed photons is modeled as a point source on the axis at the centre of the torus. Here three different types of injection spectra are considered; a blackbody, a line, and a power law. The blackbody photon source has a temperature of 0.1 eV, similar to the energy of AGN disk photons, the power law has an energy spectral index $\alpha = 1.0$, and the line has been given an energy of 6.4 keV. The code only injects photons that will pass through the torus. The transport is treated properly: photons can scatter, leave the ring, re-enter the ring at some other point (if they are heading in the right direction), and then scatter again.

Accurate photon transport is crucial for modeling this situation and so the code uses the method presented by Stern et al. (1995), which is applicable to bulk motion scattering. Consider a photon propagating outward. In this method, the code finds a 'possible' scattering point for the photon. To find the possible scattering point one does not have to specify what the electron velocity distribution is. Once a possible scattering point is determined the code then finds an electron for the photon to interact with. The possible scattering point is then either accepted or rejected based on the electron's velocity vector.

So in this version, the code determines a possible scattering point (x, y, z) in the ring, and then determines which direction the electrons are flowing at the point (x, y, z). (For instance, if the photon is traveling radially then the electron momentum vector will be at a right angle to the direction of photon propagation.) Using this electron

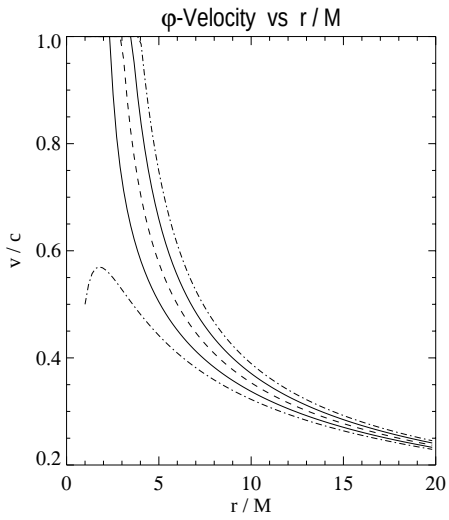

Figure 6.7: The magnitude of the ϕ-component of velocity for circular equatorial orbits about a Kerr black hole and a Schwarzschild black hole (dashed curve). The curves below the dashed curve are for direct (corotating) orbits about a Kerr black hole with angular momentum parameter $a \equiv J/M$ equal to $M/2$ (solid curve) and M (dot-dashed curve). The curves above the dashed curve are for retrograde orbits about a Kerr black hole with the angular momentum parameter again equal to $M/2$ (solid curve) and M (dot-dashed curve).

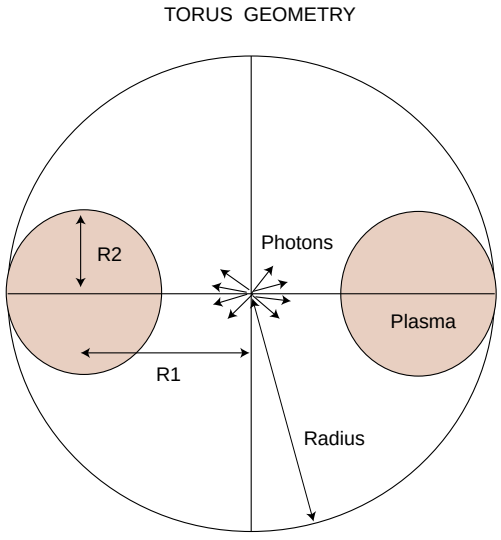

Figure 6.8: A cross-section through the torus geometry considered here. Photons are injected on the axis of the torus, scatter within the torus, and escape to form a Comptonized spectrum.

direction and the electron momentum, the scattering event is either accepted or rejected. If accepted, the scattering event is modeled (doing the kinematics properly) and the photon continues on in a new direction with a new energy. If the scattering event is rejected, the photon continues on in the same direction with the same energy, and (in the next timestep) a new possible scattering point is determined.

The torus is bounded by a sphere, and once photons are outside this sphere they have escaped and are not followed further. While photons are passing through the sphere, they can only scatter if they are inside the torus. Potential scattering events that land outside the torus are rejected and the photon continues on its path.

This idea of finding a possible event and then accepting or rejecting that event is a general one in Monte Carlo simulations (see Chapter 2). Essentially the idea is that if one has a problem with a complicated probability distribution, one starts by imagining a simple problem and solving that (the possible event). The trick then is to have some criteria for accepting or rejecting that event, which enables the calculation of the real case from the simple case. The algorithm rejects the events that are not consistent with the real case and keep those events that are.

The electrons in the simulation are assumed to be on circular orbits within a torus of material. The electrons are not followed from timestep to timestep, but it is assumed that at each timestep there are 'fresh' electrons for the photons to scatter off. That is, it has been assumed that the electron distribution is stationary in time and the photon flux does not disturb the torus. In a full treatment of the problem this should be refined to allow 'feedback' on the torus, and also the photon and electron transport should be general relativistic. Gravitational redshift is also not included in these simulations. These effects are left for future work.

6.2.3 Results

Shown in figures 6.9 - 6.18 are the results for various injection spectra and various values of the electron momentum. For the results presented here, the optical depth τ is fixed at 2.0 and the ratio $R2/R1$ is fixed at 0.1. With the exception of figure 6.12, in the top panel of each set of figures the solid curve is the input spectrum, the dashed curve is the total spectrum (integrated over all angles), and the dot-dashed curve is the spectrum seen at an inclination of $90°$ (edge on to torus) where the bin in angle is $10°$ wide ($85 - 95°$).

In the lower panel of each set of figures, the 3 curves are the spectra at $30°$, $60°$ and $90°$ inclination, (the dashed, dot-dashed and solid curves, respectively) with the $90°$ curve being the spectrum as seen from edge on to the torus. Most photons that scatter many

times come out in the plane of the torus because photons are mostly scattered in the direction the electrons are traveling. Therefore it is sometimes difficult to obtain the 30° and 60° curves, because so few photons come out at these angles. Because of this, the 30° curve is sometimes omitted from the plots presented here. Figure 6.11 has only one panel because for this case effectively all the photons emerge in the plane of the torus.

Recall that photons are injected so that they always pass through the torus; this means that observers at all inclination angles will actually see an unscattered injection spectrum from the central source in addition to the scattered component. The resulting plots present only the scattered component, with the understanding that an unscattered component will also be present in real sources.

Blackbody injection

Figures 6.9, 6.10 and 6.11 present results for a blackbody injection spectrum. The values of electron momentum η considered here are $3.0, 10.0$ and 30.0, corresponding to v^{ϕ}/c values of $0.95, 0.995$ and 0.999 respectively. These values are suitable for accelerated orbits as considered by Drake (2000), or for orbits beyond the last stable orbit.

The spectra are broadened by passage through the torus, but most photons are not scattered up to hard X-ray energies. When $\eta = 10.0$ some photons are scattered into the range $2.0 - 100.0$ keV, but for smaller values of η few X-rays can be produced by scattering of soft blackbody photons. There is no extended power law feature as would be produced by Inverse Compton (IC) scattering on an isotropic thermal distribution (and as seen, for instance, in Chapters 4 & 5).

At an inclination of 90° (solid curve, lower panel, figure 6.9) a peak due to unscattered blackbody source photons can be seen above 10^{-4} keV. Even though the torus is optically thick ($\tau = 2.0$) some photons do propagate through and escape without scattering. The second peak at around 10^{-2} keV is due to photons that have scattered in the torus. For $\eta = 3.0$ the scattered spectra retain their thermal shape, but are shifted to higher energies by IC scattering. As η increases, a 'bump'-like feature begins to appear at and above 10^{-1} keV. When $\eta = 10.0$ the bump feature becomes a flat 'shelf'-like feature.

Comparing the spectra at different inclination angles (lower panel, figures 6.9, 6.10 & 6.11), it is seen that the shape of the scattered spectra for an optically thick torus are always similar (ignoring the lower peak due to unscattered photons). However, the spectra are at systematically higher energies as the inclination angle increases. This is because photons are preferentially scattered into the direction of the electrons motion,

and since all the electrons in the simulation are traveling in the $x-y$ plane, photons that scatter more times and therefore have more energy (on average), are also more likely to be traveling in the $x-y$ plane. These photons will escape at high inclination angles, so the hardest photons will escape at $90°$.

Figure 6.12 shows the results for η set to the extreme value of 30.0. The dashed curve is the angle-integrated spectrum, and the dot-dashed curve is the spectrum at $90°$ inclination (the two are almost identical). Here significant numbers of X-rays and even gamma-rays are produced. The shelf-feature has formed into a second peak of scattered photons covering the range $2.0-100.0$ keV, and the scattered spectrum now appears 'lumpy', similar to the peaks that form due to thermal Comptonization in an optically thin plasma. Since in this case essentially all photons escape at high inclination angles, the spectra at other inclination angles are not presented.

Line injection

Figures 6.13 and 6.14 present results for a line at 6.4 keV being injected into the torus, with the more moderate values of $\eta = 0.33$ and 0.66, corresponding to v^{ϕ}/c values of 0.31 and 0.55 respectively. As before, the top panel shows the angle-integrated spectrum (dotted curve) and the spectrum at $90°$ (dot-dashed curve). The bottom panel shows the escaping spectra at $30°$, $60°$ and $90°$ inclination (the dashed, dot-dashed and solid curves, respectively).

In figure 6.13, the scattered spectra at moderate ($30°$, $60°$) inclination angles are double peaked, and are broad in energy, being $2-3$ keV wide. The width of the scattered line increases with increasing inclination angle. The escaping spectrum at $90°$, however, is broad and single peaked. The narrow spike superimposed on the broad profile is again due to unscattered photons passing through the torus and escaping.

In figure 6.14 the spectra at $30°$ and $60°$ inclination are similar in shape to the $\eta = 0.33$ case, but here the scattered lines are even broader due to the larger η value. The top of the spectrum at $90°$ is flatter than in the $\eta = 0.33$ case. The extra amount of up-scattering due to the larger η value appears to 'stretch-out' the spectrum. The low energy side of the spectrum seems to be about $4-5$ keV largely independent of the value of η, while the high energy side is shifted to higher energies for increasing values of η.

Figure 6.15 shows the results for a large value of η. Photons are up-scattered to a sharp peak, followed by a cutoff. The energy of the peak depends on the inclination angle (lower panel).

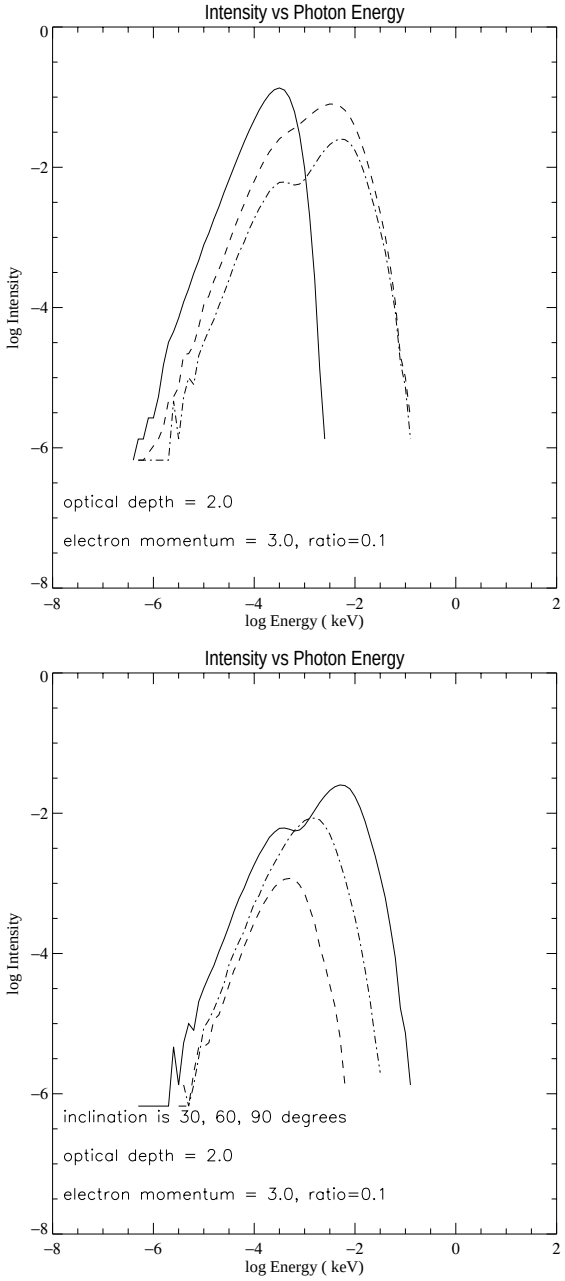

Figure 6.9: Blackbody photons IC scattered by an orbiting torus of electrons. In the top panel, the solid curve is the input spectrum, the dashed curve is the total spectrum (integrated over all angles), and the dot-dashed curve is the spectrum seen at an inclination of $90°$, where the bin in angle is $10°$ wide ($85 - 95°$). The momentum of the electrons in the torus $\eta = 3.0$. The optical depth of the torus, as defined along the axis $R2$, is fixed to be 2.0, while the parameter 'ratio', defined to be $R2/R1$, is fixed to 0.1. In the lower panel, the 3 curves are the spectra at $30°$, $60°$ and $90°$ inclination, (the dashed, dot-dashed and solid curves, respectively) with the $90°$ curve being the spectrum as seen from edge on to the torus.

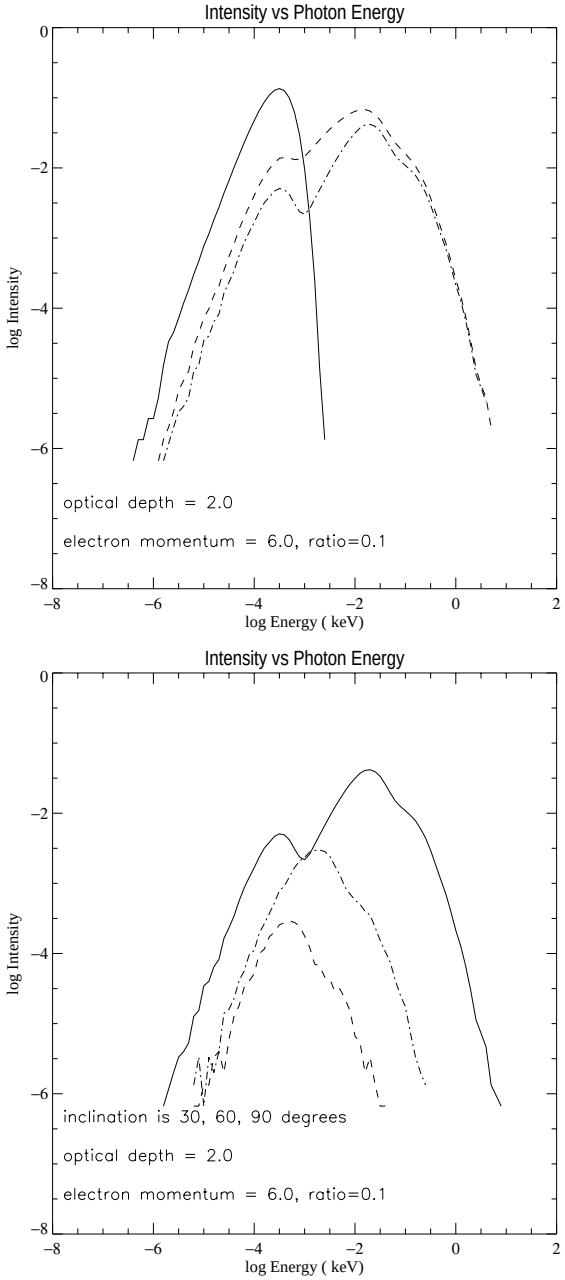

Figure 6.10: Blackbody photons IC scattered by an orbiting torus of electrons. In the top panel, the solid curve is the input spectrum, the dashed curve is the total spectrum (integrated over all angles), and the dot-dashed curve is the spectrum seen at an inclination of 90°. The momentum of the electrons in the torus $\eta = 6.0$. In the lower panel, the 3 curves are the spectra at 30°, 60° and 90° inclination, (the dashed, dot-dashed and solid curves, respectively) with the 90° curve being the spectrum as seen from edge on to the torus.

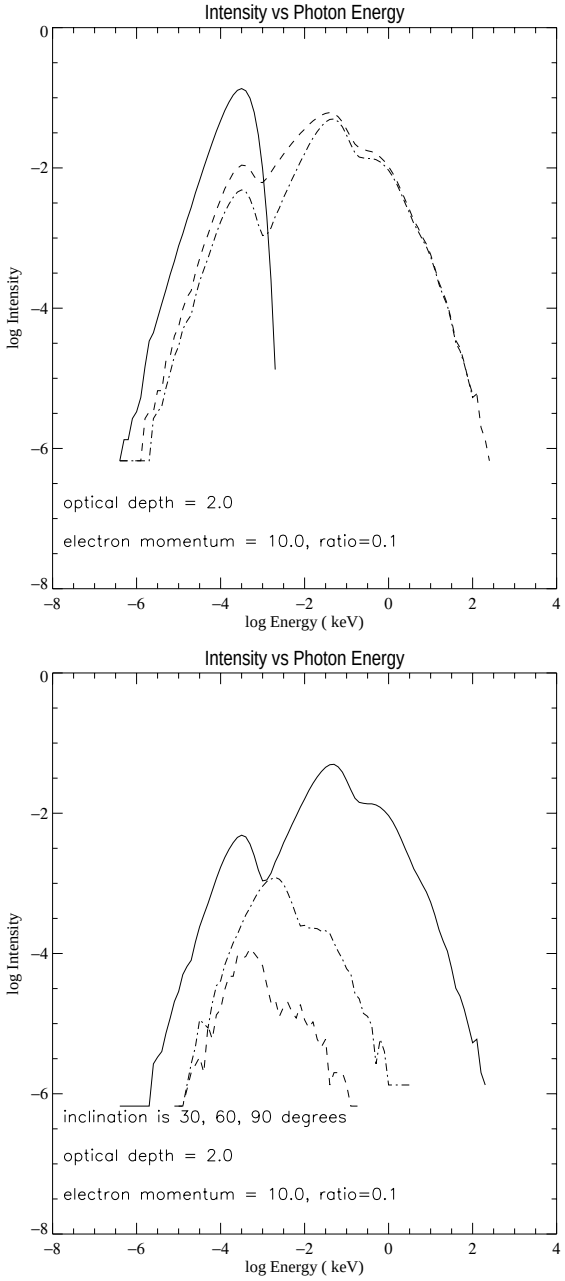

Figure 6.11: Blackbody photons IC scattered by an orbiting torus of electrons. In the top panel, the solid curve is the input spectrum, the dashed curve is the total spectrum (integrated over all angles), and the dot-dashed curve is the spectrum seen at an inclination of $90°$. The momentum of the electrons in the torus $\eta = 10.0$. In the lower panel, the 3 curves are the spectra at $30°$, $60°$ and $90°$ inclination, (the dashed, dot-dashed and solid curves, respectively) with the $90°$ curve being the spectrum as seen from edge on to the torus.

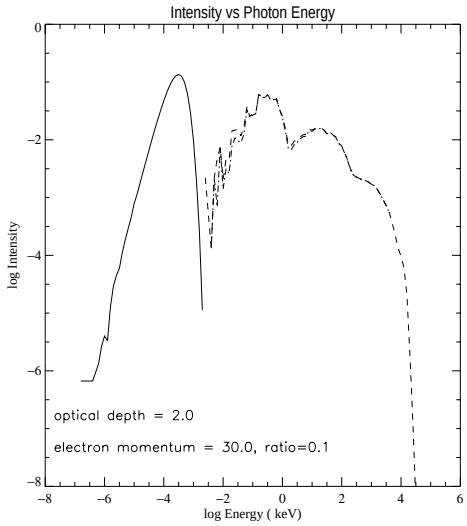

Figure 6.12: Blackbody photons IC scattered by an orbiting torus of electrons. The solid curve is the input spectrum, the dashed curve is the total spectrum (integrated over all angles), and the dot-dashed curve is the spectrum seen at an inclination of $90°$. The momentum of the electrons in the torus $\eta = 30.0$.

Power law injection

Figures 6.16, 6.17 and 6.18 present results for a power law of energy spectral index $\alpha = 1.0$ being injected into the torus, where $\eta = 2.0, 3.0$ and 6.0, corresponding to v^{ϕ}/c values of $0.89, 0.95$ and 0.99 respectively. Such a situation may occur if there is any interaction between an inner-disk rim and a central corona producing a power law of hard photons. For instance, some models of galactic X-ray binaries (Poutanen, Krolik & Ryde 1997) postulate that the disk rim can extend down into a hot central coronal region, with state transitions being caused by the extent to which the disk extends into the corona.

For low and moderate values of η (≤ 1.0) there is little difference between the input and output spectra, except the power law moves somewhat to higher energies. For larger η values (figure 6.16, 6.17 & 6.18) the spectra at $90°$ inclination have a broad trough-like feature that is caused by the superposition of unscattered power law seed photons at low energies, and the scattered component which is apparent at high energies.

For a given value of η, the shape of the scattered component is similar for different inclination angles, although the component is again shifted to higher energies as the

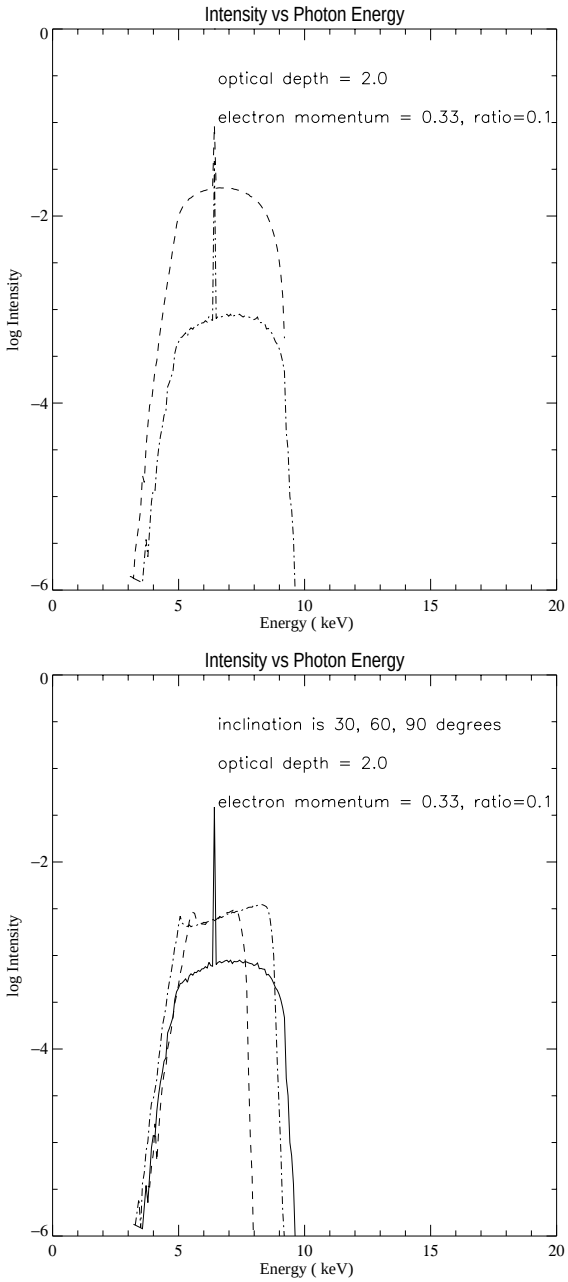

Figure 6.13: Line photons IC scattered by an orbiting torus of electrons. In the top panel, the dashed curve is the total spectrum (integrated over all angles) and the dot-dashed curve is the spectrum seen at an inclination of $90°$. The momentum of the electrons in the torus $\eta = 0.33$. The optical depth of the torus, as defined along the axis $R2$, is fixed to be 2.0, while the parameter 'ratio', defined to be $R2/R1$, is fixed to 0.1. In the lower panel, the 3 curves are the spectra at $30°$, $60°$ and $90°$ inclination, (the dashed, dot-dashed and solid curves, respectively) with the $90°$ curve being the spectrum as seen from edge on to the torus.

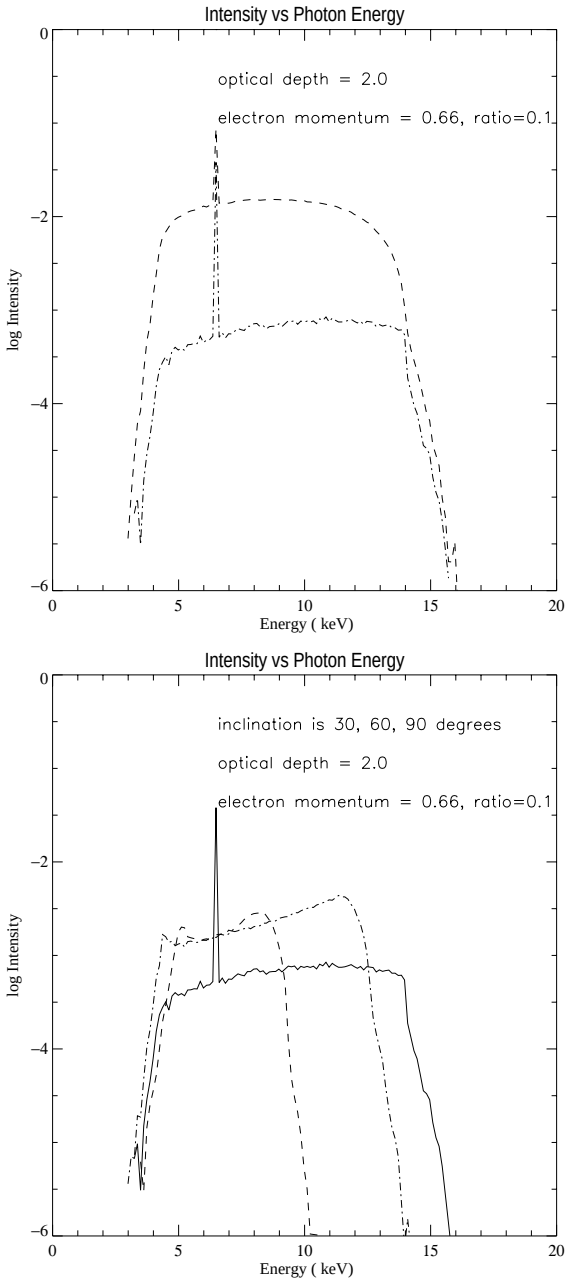

Figure 6.14: Line photons IC scattered by an orbiting torus of electrons. In the top panel, the dashed curve is the total spectrum (integrated over all angles) and the dot-dashed curve is the spectrum seen at an inclination of $90°$. The momentum of the electrons in the torus $\eta = 0.66$. In the lower panel, the 3 curves are the spectra at $30°$, $60°$ and $90°$ inclination, (the dashed, dot-dashed and solid curves, respectively) with the $90°$ curve being the spectrum as seen from edge on to the torus.

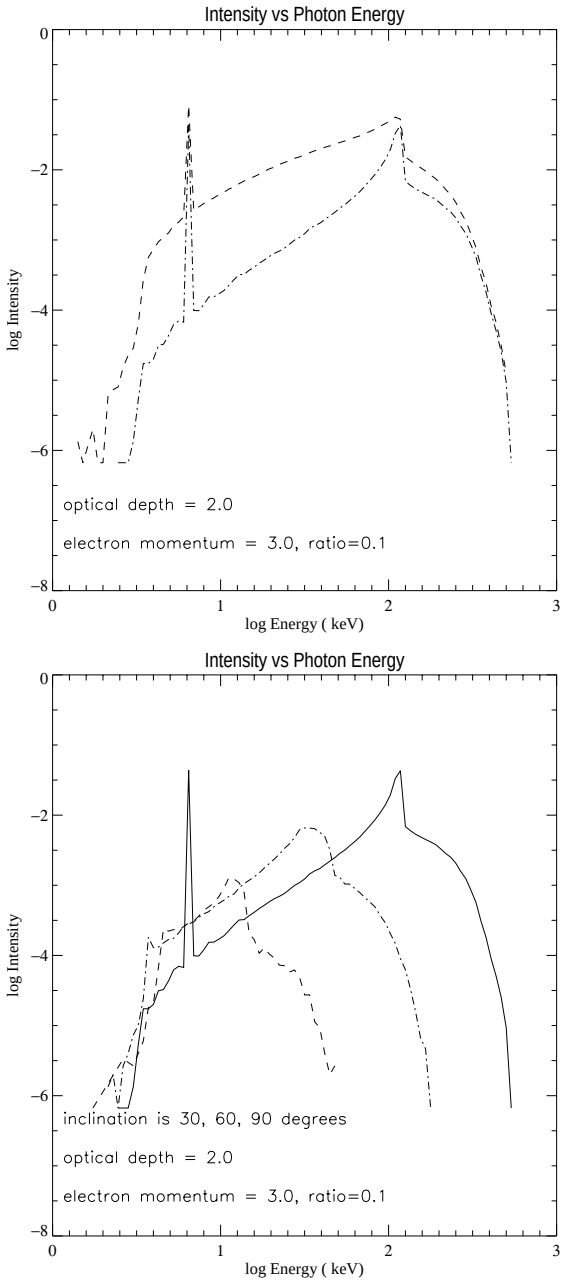

Figure 6.15: Line photons IC scattered by an orbiting torus of electrons. In the top panel, the dashed curve is the total spectrum (integrated over all angles) and the dot-dashed curve is the spectrum seen at an inclination of $90°$. The momentum of the electrons in the torus $\eta = 3.0$. In the lower panel, the 3 curves are the spectra at $30°$, $60°$ and $90°$ inclination, (the dashed, dot-dashed and solid curves, respectively) with the $90°$ curve being the spectrum as seen from edge on to the torus.

inclination angle increases (lower panels). The slope of the scattered components is similar or the same (figure 6.16, lower panel) as that of the injected spectrum even for extreme values of electron momentum. Most studies of the reflection component from accretion disks neglect the motions of material in the disk, and the fact that the slope of the injected power law is not distorted by bulk rotational motion seems to justify this assumption. The principal effect of bulk rotational motion on the power law is to systematically shift it to higher energies for high inclination angles.

6.2.4 Discussion

As mentioned in Section 6.2.1, the orbital kinetic energy in the inner regions of an accretion flow might be of the order of 100 keV. This corresponds to a dimensionless electron momentum parameter η equal to 0.66, which is smaller than most of the plots presented here $(3, 6, 10..)$. The torus would then need to be very optically thick to shift substantial numbers of photons up to high energies.

For all injected spectra, the escaping scattered spectra are approximately the same for most viewing angles, for a given value of η. This is partly because the torus considered here is optically thick, and so the photons direction of propagation gets randomized to a certain extent.

For the power law injection spectrum, the scattered power law slope seems approximately constant with inclination angle, for a wide range of electron momenta. This seems to justify the assumption of a static disk that is often used for studies of the accretion disk reflection component.

For line injection, the scattered spectra are double peaked (except when the torus is viewed exactly edge-on), with the width between the peaks increasing with increasing inclination angles. Broad double-peaked lines are indeed observationally seen (Tanaka et al. 1995), and are attributed to disk emission near a black hole. The width of the observed lines does seem to be of the same order as the width of the (simulation) scattered lines (i.e a few keV). However, any more detailed comparison with observed lines must wait until gravitational effects such as light bending and gravitational red-shift are included in future versions of the code used for this work. The most that can be currently said is that the width of the (simulation) lines may indicate that scattering can compete with general relativistic (GR) effects as a mechanism for line broadening.

In general, head-on collisions between soft photons and relativistic electrons result in high energy photons. The reason that rotational bulk motion is so inefficient at upscattering photons is that most of the collisions the photons suffer are glancing. At the

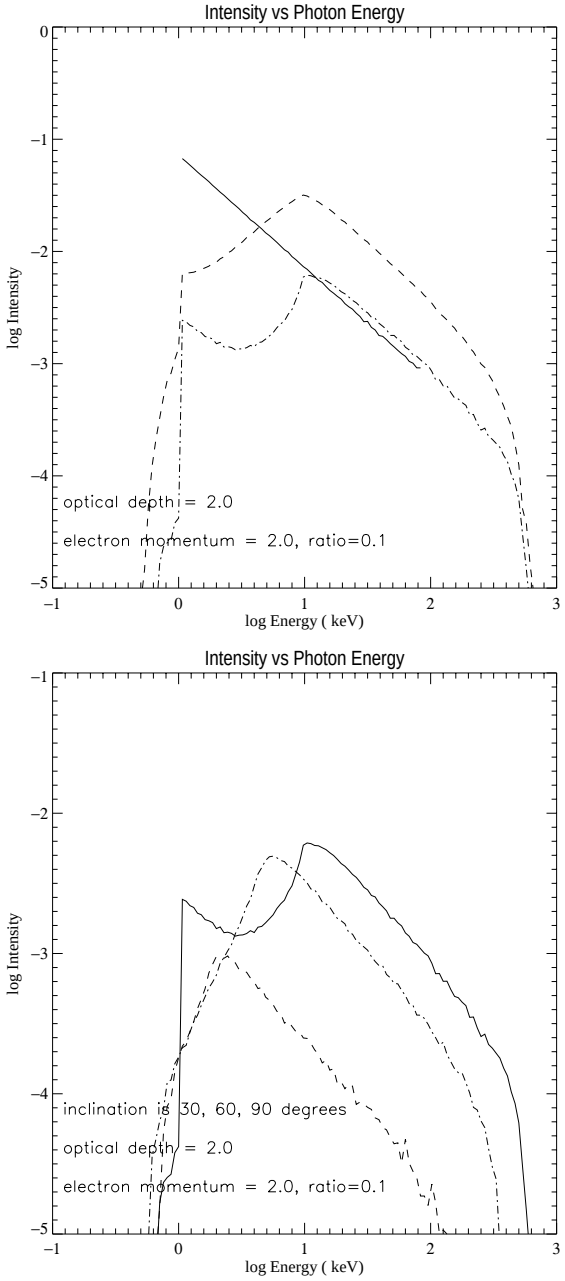

Figure 6.16: Power law photons IC scattered by an orbiting torus of electrons. In the top panel, the solid curve is the input spectrum, the dashed curve is the total spectrum (integrated over all angles), and the dot-dashed curve is the spectrum seen at an inclination of $90°$. The momentum of the electrons in the torus $\eta = 2.0$. The optical depth of the torus, as defined along the axis $R2$, is fixed to be 2.0, while the parameter 'ratio', defined to be $R2/R1$, is fixed to 0.1. In the lower panel, the 3 curves are the spectra at $30°$, $60°$ and $90°$ inclination, (the dashed, dot-dashed and solid curves, respectively) with the $90°$ curve being the spectrum as seen from edge on to the torus.

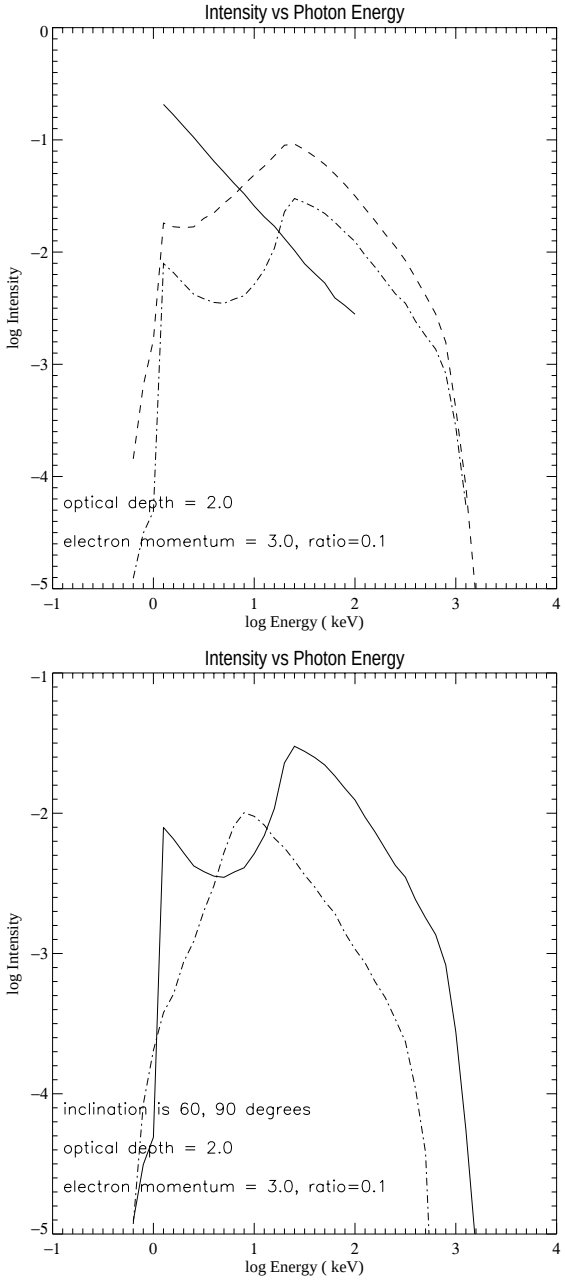

Figure 6.17: Power law photons IC scattered by an orbiting torus of electrons. In the top panel, the solid curve is the input spectrum, the dashed curve is the total spectrum (integrated over all angles), and the dot-dashed curve is the spectrum seen at an inclination of $90°$. The momentum of the electrons in the torus $\eta = 3.0$. In the lower panel, the 2 curves are the spectra at $60°$ and $90°$ inclination, (dot-dashed and solid curves, respectively) with the $90°$ curve being the spectrum as seen from edge on to the torus.

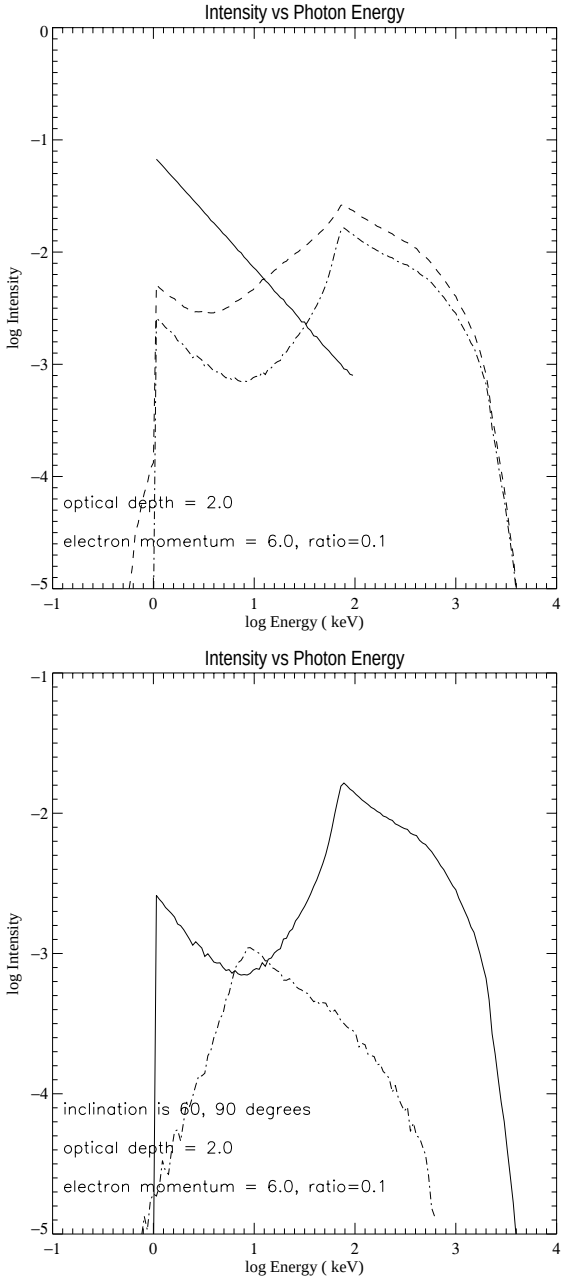

Figure 6.18: Power law photons IC scattered by an orbiting torus of electrons. In the top panel, the solid curve is the input spectrum, the dashed curve is the total spectrum (integrated over all angles), and the dot-dashed curve is the spectrum seen at an inclination of $90°$. The momentum of the electrons in the torus $\eta = 6.0$. In the lower panel, the 2 curves are the spectra at $60°$ and $90°$ inclination, (dot-dashed and solid curves, respectively) with the $90°$ curve being the spectrum as seen from edge on to the torus.

first scattering event the angle between an electron and a photon is $90°$, because the photons are travelling radially. The photon will most probably be scattered into the direction the electron is travelling, and so for any subsequent collisions the photon and electron will be travelling in approximately the same direction. Head-on collisions are rare.

In summary, it seems that bulk rotational motion is an inefficient means of producing hard photons. Injected blackbody spectra form a peak at approximately the energy of the torus electrons. Injected power law spectra keep the same power law slope, but are shifted to higher energies. Therefore, the effect of bulk rotational scattering for these two cases seems rather minimal. However, with reasonable parameters it is possible to produce broad double-peaked lines ($\sim$ a few keV wide). Scattering may therefore compete with GR effects as a mechanism for line broadening.

6.3 Conclusion

The Monte Carlo numerical technique has been applied in this Chapter to astrophysical problems where bulk motion is important. In particular, simulations have been performed where density, temperature and bulk motion with velocity gradients are present in the problem (the white dwarf case). It has been seen that the spectra are always peaked near the injection energy, and often single peaked due to the second peak being diminished as the shock approaches the white dwarf surface. A further application is to rotational motion Compton scattering, which should be a fundamental process if photons encounter electrons in orbit about a compact object. With moderate values of electron momentum, it is found that lines can be significantly broadened by rotational Compton scattering.

References

Aizu, K. 1973, Prog. Theor. Phys., 49, 1184

Bardeen, J. M., Press, W. H. & Teukolsky, S. A. 1972, ApJ, 178, 347

Chakrabarti, S. K. 2000, Class. Quan. Grav., v17, 12, 2427 (arXiv:astro-ph/0007259)

Chakrabarti, S. K. & Titarchuk, L. 1995, ApJ, 455, 623

Colpi, M. 1988, ApJ, 326, 223

Drake, S. P. 2000, in press (arXiv:gr-qc/0010082)

Ezuka, H. & Ishida, M. 1999, ApJ Supplement 120, 277

Frank, J., King, A. R. & Raine, D. J. 1985, "Accretion Power in Astrophysics", (Cambridge University Press)

Fujimoto, R. & Ishida, M. 1997, ApJ, 474, 774

Hua, X. 1997, Comp. Ph., 11, 660 (see also arXiv:physics/9709023)

Ishida. M., et al. 1994, MNRAS, 266, 367

Ishida, M., Mukai, K. & Osborne, J. P. 1994, PASJ, 46, L81

Kallman, T. & White, N. E. 1989, ApJ, 341, 955

Laurent, P. & Titarchuk, T. 1999 ApJ, 511, 289

Poutanen, J. Krolik, J. & Ryde, F. 1997, MNRAS, 292, L21

Pozdnyakov, L. A., Sobol, I. M. & Sunyaev, R. A. 1983, Ap.& Space Sci. Reviews, 2, 189

Reynolds, C. S. & Begelman, M. C. 1997, ApJ, 488, 109

Shapiro, S. L. & Teukolsky, S. A. 1983, "Black Holes, White Dwarfs and Neutron Stars, The Physics of Compact Objects", (John Wiley & Sons)

Stern, B., et al. 1995, MNRAS, 272, 291

Sunyaev, R. A. & Titarchuk, L. 1980, A&A, 86, 121

Tanaka, Y. et al. 1995, Nature, 375, 659

Wu, K., Chanmugan, G., & Shaviv, G. 1994, ApJ, 426, 664

Chapter 7

Conclusions

Analytic results

This thesis has studied the Inverse Compton scattering mechanism in astrophysics, primarily via numerical studies. Chapter 1 reviewed the fundamental analytic results required for the interpretation of Comptonized spectra, results that were derived for the case of large optical depth when an approach based on the diffusion equation is suitable. Further, Chapter 1 presented a short introduction to the astrophysical systems within which Compton scattering is thought to be important for spectral formation. The reason that feedback is considered an important ingredient for disk-corona models was also discussed, using the expression for the spectral index.

Semi-analytic disk-corona models with feedback were considered in detail in Chapter 4, with the effect of a disk wind or outflow on the energy balance of the disk, and therefore on the X-ray spectrum, being considered. While the presence of a wind can result in a hotter corona and harder X-ray spectra, the wind parameter must be large for this to occur. Only then can significant power be extracted from the disk to reduce the photon flux cooling the corona. It was also seen that a situation is possible where increasing the optical depth of the corona results in a harder X-ray spectrum, the opposite to the trend usually considered.

Numerical advance

Since numerical approaches based on the Monte Carlo technique are generally considered the most flexible, Chapter 2 provided both an introduction to the Monte Carlo technique and the application of this technique to the specific case of inverse Compton scattering. The method of modeling a scattering event via the differential cross-section

and the method of transporting photons from one scattering event to the next were presented.

The photon transport method becomes more difficult if the situation to be studied involves an electron distribution that is not isotropic. An elegant algorithm for treating these situations is the non-linear Monte Carlo approach. Chapter 3 discussed this, and then proposed and implemented an extension to this algorithm that enables the straightforward calculation of scattering in situations where the electron distribution is a complicated function of position. It was seen that such an algorithm is suitable for the calculation of scattering in plasmas containing bulk flow of electrons in addition to temperature and density gradients.

Applications of the numerical approach

The linear Monte Carlo approach was applied in Chapter 5 to a study of the time lags that are to be expected in the X-ray light curves of Cyg X-1 due to the Comptonization of photons in a corona that may consist of a multi-temperature plasma. It was shown that the phase and time lag curves contain a rise at low Fourier frequencies indicating the presence of an outer corona of plasma. The temperature of this outer corona did not greatly affect the time lags, however its optical depth did effect the time lags as more or fewer scattering events took place in the outer corona.

The flexible numerical method presented in Chapter 3 has some immediate applications; namely to photon scattering in situations where bulk motion as well as temperature variations are important. Such a situation is the case of photon scattering in an accretion column. Chapter 6 presented a numerical study of this situation and it was found that variations in the cooling parameter of the post-shock region made little difference to the scattered spectrum. At high accretion rates, the second or 'backscatter' peak is attenuated as those photons are beamed downward by the accretion flow and have a high probability of impacting the white dwarf surface. The spectra as a function of viewing angle also are little affected by the value of the post-shock cooling parameter. At moderate accretion rates the strength of the backscatter peak could be a guide to the location of the photon source (at the shock or at the base of the column).

A basic process that has until now not been considered is electron-photon scattering when the electron's momentum is due to orbital motion; a situation termed bulk rotational scattering. This process was also studied in Chapter 6 for a toroidal geometry and, in a key conclusion of this work, bulk rotational scattering was found to significantly broaden a line of photons when the orbital velocity of the electrons in the orbiting torus

was greater than about $0.3c$. The effect on the energy distribution of injected blackbody photons was to produce a peak in the scattered distribution at the energy of the orbiting electrons, while power law distributions of photons are little affected by scattering in the torus.

In summary, the codes written using the algorithms in this thesis were successfully applied to a number of astrophysical situations that had either not been studied previously (the bulk rotational scattering calculation), or had used approximate methods (the white dwarf accretion column calculation). Monte Carlo techniques are now flexible enough to treat most scattering problems of interest in astrophysics.

Part IV

Appendix

Appendix A

Monte Carlo photon transport code

```
      program compton_photons

ccccccccccccccccccccccccccccccccccccccccccccccccccccccccccccccccc ccccccccc
c     This is a code that calculates Compton scattering
c     in a weakly magnetised White Dwarf star accretion column.
c
c     This Monte Carlo code calculates the spectrum produced
c     by inverse Compton scattering of photons off Maxwellan
c     electrons in a cylindrical geometry, with density and velocity
c     gradients in the column. The cylinder extends along the x-axis.
c
c     The distance between events is determined using a modified
c     non-linear transport method. The full Klein-Nishina
c     cross-section is used.
c
c     The actual scattering events are modelled according to the
c     Pozdnyakov, Sobol' and Sunyaev method.
c
c     Inputs are the mass and radius of the white dwarf star, the
c     specific accretion rate, the viewing (inclination) angle,
c     and the ratio of bremstrahlung to cyclotron cooling in the
c     post-shock region.
c
c     The scattered spectrum output file is fort.12
c     The photon distribution with escape angle output file is fort.13
c
ccccccccccccccccccccccccccccccccccccccccccccccccccccccccccccccccc
```

```
ccccccccccccccccccccccccccccccccccccccccccccccccccccccccccccccccccccccccc
c            definitions of some variables
c
c    wdmass          mass of the white dwarf star (solar mass units)
c    wdradius        radius of the white dwarf star (cm)
c    wdaccretion     total accretion rate (grams per second)
c    e0, e1          energy of first/last energy bins in eV, linear scale
c    nbintotal       total number of energy bins
c    nphot           total number of photon trajectories
c    bin1            output spectrum bins
c    bin2            output pulse profile bins
c    dontbin         ignores the photon if .true.
c    ebin1(k)        energy of bin1(k) in eV, it is used to bin
c                    both the input & output spectra.
c    abin1(k)        angular bins, used for pulse profile
c    genrand()       name of random number generator (not included in code)
c    nbin(k)         number of photons in ebin1(k), input spectrum
c    pi              constant pi
c    amc2            constant electron rest energy
c    omfp            mean free path (mfp)
c    aradius         radius of accretion column, in units of Thompson mfp
c    tau             Thompson optical depth in the accretion column
c    done2           ends a photon trajectory when .true. (photon escape)
c    dcce            distance to the white dwarf from photon position
c    bbtemp          plank temperature of source photons in units of eV
c    plank           switch between plank (1.0) and line photon injection
c    electemp        maxwellian temperature of electrons in units of mc^2
c    vel(k)          velocity profile of the post-shock region
c    dens(k)         density profile of the post-shock region
c    temp(k)         temperature profile of the post-shock region
c    shockh          height of the accretion shock above WD surface
c    acolumn         the total length of the accretion column
c    aradiuswd       dimentionless constant, related to white dwarf radius
c    binlinear       switch between linear and log energy bins.(0.0=log)
c    cyclotron       ratio of cyclotron cooling to bremstrahlung cooling
c                    in the post-shock region
c    isotropic       isotropic photon injection if equal to one
c    plank           switch between blackbody and line injection
c    aline           input line energy in eV
c    ainclination    the inclination angle that the system is seen from
c    ainca/b         how wide the inclination angle bin is
c    shocktemp       the temperature of the accretion shock
```

```
c    x1, x2, x3          the current location of the photon (vector)
c    omeg1, 2, 3         the current photon propagation direction (vector)
ccccccccccccccccccccccccccccccccccccccccccccccccccccccccccccccccccccccccc
            implicit real*8 (a-h, o-z)
            logical done, done2, dontbin
            dimension nbin(1:10000)
            dimension bin1(1:100000)
            dimension bin2(1:100000)
            dimension ebin1(1:10000)
            dimension abin1(1:10)
            dimension vel(1:1001)
            dimension dens(1:1001)
            dimension temp(1:1001)
ccccccccccccccccccccccccccccccccccccccccccccccccccccccccccccccccccccccccc
c           INPUT PARAMETERS OF THE SIMULATION, which have been taken from
c           the paper by Wu, Chanmugam & Shaviv 1994, ApJ, 426, 664
c           with additional relations as listed in Fujimoto & Ishida 1997, ApJ, 474, 774
c
c           mass of the white dwarf star (solar mass units)
            wdmass=0.5
c           radius of the white dwarf star (cm)
            wdradius=1.0e+09
c           specific accretion rate (grams per cm^2 per second)
            wdaccretion=60.0
c           ratio of cyclotron cooling to bremstrahlung cooling in the post-shock
            cyclotron=10.0
c           the inclination angle the spectrum is seen from (degrees)
            ainclination=30.0
c           electron free-fall velocity just above the shock (v/c)
            velff=(0.0123)*((wdmass/0.5)**0.5)* ((wdradius/1.0e+9)**-0.5)
c           electron temperature at the shock, in units of 16 keV
            shocktemp=(0.0313111)*(wdmass/0.5)* ((wdradius/1.0e+9)**-1.0)
c           non-magnetic shock height (cm)
            shockheight=(7.59e+6)*((wdaccretion/4.0)**-1.0)*
        +   ((wdmass/0.5)**1.5)*((wdradius/1.0e+9)**-1.5)
c           dimensionless radius of the accretion column (a constant)
            aradius=50.0
c           dimensionless radius of the white dwarf star (a constant)
            aradiuswd=10.0*aradius
c           the length of the accretion column
            acolumn=aradiuswd + (aradiuswd/2.0)
c           the optical depth of the accretion column just above the shock
```

```
            tau=(((6.65e-25)*(aradius/aradiuswd)*(1.0e+9))
     +      /1.6726e-24)*(wdaccretion/(velff*3.0e+10))
c           output energy limits in electron volts
            e0=6000.0
            e1=7000.0
c           switch between linear and log bins.(1.0=linear)
            binlinear=1.0
c           switch between line (0.0) or blackbody injection photons (1.0)
            plank=0.0
c           input temperature of blackbody source photons, in electron volts
            bbtemp=130.0
c           input line energy (eV)
            aline=6700.0
c           isotropic photon injection if equal to one (1.0)
            isotropic=1
c           inject photons isotropically at the shock if equal to one (1.0)
            top=1.0
c           this is the total number of energy bins for the spectrum
            nbintotal=100
c           when a photon has escaped from the accretion column, this
c           becomes .true. and we stop following the photon.
            done2=.false.
c           the number of photons in the simulation
            nphot=10000
            type *, "number of photons? (integer)"
            accept *, nphot
c           in addition, other constants that the code requires are...
            ccc=3.0e8
            pi=atan(1.0)*4.0
            pi2 = pi*2.0
            amc2=511.0e3
            idummy = (2**19)+1
c           bin spectrum between these two angles
            ainca=cos((ainclination+5.0)*(pi/180.0))
            aincb=cos((ainclination-5.0)*(pi/180.0))
c           or alternatively, bin the angle integrated spectrum
c           ainca=-1.0
c           aincb=1.0
ccccccccccccccccccccccccccccccccccccccccccccccccccccccccccccccccccccccccccc

c           BEGINNING OF THE CODE: MAIN
```

```
c       determine the energy bins and the angular bins
        call start1(binlinear, nbintotal, e1, e0, ebin1, anglebin, abin1, pi)

c       determine the post-shock density, temperature & velocity profiles
c       that the photons will propagate through.
        call profiles(vel, dens, temp, shockh, aradiuswd, cyclotron,
     +  shockheight, wdradius)

c       start a photon trajectory
        do j = 1, nphot

c       inject the photon into the accretion column
        call start2(omeg1, omeg2, omeg3, isotropic, aline,
     +  x1, x2, x3, ncount3, bbtemp, aradius, aradiuswd,
     +  omegnew1, omegnew2, omegnew3, dontbin, velff,
     +  energy, energy1, shockh, plank, top,
     +  pi, pi2, idummy, dist, dist1, dcce, done, done2)

        scatcount=0.0

c       and begin the photon trajectory
        do while(.not.done2)

c       (never needed, this is here as a failsafe only)
        call stop(ncount3, energy, j, done2, dontbin)

c       find the next scattering point for the photon
        call transport(aradius, aradiuswd, tau, shockh, acolumn, index,
     +  dens, alambda, x1, x2, x3, omeg1, omeg2, omeg3)

c       the new photon scattering point is..
        x1new=x1+alambda*omeg1
        x2new=x2+alambda*omeg2
        x3new=x3+alambda*omeg3

c       has the photon escaped from the accretion column?
        call geometry(x1, x2, x3, x1new, x2new, x3new, alambda,
     +  aradius, aradiuswd, acolumn, omeg1, omeg2, omeg3,
     +  dontbin, done2)

        if (.not.done2) then
c       if it has not escaped then...
```

```
c       now we determine the velocity of the accretion flow at this point
        call frame1(gamma1, vpf, index,
     +  x1new, velff, aradiuswd, shockh, vel)

c       now model the actual scattering event.
        call scattering1(omeg1, omeg2, omeg3, cold,
     +  x1new, x2new, x3new, ncount3sum, index,
     +  omegnew1, omegnew2, omegnew3, shocktemp,
     +  energy, electemp, idummy, temp, gamma1, vpf,
     +  done2, amc2, pi, pi2, j, scatcount)

c       update photon location
        x1=x1new
        x2=x2new
        x3=x3new
c       update the photon direction
        omeg1=omegnew1
        omeg2=omegnew2
        omeg3=omegnew3
c       energy is updated in the scattering subroutine.

        endif

        enddo
c       end of current photon trajectory!!



c       sort into bins (input spectrum)
        call bin_input(ebin1, energy1, nbin, ii, nbintotal)

c       sort into bins (output spectrum)
c       if the photon has not been killed,
        if (.not.dontbin) then

c       scatcount is the scattering order, 1, 2, 3...
c       if (scatcount.eq.1.0) then
c       and if the photon is at the correct inclination angle, bin it.
        if (omeg1.ge.ainca) then
        if (omeg1.le.aincb) then
        call bin_output(ebin1, energy, bin1, ii, nbintotal, j)
```

```
            endif
            endif
c           endif

c           also, sort photons into angular bins (output spectrum)
            call bin_profile(abin1, omeg1, bin2, ii, nbintotal)

            endif

            enddo
c           end of all photon trajectories, nphot!!

c           output to files (bin1 is scattered spectrum)
            call output(ebin1, nbin, bin1, nbintotal, nphot, abin1,
     +      bin2, ncount3sum, binlinear)

            stop
            end
```

```
      subroutine bin_input(ebin1, energy1, nbin, ii, nbintotal)
c     This subroutine sorts the input photons drawn from 'blackbody'
c     into bins (input spectrum)

      implicit real*8 (a-h, o-z)

      dimension ebin1(1:10000)
      dimension nbin(1:10000)
      logical done

      ii=1
      done = .false.

350   if (.not.done) then

      if (ebin1(ii).ge.energy1) then
      done = .true.
      nbin(ii)=nbin(ii)+1
      else
      ii=ii+1
      endif
      if (ii.gt.nbintotal) then
      print *, "photon off scale", j, ebin1(nbintotal), energy1
      stop
      endif
      goto 350
      endif

      return
      end
```

```
      subroutine bin_output(ebin1, energy, bin1, ii, nbintotal, j)
c     This subroutine sorts the scattered photons into bins
c     (output spectrum)

      implicit real*8 (a-h, o-z)

      dimension ebin1(1:10000)
      dimension bin1(1:100000)
      logical done


      ii=1
      done = .false.
  400 continue
      if (done.eq..false.) then

      if (ebin1(ii).ge.energy) then
      done = .true.
      bin1(ii)=bin1(ii)+1.0

      else

      ii=ii+1
      endif
      if (ii.gt.nbintotal) then
      bin1(nbintotal)=bin1(nbintotal)+1.0
      done = .true.
      endif

      goto 400
      endif

      return
      end
```

```
      subroutine bin_profile(abin1, omeg1, bin2, ii, nbintotal)
c     This subroutine sorts the scattered photons into angular bins
c     pulse profile (output spectrum)

      implicit real*8 (a-h, o-z)

      dimension abin1(1:10)
      dimension bin2(1:100000)
      logical done


      ii=1
      done = .false.
  425 continue
      if (done.eq..false.) then

      if (abin1(ii).le.omeg1) then
      done = .true.
      bin2(ii)=bin2(ii)+1.0

      else

      ii=ii+1
      endif
      if (ii.gt.nbintotal) then
      bin2(nbintotal)=bin2(nbintotal)+1.0
      done = .true.
      endif

      goto 425
      endif

      return
      end
```

```
      subroutine blackbody(idummy, energy, bbtemp)
c     This subroutine assigns an initial energy for each photon
c     that is drawn from a Plank blackbody.
c     variable 'energy' is the photon energy.


      implicit real*8 (a-h, o-z)

c     energy/temp in units of eV
      temp=bbtemp

      eps5=1.0-genrand()
      eps6=1.0-genrand()
      eps7=1.0-genrand()
      eps8=1.0-genrand()

      test3=1.202*eps5

      if (test3.lt.1.0) then
      alpha=1.0
      else
      aa=1.0
      h=1.0
      do while (aa.le.test3)
      h=h+1.0
      aa=aa+(1.0/(h**3))
      enddo

      alpha=h
      endif

      energy=-1.0*(temp/alpha)*log(eps6*eps7*eps8)
      if ((energy.gt.1.0e30).or.(energy.le.0.0)) then
      print *, "crazy input photons"
      endif


      return
      end
```

```
      subroutine direction1(v1, v2, v3, brow, pi2)

c     This returns a random electron incident direction
c     or a random initial photon direction.

      implicit real*8 (a-h, o-z)

      brow=0.0
      do while (brow .eq. 0.0)
      yyran=1.0-genrand()
      v3=2.0*genrand()-1.0
      vsq = sqrt(1.0-v3*v3)
      svv = sin(pi2*yyran)
      v2=vsq*svv
      v1=vsq*cos(pi2*yyran)
      brow=sqrt(v1*v1+v2*v2)
      enddo

      return
      end
```

```
      subroutine frame1(gamma1, vpf, index,
     +  x1new, velff, aradiuswd, shockh, vel)

c     this subroutine determines the velocity and gamma factor of the
c     flow at the potential scattering point. This is needed for the
c     Lorentz transform out of the flow rest frame.

      implicit real*8 (a-h, o-z)
      dimension vel(1:1001)

c     find the height of the photon above the white dwarf, and then
c     get the velocity of the flow at that point.
      index=int(((x1new-aradiuswd)/(shockh))*1000.0)
      index=index+1
      if (index.le.0) then
      index=1
      endif
      if (index.le.1000) then
c     if photon is in the post-shock region, then velocity is
      vpf=velff*vel(index)
      else
c     if photon is in the pre-shock region, then velocity is
      vpf=velff
      endif
c     Lorentz factor of accretion flow
      gamma1=1.0/(sqrt(1.0-vpf*vpf))


      return
      end
```

```
      subroutine frame2(eta, gamma1, vpf, v1, v2, v3, brow)

c     this subroutine Lorentz transforms out of the accretion flow rest
c     frame, and back into the white dwarf frame.

      implicit real*8 (a-h, o-z)

c     Lorentz transform back into the White Dwarf rest frame.
c     "eta" is now the new electron momentum in the new frame.
c     gamma1 and vpf are the lorentz factor and velocity at the point
c     of the possible scattering event.
      if (eta.eq.0.0) then
c     then there is no thermal motion, and the electron is simply moving
c     with the flow.
      eta=(gamma1)*(vpf)
      v1=-1.0
      v2=0.0
      v3=0.0
      brow=sqrt(v1*v1+v2*v2)
      else
c     The electron momentum vector in the White Dwarf rest frame is ..
      ee1=v1*eta-eta*
     + (gamma1*vpf-(gamma1-1.0)*v1*(1.0))*(1.0)
      ee2=v2*eta
      ee3=v3*eta
c     convert to a unit vector plus a magnitude
      amagnew=(ee1*ee1+ee2*ee2+ee3*ee3)**(0.5)
c     the direction back in the 'lab' frame (WD star at rest) is ..
      v1=ee1/amagnew
      v2=ee2/amagnew
      v3=ee3/amagnew
      brow=sqrt(v1*v1+v2*v2)
c     energy back in the 'lab' WD frame is now
      eta=amagnew

      endif

      return
      end
```

```
      subroutine geometry(x1, x2, x3, x1new, x2new, x3new, alambda,
     +  aradius, aradiuswd, acolumn, omeg1, omeg2, omeg3,
     +  dontbin, done2)

c     This subroutine keeps track of the photon as it
c     propagates through the geometry and determines if it is
c     outside the accretion column or if it has hit the White
c     Dwarf surface.

      implicit real*8 (a-h, o-z)
      logical done2, dontbin

c     photon distance from central axis of the accretion column
      dist=(x2new*x2new+x3new*x3new)**(1.0/2.0)
c     if photon is outside the accretion column, stop the trajectory.
      if (dist.gt.aradius) then
      done2=.true.
      endif

c     if photon is outside the 'top' of the accretion column, stop traj.
      if (x1new.gt.acolumn) then
      done2=.true.
      endif

c     check if photon will impact on the White Dwarf surface.
c     If so, kill the photon.
      dcce=0.0
      dist1=(x1*x1+x2*x2+x3*x3)**(1.0/2.0)
      angle1=(x1*omeg1+x2*omeg2+x3*omeg3)/dist1
      xangle=2.0*dist1*angle1
      test5=(xangle*xangle-4.0*
     +  (dist1*dist1-aradiuswd*aradiuswd))

      if (test5.ge.0.0) then
      if (angle1.le.0.0) then

c     then the photon is heading towards the White Dwarf surface, so

c     if photon already outside accretion column, it will definitely
c     hit the White Dwarf, so kill it.
      if (done2.eq..true.) then
      dontbin=.true.
```

```
c           endif
            else

c           if photon is still inside accretion column, it may hit the WD.
c           calculate the distance to the White Dwarf 'dcce'
c           This solves a quadratic derived from the cosine rule c2=a2+b2-2a.b
            dcce=(-1.0*xangle-(xangle*xangle-4.0*
     +      (dist1*dist1-aradiuswd*aradiuswd))**(0.5))/2.0

            if (alambda.gt.dcce) then
c           photon will hit the surface, so stop trajectory and kill photon.
            done2=.true.
            dontbin=.true.
            endif

            endif
            endif
            endif


            return
            end
```

```
      subroutine maxwell(idummy, eta, electemp)
c     use for n above 0.29 (kT greater than 150 keV)
c     This subroutine assigns to each electron a momentum that
c     is drawn from an isotropic maxwellian distribution, if the
c     temperature of the electron distribution greater than 0.29
c     note: electemp is n

      implicit real*8 (a-h, o-z)

c     electron temperature (units of electron rest mass kT / mc2)

  100 continue
      eps1=genrand()
      eps2=genrand()
      eps3=genrand()
      eps4=genrand()

      if (eps1.eq.0.0) then
      goto 100
      endif
      if (eps2.eq.0.0) then
      goto 100
      endif
      if (eps3.eq.0.0) then
      goto 100
      endif
      if (eps4.eq.0.0) then
      goto 100
      endif

      eta=0.0
      eta1=-1.0*electemp*log(eps1*eps2*eps3)
      eta2=-1.0*electemp*log(eps1*eps2*eps3*eps4)
      if ((eta2*eta2 - eta1*eta1).gt.1.0) then
      eta=eta1
      else
      goto 100

      endif

      if (eta.le. 0.0) then
      print *, "crazy electron momentum"
```

```
endif

return
end
```

```
      subroutine maxwell_low(idummy, eta, electemp)
c     use for n below 0.29 (kT less than 150 keV)
c     This subroutine assigns to each electron a momentum that
c     is drawn from an isotropic maxwellian distribution, if the
c     temperature of the electron distribution is less than 0.29

      implicit real*8 (a-h, o-z)

c     electron temperature (units of electron rest mass kT / mc2)

   90 continue
      eps9=1.0-genrand()
      eps10=1.0-genrand()

      eta=0.0

      eta3=-1.5*log(eps9)
      eta4=eps10*eps10
      test3=0.151*(1.0+electemp*eta3)*(1.0+electemp*eta3)
     + *eta3*(2.0+electemp*eta3)*eps9

      if (eta4 .lt. test3) then
      eta=sqrt(electemp*eta3*(2.0+electemp*eta3))
      else
      goto 90

      endif

      return
      end
```

```
      subroutine meanfreepath(omfp, electemp, tau, aradius, energy, amc2)
c     This subroutine calculates the mean free path of the photons
c     using the relativistic cross section for compton scattering,
c     assuming an isotropic and homogeneous electron distribution.
c     THIS SUBROUTINE IS NOT USED IN THIS CODE, but is used in the linear
c     Monte Carlo code and is presented here for the sake of completeness.

      implicit real*8 (a-h, o-z)

      nsum=40
      hh=2.0*(energy / amc2)
      ann=electemp

      gg=1.0 / (0.375*(tau / aradius))
      sighsum=0.0
      sigh1sum=0.0
      sigh2sum=0.0
      sigh1=0.0
      sigh2=0.0
      aa=0.0
      aaa=0.0

      test4=2.0*hh*(1.0+ann*log(2.0*float(nsum)))
      if (test4.le.0.001) then
      omfp=(aradius / tau)
      return
      endif

      do jj=1, nsum

      gambeta=1.0-(ann*log((jj- 0.5) / float(nsum)))
      aaa=(gambeta*sqrt(gambeta*gambeta-1.0)) + aa
      aa=aaa

      gambetplus=hh*(gambeta+sqrt(gambeta*gambeta-1.0))
      gambetminus=hh*(gambeta-sqrt(gambeta*gambeta-1.0))

      x=gambetplus
      if (gambetplus.le.0.5) then

      sigh1=((x*x) / 6)+(0.047*((x)**3))-
     +  (0.03*((x)**4))+(x*x) / (2.0*(1.0+x))
```

```
      else

      if (gambetplus.gt.3.5) then

      sigh1=(1.0 +x)*log(1.0 +x)-(x / 2.0)-
     +  13.16*log(2.0 +(0.076*x))+9.214
      else
      sigh1=(1.0 +x)*log(1.0 +x) -(0.94*x) -0.00925

      endif

      endif

      x=gambetminus
      if (gambetminus.le.0.5) then

      sigh2=((x*x) / 6)+(0.047*((x)**3))-
     +  (0.03*((x)**4))+(x*x) / (2.0*(1.0+x))
      else

      if (gambetminus.gt.3.5) then

      sigh2=(1.0 +x)*log(1.0 +x)-(x / 2.0)-
     +  13.16*log(2.0 +(0.076*x))+9.214
      else
      sigh2=(1.0 +x)*log(1.0 +x) -(0.94*x) -0.00925

      endif

      endif

      if ((gambetplus.lt.0.0).or.(gambetminus.lt.0.0)) then
      print *, ”problem in meanfreepath”
      stop
      endif

      sigh1sum=sigh1+sigh1sum
      sigh2sum=sigh2+sigh2sum
      sighsum=sigh1sum-sigh2sum

      enddo
```

```
ggg=gg*aa
omfp=(ggg*hh*hh)/sighsum

return
end
```

```
      subroutine output(ebin1, nbin, bin1, nbintotal, nphot, abin1,
     +  bin2, ncount3sum, binlinear)

c     This subroutine outputs the initial and final spectra to files.
c     as well as the beam profile of escaping photons.
c     (bin1 is scattered spectrum)

      implicit real*8 (a-h, o-z)

      dimension bin1(1:100000)
      dimension bin2(1:100000)
      dimension ebin1(1:10000)
      dimension abin1(1:10)
      dimension nbin(1:10000)

      open(unit=11, STATUS= 'UNKNOWN')
      open(unit=12, STATUS= 'UNKNOWN')
      open(unit=13, STATUS= 'UNKNOWN')
      open(unit=21, STATUS= 'UNKNOWN')

c     write the input and output spectra to files
      do jj = 1, nbintotal

c     this counts the number of escaping photons.
      sumbin=sumbin+bin1(jj)/float(nphot)

c     ebin1 in KeV if divide by 1000
      outx=ebin1(jj)/1000
      outy1=bin1(jj)/float(nphot)
      outy=float(nbin(jj))/float(nphot)

      if (outx.eq.0.0) then
      outx=1.0
      endif
      if (outy.eq.0.0) then
      outy=1.0
      goto 500
      endif

      if (binlinear.eq.0.0) then
      write (11,*) log10(outx), log10(outy)
      else
```

```
      write (11,*) outx, log10(outy)
      endif

  500 continue

      if (outy1.eq.0.0) then
      outy1=1.0
      goto 600
      endif

      if (binlinear.eq.0.0) then
      write (12,*) log10(outx), log10(outy1)
      else
      write (12,*) outx, log10(outy1)
      endif

  600 continue

      enddo

c     write the angular bins to a file
      do jj = 1, 10

      outx1=abin1(jj)+0.1
      outy2=bin2(jj) / float(nphot)

      if (outy2.eq.0.0) then
      outy2=1.0
      goto 610
      endif

      write (13,*) outx1, outy2
  610 continue

      enddo

      write (21,*) "Output from inverse Compton scattering "
      write (21,*) " Monte Carlo code, version white dwarf: "
      write (21,*) "Spectra output to fort.11, fort.12"
      write (21,*) "Pulse profile output to fort.13"
      write (21,*) " "
      write (21,*) "number of photons in the run"
```

```
      write (21,*) nphot
      write (21,*) ”intensity normalization   1.0”
      write (21,*) sumbin
      write (21,*) ”average number of scatterings per photon is..”
      write (21,*) float(ncount3sum) / float(nphot)
      write (21,*) ”Code Output Completed: Thankyou”

      close(unit=11)
      close(unit=12)
      close(unit=13)
      close(unit=21)

      print *, ”Spectra output to fort.11, fort.12”
      print *, ”Pulse profile output to fort.13”
      print *, ”More information about this run can be found in fort.21”
c     sumbin is the intensity normalization   1.0
      print *, ”intensity normalization   1.0”
      print *, sumbin
      print *, ”average number of scatterings per photon is..”
      print *, float(ncount3sum) / float(nphot)
      print *, ”Code Output Completed: Thankyou”

      return
      end
```

```
      subroutine profiles(vel, dens, temp, shockh, aradiuswd, cyclotron,
     +  shockheight, wdradius)

c     This subroutine determines the velocity, density and temp profiles
c     in the post-shock region of a white dwarf accretion column,
c     using an integral expression as determined by
c     Wu et al. 1994, MNRAS 426, 664.
c     The subroutine breaks the post-shock region into 1000 zones.
c     The inputs required are the ratio of brem cooling to cyclotron
c     cooling eps, the number of zones in the post-shock region denstep,
c     and whether the region is optically thick or thin alpha/beta.
c     note that 'tau' as used in this subroutine is not optical depth,
c     but is a dimensionless velocity.

      implicit real*8 (a-h, o-z)
      dimension vel(1:1001)
      dimension dens(1:1001)
      dimension temp(1:1001)

c     constants for the integration

c     density stepsize: adjust this to get the required number
c     of zones in the post-shock region
      denstep=1000.0
c     stepsize in velocity, for the integral (don't adjust)
      stepsize=0.0000001
c     initial velocity
      tau=stepsize
c     optically thick cooling powerlaws
      alpha=2.0
      beta=3.85
c     or alternativly, the optically thin cooling powerlaws
c     alpha=7.5
c     beta=8.5
c     ratio of brem to cyclotron (use equation (10) of Wu et al. 1994)
      eps=cyclotron

c     find the total value of the integral
c     (need this below for normalisation)
      do while(tau.le.(0.25))
c     tau is a dimensionless velocity, and is integrated over
      dum=tau
```

```
c       the following INTEGRAND is from WU et al., MNRAS, 1994
        aint=dum*dum*(5.0-8.0*dum)/((dum*(1.0-dum))**(0.5))
     +  *(( 1.0 + ((4.0**(alpha+beta))/3.0**alpha)*eps
     +  *((1.0 -dum)**(alpha))*(dum**beta) )**(-1.0))
c       area of this rectangle is value times stepsize
        aintegral=aint*stepsize
c       sum the integral as you go
        sumintegral=sumintegral + aintegral

c       next step in velocity
        tau=tau+stepsize

c       end integration loop
        enddo

c       reset some values for the next integration
        aintvalue=sumintegral
        xx1=aintvalue/denstep
        value=xx1
        sumintegral=0.0
        tau=stepsize
        index=1.0

c       This is the same integration, except that it now
c       gives the normalised profiles
        do while((sumintegral/aintvalue).le.1.0)

c       tau is a dimensionless velocity, and is integrated over
        dum=tau
c       INTEGRAND from WU et al., MNRAS, 1994
        aint=dum*dum*(5.0-8.0*dum)/((dum*(1.0-dum))**(0.5))
     +  *(( 1.0 + ((4.0**(alpha+beta))/3.0**alpha)*eps
     +  *((1.0 -dum)**(alpha))*(dum**beta) )**(-1.0))
c       area of this rectangle is value times stepsize
        aintegral=aint*stepsize
c       sum the integral as you go
        sumintegral=sumintegral + aintegral

c       normalised velocity, density, temperature profiles
        if(sumintegral.ge.value) then
        vel(index)=tau
        dens(index)=1.0/tau
```

```
      temp(index)=16*tau*(1.0-tau)/3.0
c     write the normalised profiles at this point to files (if you want)
      write(30,*) index, vel(index)
      write(31,*) index, dens(index)
      write(32,*) index, temp(index)
      value =value + aintvalue/denstep
      index=index+1
      endif

c     next step in velocity
      tau=tau+stepsize

c     end integration loop
      enddo

c     end of the profile, you have reached the shock.

c     the (dimensionless) height of the magnetised shock is
      shockh=(sumintegral/4.9147193E-02)*(shockheight/wdradius)
c     shock height in units the code uses (mean free path units)
      shockh=shockh*aradiuswd

      return
      end
```

```
      subroutine scattering1(omeg1, omeg2, omeg3, cold,
     +  x1new, x2new, x3new, ncount3sum, index,
     +  omegnew1, omegnew2, omegnew3, shocktemp,
     +  energy, electemp, idummy, temp, gamma1, vpf,
     +  done2, amc2, pi, pi2, j, scatcount)

c     This subroutine takes in the photons direction of propagation
c     and energy, and models the scattering event with an electron drawn
c     from a Maxwellian distribution in the flow frame. It then Lorentz
c     transforms to the white dwarf frame, and returns the new energy and
c     new direction of propagation for the photon.

      implicit real*8 (a-h, o-z)
      dimension temp(1:1001)
      logical done2

      if (index.le.1000) then
c     if photon is in the post-shock region then temperature is
      cold=0.0
      electemp=shocktemp*temp(index)
      else
c     cold electrons in pre-shock (in the flow frame, 1.0=cold)
      cold=1.0
      electemp=0.0
      endif

      count=0.0
   10 continue

c     eta=p/mc ; the electron momentum
      if (cold.eq.0.0) then

c     there are 2 routines that can be called depending on what
c     temperature you are interested in.
      if (electemp.ge.0.29) then
      call maxwell(idummy, eta, electemp)
      else
      call maxwell_low(idummy, eta, electemp)

      endif

      else
```

```
c       or you can have cold electrons
        eta=0.0

        endif

c       draw an incident direction for your electron
        call direction1(v1, v2, v3, brow, pi2)

c       Lorentz transform out of the flow frame, into the white dwarf frame
        call frame2(eta, gamma1, vpf, v1, v2, v3, brow)

c       calculate amu angle cosine between photon/electron
        amu=v1*omeg1 + v2*omeg2 + v3*omeg3

c       lorentz factor, beta=v/c, for the incident electron
        gamma=sqrt(eta*eta + 1.0)
        beta=eta/gamma

c       proportional to photon energy
        xxx=2.0*energy*gamma*(1.0 -(amu*beta))/amc2

c       calculate cross section for the photon
        if (xxx.le.0.5) then
        sigma=(1.0/3.0)+(0.141*xxx)-(0.12*xxx*xxx)+
     +  ((1.0+0.5*xxx)/((1.0+xxx)*(1.0+xxx)))
        else

        if (xxx.gt.3.5) then
        sigma=(log(1.0+xxx)+0.5-(1.0/(2.0+0.076*xxx)))/xxx
        else
        sigma=(log(1.0+xxx)+0.06)/xxx

        endif

        endif

        if (sigma.lt.0.0) then
        print *, "cross-section has gone negative"
        print *, energy, xxx
        stop
        endif
```

```
c       have here the rejection technique (Stern 1995; MNRAS, 272, 291)
c       the relative velocity is
        vit=(1.0 - beta*amu)
        thompson=1.0
        ccc=1.0
c       wish to keep event with a probability of
c       ((3.0/4.0)*sigma*vit)/(thompson*2.0*ccc), so...
        test5=(3.0/4.0)*sigma*vit
        test6=(1.0-genrand())*(thompson*2.0*ccc)
        if (test6.lt.test5) then
c       then "keep the scattering event"

        ncount10=0
   15   continue
        ncount10=ncount10+1
        if (ncount10.gt.1000) then
        print *, "looped too many times2"
        done2=.true.
        endif

c       new angle (scattered)
        yran = genrand()
        amunew=(beta+2.0*yran-1.0)
     +  /(1.0+beta*(2.0*yran-1.0))


c       azimuthal scattering angle
        aaran=1.0-genrand()
        theta=2.0*pi*aaran

c       find new photon direction
        omegnew1=amunew*v1+sqrt(1.0-amunew*amunew)*
     +  (v2*cos(theta)+v1*v3*sin(theta)) /brow
        omegnew2=amunew*v2+sqrt(1.0-amunew*amunew)*
     +  (v2*v3*sin(theta)-v1*cos(theta)) /brow
        omegnew3=amunew*v3-sqrt(1.0-amunew*amunew)*
     +  sin(theta)*brow

c       photon scattering angle
        anglescat=omeg1*omegnew1+omeg2*omegnew2+omeg3*omegnew3
```

```
c       proportional to new photon energy
        ratio=( 1.0+ (energy*(1.0 -anglescat)
     +  /((1.0 -(amunew*beta))*gamma*amc2)) )
        xxxnew=xxx/ratio

c       test the new angle amuNew (rejection technique)
c       bbb is a parameter used in the expression for the cross-section
        bbb=(xxx/xxxnew) + (xxxnew/xxx) + 4.0*((1.0/xxx) - (1.0/xxxnew))
     +  +4.0*((1.0/xxx) - (1.0/xxxnew))*((1.0/xxx) - (1.0/xxxnew))
        yyy=((xxxnew*xxxnew)/(xxx*xxx))*bbb
        test2=2.0*genrand()

        if (test2.ge.yyy) then
        goto 15
        endif
        ncount3sum=ncount3sum+1

c       the photon energy after scattering is
        aaa=1.0/( (2.0*gamma)*(1.0 -amunew*beta) )
        energynew=xxxnew*aaa*amc2
        energy=energynew
        scatcount=scatcount+1.0

        else
c       the potential scattering event has been rejected,
c       therefore photon continues in same direction without scattering

c       update the photon direction
        omegnew1=omeg1
        omegnew2=omeg2
        omegnew3=omeg3
c       no change in direction
        endif
c       end of rejection loop

        return
        end
```

```
      subroutine start1(binlinear, nbintotal, e1, e0, ebin1, anglebin,
     +  abin1, pi)

c     This subroutine defines the energy bins and angle bins that
c     are to be used in the simulation

      implicit real*8 (a-h, o-z)
      dimension ebin1(1:10000)
      dimension abin1(1:10)

c     initialize the energy and angle bins.
      if (binlinear.eq.0.0) then
c     bin photon number at the side of each bin, log scale
      nbintotal=401
      do ii = 1, nbintotal
      ebin1(ii)=10**(-5.0+0.1*(ii-1))
      enddo

      else

c     bin photon number at the side of each bin, linear scale
c     this is best for investigating lines.
      do ii = 1, nbintotal
      ebin1(ii)=((e1-e0)*ii/float(nbintotal)) +e0
      enddo

      endif

c     bin angle at the side of each bin, evenly distributed in angle
      anglebin=0.0
      do ii = 1, 10
      abin1(ii)=1.0-0.2*ii

      enddo

      return
      end
```

```
      subroutine start2(omeg1, omeg2, omeg3, isotropic, aline,
     +  x1, x2, x3, ncount3, bbtemp, aradius, aradiuswd,
     +  omegnew1, omegnew2, omegnew3, dontbin, velff,
     +  energy, energy1, shockh, plank, top,
     +  pi, pi2, idummy, dist, dist1, dcce, done, done2)

c     initialize some variables and inject a photon

      implicit real*8 (a-h, o-z)
      logical done, done2, dontbin

      done = .false.
      done2=.false.
      dontbin=.false.
      energy=0.0
      count2=0.0
      ncount3=0

c     here we inject/start a new photon
      if (plank.eq.1.0) then
c     draw the initial photon energy from the plank distribution
      call blackbody(idummy, energy, bbtemp)
      else
c     inject a line, with energy in electron volts
      energy=aline
      endif
      energy1=energy

c     initialize the photon direction/location
c     inject photons on a plane at the base of the accretion column
      x1=aradiuswd
      x2=0.0
      x3=0.0
      omegnew1=0.0
      omegnew2=0.0
      omegnew3=0.0
      dist=0.0
      dist1=0.0
      dcce=0.0
      dist2=aradius +1.0
      do while (dist2.gt.aradius)
c     photons initially within a circle in y-z plane
```

```
      x2=aradius*genrand()
      x3=aradius*genrand()
      dist2=(x2*x2 + x3*x3)**(0.5)
      enddo
      if (isotropic.eq.1) then
c     send photons out in a random direction, in the flow rest frame
      call direction1(v1, v2, v3, brow, pi2)
      omeg1=v1
      omeg2=v2
      omeg3=v3
      if (top.eq.1.0) then
c     inject the photons at the shock height
      x1=x1+ shockh
c     velocity at the shock is 0.25 of the free-fall velocity
      vpf=velff/4.0
c     Lorentz factor of accretion flow
      gamma1=1.0/(sqrt(1.0-vpf*vpf))
c     Lorentz transform out of flow frame & into White Dwarf rest frame.
c     The photon propagation vector in the White Dwarf rest frame is ..
      ee1=omeg1*energy-energy*
     + (gamma1*(vpf)-(gamma1-1.0)*omeg1*(1.0))*(1.0)
      ee2=omeg2*energy
      ee3=omeg3*energy
c     convert to unit vector plus magnitude
      amagnew=(ee1*ee1+ee2*ee2+ee3*ee3)**(0.5)
c     photon direction back in the 'lab' frame (WD star at rest) is ..
      omeg1=ee1/amagnew
      omeg2=ee2/amagnew
      omeg3=ee3/amagnew
c     photon energy back in the 'lab' frame is now
      energy=amagnew
      endif
      else
c     photons are directed initially along the accretion column
      omeg1=1.0
      omeg2=0.0
      omeg3=0.0
      endif

      return
      end
```

```
      subroutine stop(ncount3, energy, j, done2, dontbin)

      implicit real*8 (a-h, o-z)
      logical done2, dontbin

c     should not be needed, but stops the code from running on forever...
      if (ncount3.gt.100000.0) then
      print *, ”looped too many times, something’s wrong”
      print *, energy, j
      done2=.true.
      dontbin=.true.
      ncount3=0
      endif
      ncount3=ncount3+1

      return
      end
```

```
      subroutine transport(aradius, aradiuswd, tau, shockh, acolumn, index,
     +  dens, alambda, x1, x2, x3, omeg1, omeg2, omeg3)

c     this subroutine transports the photons through the accretion column

      implicit real*8 (a-h, o-z)
      dimension dens(1:1001)

c     This is the mean free path (omfp) of the photon.
c     For the WD case, we are in the Thompson regime, so..
      omfp=(aradius/tau)

c     integrate over the accretion column density profile here
c     to find the distance to the next scattering event
c     you want the integral to equal this number
      propdist=-1.0*log(1.0-genrand())
      sumh=0.0
      sumintegral=0.0
      itest50=0
      xx1=x1
      xx2=x2
      xx3=x3
      dist3=0.0
      dist4=aradiuswd+1.0
c     this is the stepsize for the integration when the photon
c     is in the pre-shock region
      stepsize=0.001*aradiuswd

c     integrate, as long as the photon has not come out the sides
c     of the accretion column or the top of the accretion column
c     or hit the white dwarf surface.

      do while((sumintegral.lt.propdist).and.(dist3.le.aradius).and.
     +  (xx1.le.acolumn).and.(dist4.ge.aradiuswd))

c     the density profile function for the accretion column is
      index=int(((xx1-aradiuswd)/(shockh))*1000.0)
      index=index+1
      if (index.le.0) then
      index=1
      endif
      if (index.le.1000) then
```

```
c       if photon is in the post-shock region then the stepsize is
        stepsize1=0.01*shockh
        dpf=(tau/aradius)*dens(index)
        else
c       or constant density, because photon in in pre-shock region
        stepsize1=stepsize
        dpf=(tau/aradius)
        endif
        aintegral=dpf*stepsize1
        xx1=xx1+stepsize1*omeg1
        xx2=xx2+stepsize1*omeg2
        xx3=xx3+stepsize1*omeg3
        dist3=(xx2*xx2 + xx3*xx3)**(0.5)
        dist4=(xx1*xx1+xx2*xx2 + xx3*xx3)**(0.5)
        sumh=sumh + stepsize1
        sumintegral=sumintegral + 2.0*aintegral
        enddo

c       this is how far the photon has traveled
        alambda=sumh

        return
        end
```